UNIVERSITÄT HAMBURG
DEPARTMENT PHYSIK

Luminosity Measurements with the ATLAS Detector

Dissertation

zur Erlangung des Doktorgrades
des Fachbereichs Physik
der Universität Hamburg

vorgelegt von

STEFAN MÄTTIG
aus Hamburg

Hamburg

2012

Gutachter der Dissertation	: Prof. Dr. J. Haller
	: Dr. T. Pauly
Gutachter der Disputation	: Prof. Dr. J. Haller
	: Prof. Dr. P. Schleper
Datum der Disputation	: 6. August 2012
Vorsitzender des Prüfungsausschusses	: Dr. Michael Martins
Vorsitzender des Promotionsausschusses	: Prof. Dr. Peter H. Hauschildt
Leiter des Departments Physik	: Prof. Dr. Daniela Pfannekuche
Dekan der MIN-Fakultät	: Prof. Dr. Heinrich Graener

Abstract

For almost all measurements performed at the Large Hadron Collider (LHC) one crucial ingredient is the precise knowledge about the integrated luminosity. The determination and precision on the integrated luminosity has direct implications on any cross-section measurement, and its instantaneous measurement gives important feedback on the conditions at the experimental insertions and on the accelerator performance. ATLAS is one of the main experiments at the LHC. In order to provide an accurate and reliable luminosity determination, ATLAS uses a variety of different sub-detectors and algorithms that measure the luminosity simultaneously. One of these sub-detectors are the Beam Condition Monitors (BCM) that were designed to protect the ATLAS detector from potentially dangerous beam losses. Due to their fast readout and very clean signals this diamond detector is providing in addition since May 2011 the official ATLAS luminosity. This thesis describes the calibration and performance of the BCM as a luminosity detector in the years 2010 and 2011. The calibration was performed via so called van-der Meer (*vdM* -) scans. These scans allow to measure the convolved beam sizes in vertical and horizontal directions, which can be used together with the precise knowledge of the beam intensities to determine a luminosity calibration constant. Detailed evaluation of all possible error sources affecting this method including cross-checks amongst many different sub-detectors lead to a final ATLAS luminosity uncertainty for *pp* collisions at $\sqrt{s} = 7\,\text{TeV}$ of $\delta\text{L}/\text{L}$=3.4% for 2010, and of $\delta\text{L}/\text{L}$=2.2% for 2011.

Zusammenfassung

Für fast alle Messungen am Large Hadron Collider (LHC) ist die präzise Kenntnis der Luminosität von enormer Wichtigkeit. Die integrierte Luminosität ist notwendig zur Bestimmung von Wirkungsquerschnitten und ihre instantane Messung liefert wichtige Informationen über die experimentellen Bedingungen an den Kollisionspunkten und über die Leistung des Beschleunigers. ATLAS ist eins der beiden großen Experimente am LHC. Für eine genaue und verlässliche Bestimmung der Luminosität nutzt ATLAS eine Vielzahl verschiedener Sub-Detektoren und Algorithmen. Zu diesen Sub-Detektoren gehören die Beam-Condition-Monitors (BCM), deren Aufgabe es ist, gefährliche Abweichungen des Strahls von seiner Sollumlaufbahn zu entdecken, und somit den inneren Detektor vor schädigender Strahlung zu schützen. Aufgrund ihrer schnellen Auslese und ihrer extrem präzisen Signale liefern die BCM seit Mai 2011 zusätzlich die offiziellen ATLAS Luminositäts Messungen. Die folgende Doktorarbeit beschreibt die Kalibrierung und Performanz der BCM als Luminositäts-Detektor in den Jahren 2010 und 2011. Ihre Kalibrierung wurde mithilfe sogenannter van der Meer Scans durchgeführt. Diese erlauben die Messung des transversalen Strahl-ueberlapps in horizontaler und in vertikaler Richtung. Zusammen mit der präzisen Kentniss der Intensitäten beider Strahlen ist es damit möglich eine Kalibrationskonstante für die Luminosität zu bestimmen. Detaillierte Abschätzungen der Fehlerquellen dieser Methode, sowie der Vergleich von Messungen verschiedener Sub-Detektoren ergeben eine finale Unsicherheit der ATLAS Luminosität für Proton-Proton Kollisionen bei $\sqrt{s} = 7\,\text{TeV}$ von $\delta\text{L}/\text{L}$=3.5% für 2010 und von $\delta\text{L}/\text{L}$=2.2% für 2011.

Contents

Chapter 1

Introduction

The Large Hadron Collider (LHC) at CERN is a 27 km two-ring, superconducting accelerator and collider that started its operation in November 2009. By colliding high intensity proton beams a center-of-mass energy of 7 TeV the LHC set a new world record at the beginning of 2010.
The LHC aims for a wide scientific program, that stretches from precision measurements of the Standard Model, such as top-quark and b-quark physics, to the discovery of new physics beyond the Standard Model. The main motivation behind the LHC project is, however, the discovery of the Higgs boson, that was predicted more than 40 years ago and has not yet been found.
For almost all measurements performed at the LHC one crucial ingredient is the precise knowledge about the integrated luminosity. The determination and precision on the integrated luminosity has direct implications on any cross-section measurement, and its instantaneous measurement gives important feedback on the conditions at the experimental insertions and on the accelerator performance.
ATLAS is one of the main experiments at the LHC. This thesis describes the calibration and performance of the ATLAS Beam Condition Monitor (BCM) as a luminosity sub-detector in *pp* collisions in the years 2010 and 2011. Primarily designed to protect the ATLAS detector from potentially dangerous beam losses, this diamond detector is providing the official ATLAS luminosity since May 2011.
The calibration was performed via so called van-der Meer (*vdM* -) scans, that are dedicated beam-separation scans which are used to determine the absolute luminosity. Two such *vdM* scan sessions, performed in October 2010 and in May 2011, are analyzed in this thesis. The final results of this analysis are calibrating the official ATLAS luminosity of $\sqrt{7}$ TeV *pp* collisions recorded in 2011, that is input to most physics analysis of this data taking period.
This analysis has contributed to a total luminosity precision of 3.4% on the 48 pb^{-1} recorded data by ATLAS in 2010 [1] and to a precision of 2.2% on the 5.6 fb^{-1}

recorded in 2011 [2].

This thesis will start with a general overview on luminosity measurements at hadron colliders. This will be followed by a description of the LHC in Chapter 3, with an emphasis on the devices and parameters that are relevant for the performance of *vdM* scans. Chapter 4 will describe the ATLAS detector and in particular its variety of luminosity sub-detectors and its luminosity infrastructure. The *vdM* method will be explained theoretically and experimentally, including all its uncertainties, in Chapter 5. This Chapter will also introduce the different event-counting algorithms and how they are translated into luminosity values. A detailed analysis of two *vdM* scans is then given in Chapter 6 and Chapter 7 and finally a summary and discussion of the results will be presented in Chapter 8. As this analysis introduces a large number of abbreviations and symbols, not common to every particle-physicist, a Glossary in Appendix A has been added.

Chapter 2

Luminosity at Hadron Colliders

The luminosity of a particle collider is determined by the rate of particle collisions it produces. Assuming a process $pp \to X$, the luminosity $\mathscr{L}(t)$ is the process-independent proportionality factor between the rate $R_{pp\to X}(t)$ and its production cross-section $\sigma_{pp\to X}$:

$$R_{pp\to X}(t) = \mathscr{L}(t) \cdot \sigma_{pp\to X} \tag{2.1}$$

Its precise knowledge is important since for many cross-sections measurements the uncertainty on the luminosity dominates the final result. In particular in view of the possibility to constrain the parton distribution functions (PDFs) which will have a direct impact on the systematics of several important measurements, a precision at the level of a few percent is aimed at the LHC [3]. The definition in 2.1 is also referred to as *instantaneous luminosity* and is usually expressed in units $\mathrm{cm}^2\mathrm{s}^{-1}$. As running conditions vary with time, the luminosity of a collider also has a time dependence. The integral over time is called *integrated luminosity* it is commonly denoted with $L = \int \mathscr{L}(t)\mathrm{d}t$, and measured in units b^{-1}. One further distincts *delivered integrated luminosity*, which refers to the integrated luminosity which the machine has delivered to an experiment, and *recorded integrated luminosity*, which refers to the amount of data that has actually been stored to disk by the experiments.
In order to give a description of the luminosity at hadron colliders, this chapter will start with a brief introduction of a few key parameters of accelerator physics and beam dynamics. This is followed by a section about the luminosity of bunched beams and about the most relevant luminosity reduction effects. Finally, different methods to determine the total luminosity scale will be presented.

2.1 Basics on Bunched Beams

The following will only give a very basic overview and focus only on aspects relevant for this thesis. Good introductory descriptions can be found e.g. in [4] or [5].

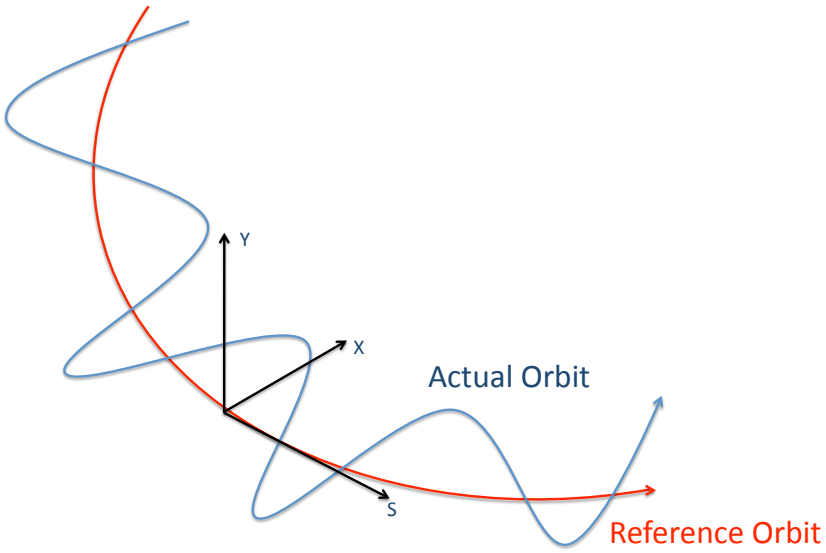

Figure 2.1 The coordinate system, used in the following, is traveling along the reference orbit. A particle is performing transverse oscillations around the design path, indicated by the blue line.

In a circular synchrotron accelerator, particles traversing along the ring are accelerated with a high amplitude alternating electric field, that is applied at each passage. The particles are being focused and bent by transverse magnetic fields. An ideal particle is traveling around the design path that is also called the *reference orbit*. An actual particle is performing oscillations around the reference orbit, as will be shown later. A schematic view including the definition of the local coordinate system, used in the following, is given in Figure 2.1.

Particles are traveling on two such orbits in opposite directions and are colliding at the interaction points (IPs). The accelerating and longitudinal focusing electric field is achieved with radio frequency (RF) cavities, which generate a longitudinal oscillating voltage of frequency f_{RF} along the beam axis. A *synchronous particle* stays exactly on the centered orbit. For a stable acceleration, the RF frequency of the cavities must be a constant integer of the revolution frequency f_{rev} of the synchronous particle. In that way it crosses the electric field every turn at a constant phase and thus experiences a constant force. In reality small errors will disturb this ideal motion and thus lead to deviations from the ideal orbit. Furthermore any initial distribution of particles injected into a synchrotron is non-monochromatic.

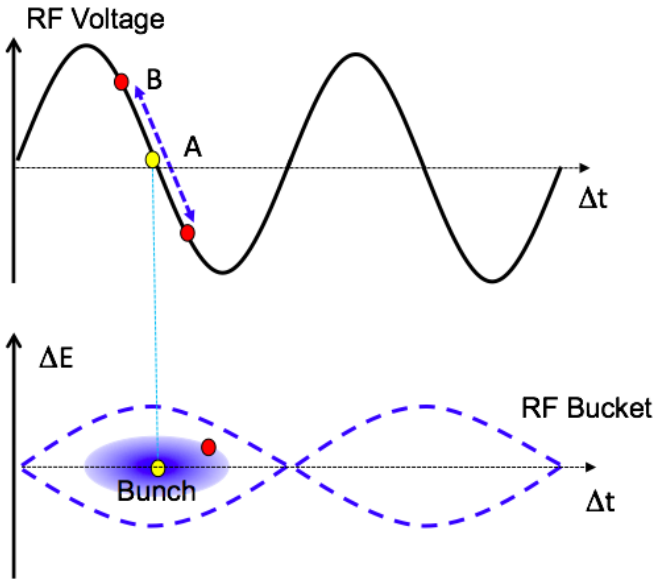

Figure 2.2 RF voltage and formation of RF buckets and bunches. Particle A is the synchronous particle, while particle B shows a non-synchronous that is performing oscillations in phase space. Shown is a simplified case of a *stationary bucket* where the synchronous particle passes the RF at zero voltage.

2.1.1 Longitudinal Particle Motion

The more realistic case of a *non-synchronous particle* has a small energy offset with respect to the synchronous particle. If one assumes relativistic particles above the transition energy, i.e. $v \approx c$, particles with higher energy will have a longer orbit, as they are less deflected by the bending magnets. Thus they have a lower revolution frequency, which will delay their arrival at the accelerating cavity. In turn, lower energy particles will have a shorter orbit, a higher revolution frequency, and will arrive earlier at the accelerating cavity.

Figure 2.2 shows a schematic example of the phase-focusing. A is the synchronous particle, arriving at the RF with the phase ϕ_s, where it experience zero voltage and thus no acceleration. The particle B arrives later with a phase difference of $\Delta\phi$ to the synchronous one, sees a positive RF voltage and thus receives acceleration. After some time, particle B will arrive at the same RF phase as the synchronous particle. However, with a higher energy ΔE and thus a higher frequency, and negative acceleration in the next turn. Particle B will therefore oscillate around the synchronous particle, forming an ellipse in phase space ΔE-$\Delta\phi$. The limiting case is where $\Delta\phi$ between A and B exceeds π. Any particle exceeding this limit gets unstable as it would receive acceleration that moves it further away from the synchronous particle. The boundary between stable and unstable particle defines an *RF bucket*. All particles within the RF bucket are performing so called *synchrotron oscillation* around the synchronous particle during acceleration. The collection of particles sharing a bucket is commonly defined as a

bunch. The RF frequency is therefore forming a chain of buckets that appear in a phase of 2π, which can potentially be filled with a bunch. The longitudinal shape of a bunch is thus defined by the RF frequency, and the number of buckets within an accelerator is defined by the ratio of the RF frequency divided by f_{rev}.

2.1.2 Transverse Particle Motion

The transverse bending and focusing of particles is provided by transverse magnetic fields. The most important magnets used in accelerators are dipoles and quadrupoles. Dipole magnets provide a constant field $\vec{B}_y$, they are used to guide the particles along the closed orbit.

Quadrupole magnets are used to control the beam size. Depending on the polarity, a quadrupole has a focusing effect on the beam in one plane and a defocusing effect in the plane orthogonal to it. A particle passing through the center of a quadrupole does not experience any force while the bending of its trajectory rises linearly with the distance from the center. It can be shown that a section composed of alternating focusing and defocusing elements has a net focusing effect, provided the quadrupoles are correctly placed. Therefore the most commonly used structure in accelerators are FODO cells. Such a cell contains a horizontal focusing (F) quadrupole, a drift space (O) and a horizontal defocusing (D) quadrupole. Their net effect is focusing, if the drift spaces between the quadrupoles are small compared to the focal length of the magnets. Particles with non-zero coordinates *x,y* and slopes *x',y'* in the transverse plane perform therefore oscillations in the horizontal and vertical planes around the reference orbit. This particle motion is called *betatron motion* and can be described in form of the Hill equation (here just shown for x):

$$\frac{\mathrm{d}^2x}{\mathrm{d}s^2} + K_x(s)x = 0 \tag{2.2}$$

This resembles the harmonic oscillator equation, except that $K_x(s)$, which is the effective focusing function of the magnets, depends on the longitudinal position s in the ring. The general solution of 2.2 can be written as:

$$x(s) = \sqrt{\beta_x(s)\varepsilon}\cos[\Phi_x(s) + \Phi_0] \tag{2.3}$$

This solution corresponds to a pseudo harmonic oscillation, which are called *betatron oscillations*. Φ_0 is called the *betatron phase advance* that is a constant determined by the initial conditions. $\Phi_x(s)$ is the phase which is a periodic non-linear function of s and $\beta_x(s)$ is the *betatron function*, both are defined by the arrangement of the magnets along the design orbit. During each turn the particles perform ν betatron oscillations around the reference orbit, with the local amplitude proportional to $\beta(s)$. The betatron

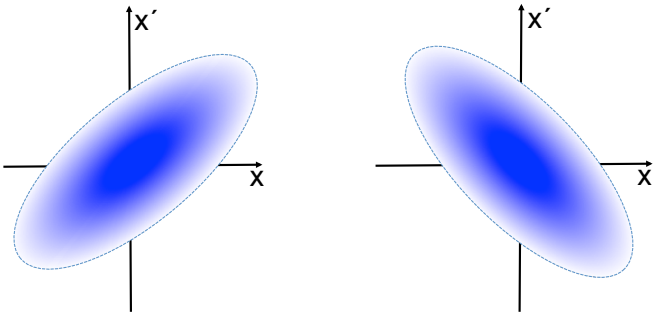

Figure 2.3 Conservation of phase space at different points s in the accelerator. Even if the shape of the ellipse changes, the area of the ellipse $\pi\varepsilon$ and remains constant.

function at the interaction point is denoted as β^* and is usually given in unit m. Plotting x versus x', where x' is the local slope of the beam $\mathrm{d}x/\mathrm{d}s$, within one turn for all particles in a bunch at a fixed position s, one ends up with ellipse of area $\pi\varepsilon$. This area is defined as the *emittance*. Doing the same for different positions s in the ring, $\beta_x(s)$ alters the shape of the ellipse, but one finds that the area remains constant all around the accelerator. This is illustrated in Figure 2.3. According to Liouville's theorem, the emittance area in phase space will be conserved as the beam circulates in a synchrotron, as long as the forces do not depend upon velocity. The latter is broken during proton acceleration because the longitudinal momentum increases while the transverse stays the same, and thus the slope x' decreases. As a result, the beam shrinks and its emittance is inversely proportional to the beam momentum. A conserved quantity is therefore the *normalized emittance*:

$$\varepsilon_{\mathrm{N}} = \gamma_{\mathrm{r}}\beta_{\mathrm{r}}\varepsilon \tag{2.4}$$

where $\beta_{\mathrm{r}} = v/c$ and $\gamma_{\mathrm{r}} = 1/\sqrt{1-\beta_{\mathrm{r}}^2}$.

Particles in a beam are often Gaussian distributed, when it is projected on the vertical or horizontal plane. In this case the emittance is commonly defined as:

$$\varepsilon_{x,y} = \frac{\sigma_{x,y}^2}{\beta_{x,y}(s)} \tag{2.5}$$

where $\sigma_{x,y}$ are the cross-sectional size of the bunch in horizontal and vertical plane, respectively. This formula shows that if β is low, the beam is narrow with a large spread in transverse momentum and vice-versa if β is high.

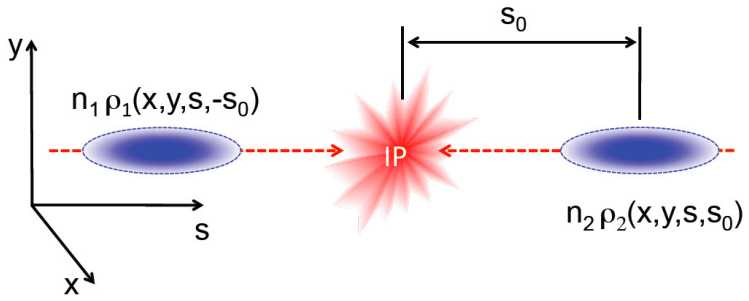

Figure 2.4 Schematic view of two bunches colliding at the IP with $\rho_{1(2)}$ being the distribution functions and $n_{1(2)}$ the number of particles per bunch in beam 1 (2).

2.2 The Luminosity of Bunched Beams

In a particle collider one assumes two colliding bunches with different time dependent particle distribution functions in three dimensions. A schematic view of a bunch-collision is shown in Figure 2.4. Since the two beams are passing through each other, their overlap depends on the longitudinal position of the bunches, therefore on the time they pass towards and through each other. The distance of the two beams to the central collision point can be written as $s_0 = c \cdot t$. The general equation for luminosity can be expressed with the overlap integral over the particle distribution functions $\rho_{1,2}$ of the two beams [6, 7]:

$$\mathscr{L} = n_1 n_2 f_r K \int\int\int\int_{-\infty}^{+\infty} \rho_1(x,y,s,-s_0)\rho_2(x,y,s,s_0)\mathrm{d}x\mathrm{d}y\mathrm{d}s\mathrm{d}s_0, \tag{2.6}$$

where $n_{1,2}$ are the number of particles per bunch, f_r the revolution frequency and x, y, s are the coordinates. The kinematic factor K is defined as [8]:

$$K = \sqrt{(\vec{v_1} - \vec{v_2})^2 - (\vec{v_1} \times \vec{v_2})^2/c^2}, \tag{2.7}$$

where $\vec{v_{1,2}}$ is the velocity of beam 1 (2). In the following it is assumed that the beams are colliding head on. Further, that the densities are uncorrelated in all planes, i.e. $\rho_i(x,y,s,-s_0) = \rho_{ix}(x)\rho_{iy}(y)\rho_{is}(s-s_0)$ for $i = 1,2$ and that $\vec{v_1} = -\vec{v_2}$. In the ultra-relativistic approximation, and by setting $c = 1$, the kinematic factor becomes $K = 2$. Now one can factorize the density distributions, and the overlap integral can be written as:

$$\mathscr{L} = 2n_1 n_2 f_r \int\int\int\int_{-\infty}^{\infty} \rho_{1x}(x)\rho_{1y}(y)\rho_{1s}(s-s_0)\rho_{2x}(x)\rho_{2y}(y)\rho_{2s}(s+s_0)\mathrm{d}x\mathrm{d}y\mathrm{d}s\mathrm{d}s_0 \tag{2.8}$$

Independent of the particle distributions at the source, beams are generally well described by Gaussian density profiles by the time the beam reaches high energy [9]. If one assumes Gaussian profiles in all dimensions, ρ can be written as:

$$\rho_{iu}(u) = \frac{1}{\sigma_{iu}\sqrt{2\pi}} \exp\left(-\frac{u^2}{2\sigma_{iu}^2}\right) \text{ where } i = 1,2, u = x,y \tag{2.9}$$

$$\rho_{is}(s \pm s_0) = \frac{1}{\sigma_{is}\sqrt{2\pi}} \exp\left(-\frac{(s \pm s_0)^2}{2\sigma_{is}^2}\right) \text{ where } i = 1,2 \tag{2.10}$$

Equation 2.8 expressed with 2.9 and 2.9 reads as:

$$\begin{aligned}\mathscr{L} = &\frac{2n_1 n_2 f_r}{(\sqrt{2\pi})^6 \sigma_{1x}\sigma_{2x}\sigma_{1y}\sigma_{2y}\sigma_{1s}\sigma_{2s}} \times \\ &\int\int\int\int_{-\infty}^{\infty} e^{-x^2\left(\frac{1}{2\sigma_{1x}^2}+\frac{1}{2\sigma_{2x}^2}\right)-y^2\left(\frac{1}{2\sigma_{1y}^2}+\frac{1}{2\sigma_{2y}^2}\right)-\frac{(s-s_0)^2}{2\sigma_{1s}^2}-\frac{(s+s_0)^2}{2\sigma_{2s}^2}} \mathrm{d}x\mathrm{d}y\mathrm{d}s\mathrm{d}s_0\end{aligned} \tag{2.11}$$

Integrating over s and s_0 and using the formula:

$$\int_{\infty}^{\infty} e^{-(ax^2+2bx+c)}\mathrm{d}x = \sqrt{\frac{\pi}{a}} \exp\left[\frac{b^2-ac}{a}\right] \tag{2.12}$$

One gets the following expression:

$$\mathscr{L} = \frac{n_1 n_2 f_r}{2\pi\sqrt{\sigma_{1x}^2+\sigma_{2x}^2}\sqrt{\sigma_{1y}^2+\sigma_{2y}^2}} \tag{2.13}$$

In case of head-on collisions and with the previous assumption that the density distributions are not correlated, the luminosity does not depend on the bunch lengths $\sigma_{1,2s}$. With n_b being the number of colliding bunches and by recalling Equation 2.5 the luminosity can be expressed in terms of ε and β^* as:

$$\mathscr{L} = \frac{n_1 n_2 f_r n_b}{2\pi\sqrt{(\varepsilon_{1x}\beta_{1x}^* + \varepsilon_{2x}\beta_{2x}^*)(\varepsilon_{1y}\beta_{1y}^* + \varepsilon_{2y}\beta_{2y}^*)}} \tag{2.14}$$

From this equation it is obvious that in order to achieve high luminosity, one needs to have many highly populated bunches of low emittance, colliding at high frequency at locations where the beam optics provides a value of β^* as low as possible.
However, in a particle collider there are several constraints on these parameters that limit the maximum achievable luminosity. For example the stored energy must not exceed the limit of a safe beam abort. Others are given by a maximum dipole field, the mechanical aperture or beam-beam effects, as explained in the next section.

2.3 Luminosity Limitations and Reduction Effects

Several factors are limiting the maximum achievable luminosity at a hadron collider. The ones most important will be discussed in the following.

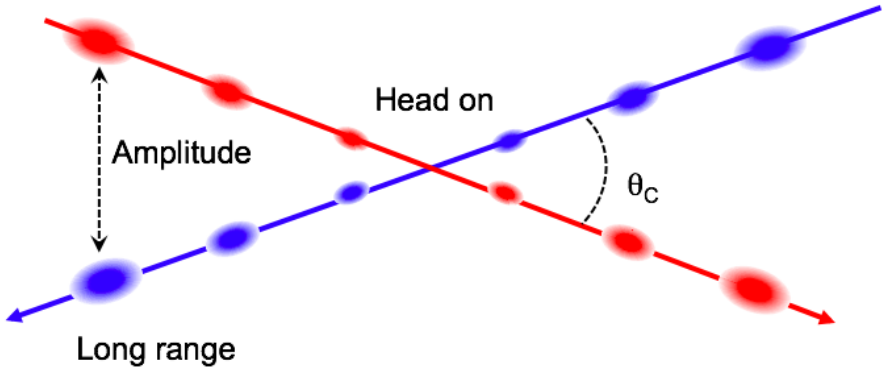

Figure 2.5 Two beams that are colliding with a crossing-angle θ_c. Beam-beam interactions occur when particles of one beam encounter the fields of the opposing beam.

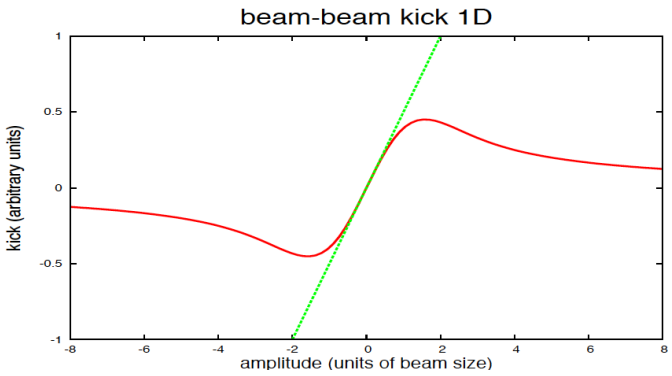

Figure 2.6 Beam-beam force(red) as a function of the amplitude for round beams in units of beam size σ_b. The green line corresponds to the linear force of a quadrupole [11].

2.3.1 Beam-Beam Effects

Every bunch can be seen as a collection of a large number of charges that represent an electromagnetic potential for other charges [10]. Therefore both beams exert forces on particles of the other beam (*beam-beam force*), but also a defocusing force on itself (*space charge*).

Beam-beam forces appear when bunches are colliding head-on, but also *long-range interactions* appear between bunches traveling in the same beam pipe. Figure 2.5 illustrates both interaction types. Figure 2.6 shows an example where the *kick*[1] produced by the beam-beam force for round beams is plotted against the amplitude (distance) between two beams. For small amplitudes (head-on collisions) the force is linear, while for larger amplitudes it becomes very non-linear. The linear part of the force resembles that of a quadrupole field. One therefore expects an additional defocusing effect and thus a change of the β functions of the beams. This effect, can lead to orbit distortions

[1] Kick is the change of the slope of the particles trajectory

that change the beam-optics and can finally result in an increase of the emittance and in non-Gaussian tails of the particle distributions. Going to higher amplitudes, one can see that at $\approx 1.6\sigma_b$ the local slope of the force, i.e. its derivative with respect to the amplitude, is changing sign, which means that an initially defocusing force becomes focusing at large amplitudes. The linear forces are most significant for high density beams, i.e. high intensity and small beam-sizes, exactly what is needed to achieve high luminosity. The beam-beam interactions are therefore often the limiting factor for the luminosity at a collider.

2.3.2 Total Beam Current

The luminosity is directly proportional to the intensity product $n_1 n_2$ of both beams. This stored energy must be absorbed safely at the end of each run or in the case of a malfunction or an emergency. The beam dumping system and the magnet system therefore provide additional limits for the maximum attainable beam energies and intensities.

2.3.3 Crossing Angle

As mentioned before, crossing angles are often introduced in order to restrict collisions only to the IP and to avoid unwanted *parasitic*- collisions at other positions in the ring. This is illustrated in Figure 2.5. Due to the crossing angle θ_c the luminosity will be reduced by the factor [12]:

$$F_c = \sqrt{1 + \left(\frac{\theta_c \sigma_s}{2\sigma^*}\right)^2} \tag{2.15}$$

where σ_s is the bunch length and σ^* the transverse r.m.s. beam size at the interaction point in case of round beams.

2.3.4 Beam Offset

If the beams are not exactly colliding head-on but with a small transverse offset the luminosity is reduced. Such an offset can be introduced due to beam-beam effects or imperfect centering. However, they can also be generated on purpose in beam-separation scans, as will be explained later. For Gaussian beams, the loss in luminosity can be expressed as [12]:

$$\frac{\mathscr{L}}{\mathscr{L}_0} = exp\left[-\frac{(\delta x)^2}{2(\sigma_{1x}^2 + \sigma_{2x}^2)} - \frac{(\delta y)^2}{2(\sigma_{1y}^2 + \sigma_{2y}^2)}\right] \tag{2.16}$$

where $\delta x, \delta y$ are the horizontal and vertical separation between the two beams and σ_x, σ_y the transverse r.m.s. beam sizes.

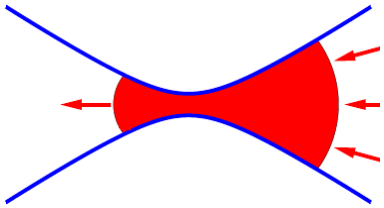

Figure 2.7 Sketch of the bunch shape (in red) at the IP, in order to illustrate the hour-glass effect. The blue line indicates the parabolic shape of the β function. The bunch has a minimum in transverse size at the IP and grows as it proceeds away from it [13].

2.3.5 Hourglass Effect

The β functions and beam sizes have a minimum at the IP and grow, as one proceeds away from it. Figure 2.7 shows a sketch to illustrate this. Collisions that occur away from the IP have therefore an increase in beam sizes and the luminosity is reduced. The effect becomes significant if β^* is small compared to the bunch length, in particular if the ratio $r = \frac{\beta^*}{\sigma_s}$ is of the order one or less [12].

2.4 Luminosity Calibration

As shown in Equation 2.1, the luminosity is the proportionality factor between the rate and cross-section of an observed process. As $\mathscr{L}$ is process-independent it is possible to measure the luminosity with any process whose cross-section is known. For a precise luminosity determination, however, it is essential that the process has precise theoretical predictions and at the same time that its rate can be accurately measured. For e^+e^- collider, the elastic scattering (Bhabha process) is often used, because it has both a high production rate and is theoretically well understood. This process allowed an absolute luminosity determination to about 0.05% at the Large Electron Positron collider (LEP) [14]. At the $pe^{+(-)}$ collider HERA an uncertainty of 1-3% could be achieved by counting the rate of Bethe-Heitler $ep \to e'p\gamma$ events [15].
In contrast to e^+e^- colliders the main challenge at hadron colliders is to find a theoretically precise reference process. There are essentially two reasons, the first one is that one has a strong process and the perturbative corrections are high and more difficult to calculate. Secondly, that instead of having point like interactions, one studies the collision of protons made out of quarks and gluons. The hard scattering interactions of quarks and gluons depend on the fraction of the protons momentum carried by the two colliding partons, that is described by the Parton Distribution Functions (PDF). The uncertainty of the PDFs limit the precision of the theoretical cross-section calculations for many processes [16].

At the LHC so-called *relative luminosity measurements* are performed by measuring the inelastic pp rate R_{inel}. This allows to monitor the luminosity evolution quantitatively. However the inelastic cross-section σ_{inel} at the LHC energies are theoretically not well described. And thus these measurements lack the overall normalization.
Several methods can be envisaged to calibrate these measurements with an *absolute* luminosity determination. Most of these have in common that they need special running conditions that are very different to normal physics operation. The basic principle of a luminosity calibration is to measure the absolute luminosity in a dedicated calibration run and measure simultaneously R_{inel} by a relative luminosity monitor. In this way the rate R_{inel} can be directly mapped to the absolute value and a calibration factor can be extracted. This allows to provide a luminosity measurement using the relative measurements at any given time of data taking. The following will give a short overview over different methods that can be used to determine the absolute luminosity at the LHC.

2.4.1 Absolute Luminosity from Standard Model Processes

Using Equation 2.1 with a process that has a well described cross-section one can determine the absolute luminosity by measuring the corresponding rate. However, the final accuracy on the luminosity is usually limited by the theoretical uncertainty on the calculated cross-section. The leptonic decay of $W^{\pm}$ and Z^0 bosons are often referred to as "standard candle processes", because they have clean signals and are theoretically well understood. They have large cross-section combined with experimentally well defined final states that are almost background free. Using different sets of PDFs, their theoretical cross-sections are at the level of 5% and the experimental accuracy is at the level of 1% or below [17]. Recent measurements of $W^{\pm}$ and Z^0 boson production cross-sections at the LHC are in agreement with the theoretical values, therefore they are suited to use them in addition for absolute luminosity measurements.
Other processes such as muon-pair production via two photon exchange $pp \to pp\mu^+\mu^-$ could in principle be used as well [18]. Their cross-section can be calculated to a level of 1%, but their rate is extremely low and the experimental acceptance and efficiency are difficult to calculate.

2.4.2 Absolute Luminosity using the Optical Theorem

Traditionally the luminosity at hadron colliders is determined via elastic scattering of protons at small angles. With this method a precision of the order of 2% could be obtained at the CERN $S\overline{p}pS$ collider. At the LHC this approach is taken by TOTEM [19] and the ALFA [20] experiments. The optical theorem states that the total cross-

section σ_{tot} is directly proportional to the imaginary part of the nuclear forward elastic scattering amplitude $f(t)$, extrapolated to zero momentum transfer $t = 0$ [21]:

$$\sigma_{\text{tot}} = 4\pi \,\text{Im}[f(t=0)] \tag{2.17}$$

And one gets the following expression for the luminosity:

$$\mathscr{L} = \frac{(1+\rho^2)}{16\pi} \frac{(R_{\text{el}} + R_{\text{inel}})^2}{(\text{d}R_{\text{el}}/\text{d}t)_{t=0}} \tag{2.18}$$

To measure $\mathscr{L}$ one thus requires the simultaneous measurement of the total elastic- (R_{el}) and inelastic- (R_{inel}) rates and the extrapolation of the differential elastic scattering rate ($\text{d}R_{\text{el}}/\text{d}t$) to the optical point $t = 0$. The parameter $\rho = \text{Re}[f(t=0)]/\,\text{Im}[f(t=0)]$ is in general taken from theoretical predictions.

It is required to have a very good detector coverage of the whole space for the inelastic rate measurement and the possibility to measure up to very small values of t. The latter is achieved with special high-β^* optics and requires detectors very close to the beam, which is in general realized with so called *Roman Pots*. At Fermilabs Tevatron the CDF and E811 experiments provided precisions on σ_{tot} for $\sqrt{s} = 1.8\,\text{TeV}$ $p\overline{p}$ collisions of about 2.8% [22]. For the most recent results an absolute luminosity uncertainty of about 6% could be achieved[2] [22].

Another approach, that is foreseen by ALFA, uses the Coulomb scattering amplitude. Here only the measurement of the elastic scattering at very small values of t is required, without the full coverage of the inelastic rate measurements. All unknown parameters, including $\mathscr{L}$ and σ_{tot} can be determined by a fit to the t-dependence of $\text{d}R_{\text{el}}/\text{d}t$. However, to access the Coulomb region measurements require optics with even higher β^* of several kilometers, and the detectors need to approach the beams at a distance of 1-2 mm. The commissioning of such optics is complex and only foreseen at a later stage of the LHC running.

2.4.3 Absolute Luminosity from Beam Parameters

Recalling Equation 2.13 one sees that the absolute luminosity can be extracted from certain beam parameters. The beam intensities can be measured with intensity monitors, which will be discussed in the following chapter, whereas the determination of the beam sizes at the IP is more delicate. It is possible to measure the beam profiles at certain positions in the accelerator using *wire scanners* or *synchrotron light monitors*, however to extrapolate the measurements to the IP a precise knowledge of the β-function is required. In order to determine β^*, the so-called *K-modulation* of the

[2] The σ_{tot} values were extrapolated to $\sqrt{s} = 1.96\,\text{TeV}$ and the luminosity was then determined via inelastic rate measurements.

nearest quadrupoles to the IP can be used. This procedure makes use of the fact that a betatron tune change $\delta\nu$ is related to the perturbation $\delta k(s)$ of the focusing strength and the β-function. Thus a change in the strength of the quadrupole allows the average β-function to be measured, by observing $\delta\nu$ as a function of $\delta k(s)$. However, presently the precision of these measurements is only about 5% [23].

A more precise possibility is to determine the transverse beam overlap in dedicated scans, by displacing the two beams against each other and simultaneously measure the interaction rate with dedicated luminosity monitors. This method is called *van der Meer* scans and as it is a main subject of this thesis it will be explained in detail in Chapter 5. A new approach, called Beam-gas imaging, is performed by the LHCb experiment [24]. Whose high resolution vertex detector makes it possible to perform precise measurements of the vertex positions of beam-gas and beam-beam interactions. With these measurements beam parameters such as width and position can be measured. More details can be found in [25].

Chapter 3

The LHC

This section will start with a brief overview of the Large Hadron Collider (LHC). A detailed description can be found in [26]. After an introduction of the present achievements and goals this chapter will focus on the operational aspects that are relevant for luminosity measurements and in particular for the *vdM* scan procedure. A strong focus in the last section will be on beam intensity measurements, which are a main ingredient for the determination of the absolute luminosity from beam-parameters.

3.1 General Overview

Parameter	2010	2011	2012	Nominal
Beam Energy [TeV]	3.5	3.5	4.0	7.0
Bunch Intensity $10^{11}p$	1.1	1.49	1.6	1.15
Number Of Bunches	368	1380	1380	2808
Luminosity at IP1/5 [$10^{33}\text{cm}^2\text{s}^{-1}$]	0.2	3.6	6	10
Full Crossing Angle at IP1/5 [μrad]	200	240	290	285
β^*[m]	3.5	1.0	0.6	0.55
ε_N[μm]	2.0	2.6	2.5	3.75

Table 3.1 Important LHC parameters. Listed for 2010 and 2011 are the "peak performances" and for 2012 the expected values. The right most column shows the nominal design values [27, 28, 29].

The LHC is a 27 km long circular collider about 100 m under the surface. Its ring is divided into eight sectors, where each sector consists of an 2.4 km long arc and a straight section. The arcs contain dipole bending magnets, and the approximately 528 m long straight sections serve as Interaction Points (IPs). Four of these regions are

dedicated to the main experiments two others are used for beam cleaning systems to capture off-momentum and halo particles, another for the superconducting RF cavities and one for the beam dumping system. The LHC has two high luminosity experiments, ATLAS [30] (IP1) and CMS [31] (IP5) for proton operation. There are also two low luminosity experiments, LHCb [24] (IP8) for b-physics and TOTEM [32] (IP5). In addition to the proton beams, the LHC can also be operated with ion beams, where the heavy-ion detector ALICE [33] (IP2) is dedicated to explore such nucleus-nucleus interactions. Figure 3.1 gives an overview of the LHC ring.

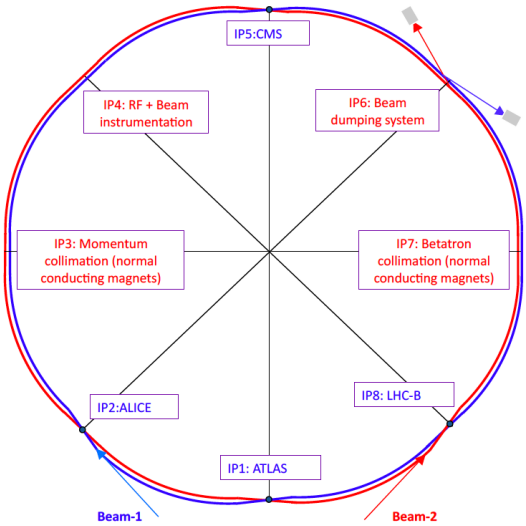

Figure 3.1 The LHC ring with its eight experimental insertions. beam 1 is circulating clockwise and beam 2 counter-clockwise. The beams exchange their positions (inside/outside) in 4 points to ensure that both rings have the same circumference [26].

The LHC produced collisions for the first time in December 2009 at the injection energy of 450 GeV per beam. The early part of 2010 saw the continued ramp-up of beam energy with first collisions at 3.5 TeV per beam on March 30, 2010. The most relevant parameters that were achieved in the last years, and the ones foreseen for the future are listed in Table 3.1. The first proton run ended on 4 November 2010, which was followed by a run with lead ions from November 2010 to the 6th December 2010. Initially the LHC was scheduled to run to the end 2011 before going into a long technical stop necessary to prepare it for running at its full design energy of 7 TeV per beam [34]. However, due to the expected performance improvements in 2011 it was decided that the LHC will run through to the end of 2012, with a short technical stop at the end of 2011. The energy for 2011 was kept to 3.5 TeV per beam, but the bunch intensities were increased and the beams were squeezed to a smaller β^* at the IPs. For 2012 it was decided to run the LHC at 4 TeV per beam, but to keep the 50 ns bunch spacing, with an average number of interactions per bunch crossing of about 27.

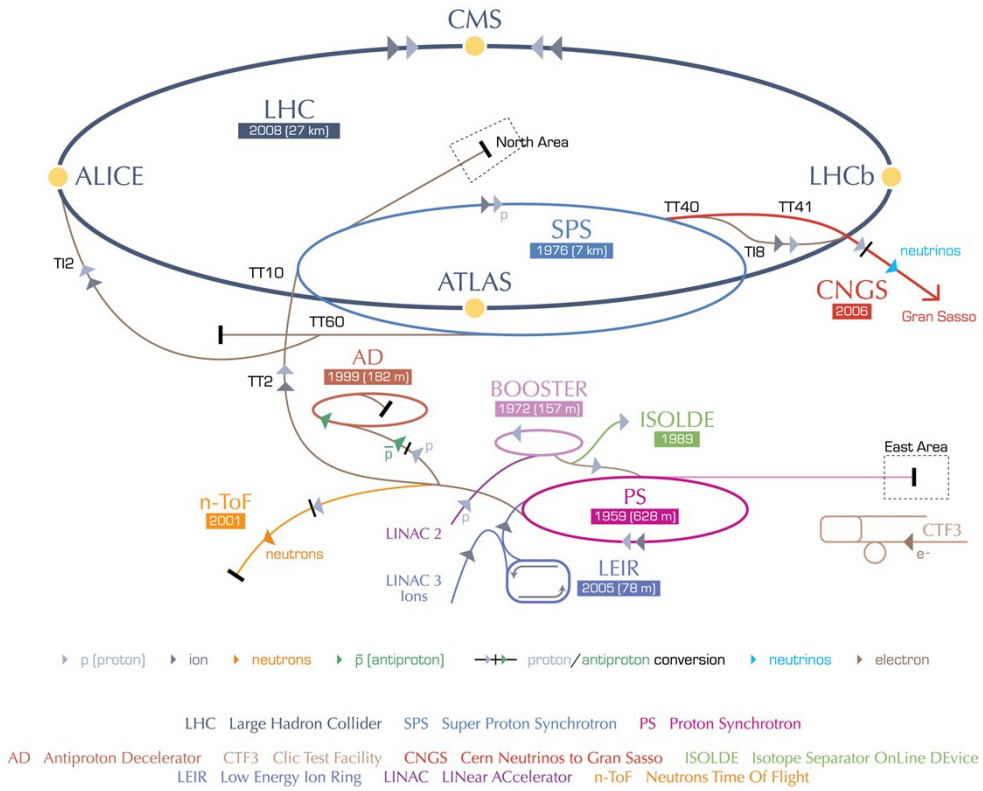

Figure 3.2 The CERN accelerator complex including the LHC and all pre-accelerators [35].

In 2013 the LHC will go into a long shutdown to prepare for higher-energy running starting in 2015, that will bring it closer to its design energy.

3.2 Bringing Proton Beams into Collision

This section will explain how the protons are accelerated at the LHC and finally brought into collision at the IPs.

The first step is the ionization of the gas from a bottle of hydrogen. From there the protons are extracted with an energy of 100 keV. But before they are fed into the LHC ring they need to be accelerated by several different pre-accelerators. Figure 3.2 gives an overview of their location. Each accelerator increases the energy typically by a factor 10-20. The protons are first accelerated to 750 keV using an RF frequency and are then are injected into the 80 m long linear accelerator LINAC2. There the beam is accelerated to an energy of 50 MeV. From the LINAC2 the protons are injected into the Proton Synchrotron Booster (PSB), that increases their energy to 1.4 GeV. The PSB consists of four beam-pipes, each circulating one bunch. From the PSB the particles are injected into the Proton Synchrotron (PS). This happens in two steps: First one *batch* containing one bunch from either of the four PSB beam pipes, then 1.2 s later one ad-

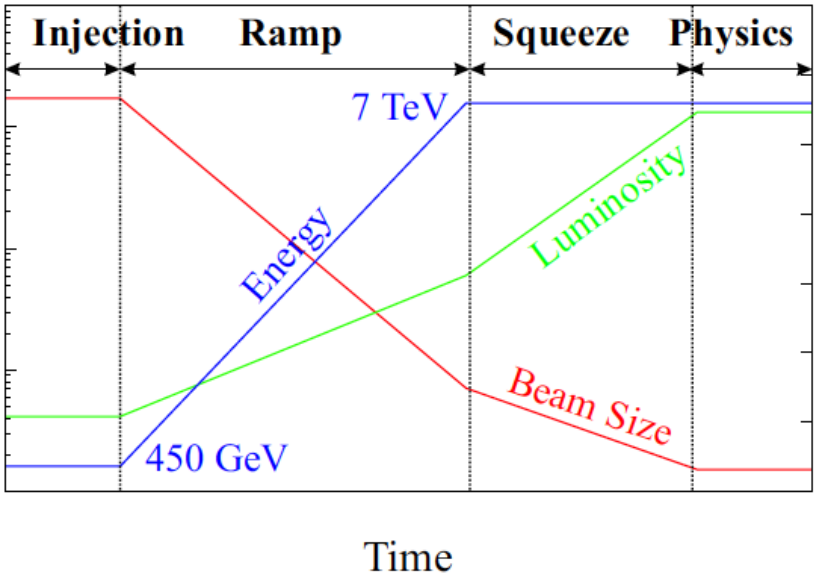

Figure 3.3 Evolution of energy, luminosity and beam size during the filling sequence. The beams are kept separated until the Physics stage is reached, therefore the luminosity evolution represents the value if the beams were colliding head-on [6].

ditional batch containing two bunches. Triple splitting is done at the injection energy, which provides 18 consecutive bunches. The beam is then accelerated up to 25 GeV, where each bunch is further split twice into two to give 72 consecutive bunches. This leaves a 320 ns gap in the bunch train for the rise-time of the ejection kicker. The next step is the Super Proton Synchrotron (SPS), which is a 6.9 km long circular accelerator lying 50 m underground. The SPS is filled with either two, three or at maximum four PS batches of 72 bunches. The protons are finally accelerated to the LHC injection energy of 450 GeV. The injection into the LHC ring from the SPS is done close to IP2 for beam 1 (clockwise) and IP8 for beam 2 (counter clockwise). In the nominal filling scheme this entire process is repeated 12 times per ring to fill the LHC. Then the LHC accelerates the full beam to 3.5 TeV (4 TeV in 2012).

Figure 3.3 shows schematically the evolution of the main beam parameters during a physics fill. Note that the luminosity is just plotted for illustration, since the beams are kept separated until the end of the squeeze. The beams are injected at a β^* of 11m in IP1 and IP5 and 10 m in IP2 and IP8 [6]. Then the beams are *ramped* to high energy, then *squeezed* at the interaction points to a smaller β^*. During ramping the longitudinal momentum of the particles increases, while the transverse component is left unchanged. As explained in Chapter 2.1 this leads to a reduction of the transverse emittance, an effect also known as *adiabatic damping*. A smaller ε in turn leads to a higher luminosity (see Equation 2.13). During the squeeze β^* gets decreased which leads to an additional luminosity enhancement. The separation of the beams at the IPs

is steered with six dipole orbit corrector magnets per plane and beam. Two of them are located further away from the IP and act on each beam separately. They are used for fine-tuning of the offsets. The other magnets are installed closer to the IP and affect both beams at the same time. They are used to generate a crossing angle between the colliding bunches and are also steering the beam-separation in *vdM* scans by creating a local distortion in the beam orbit, which is called *closed orbit bump*.
At the experimental insertions the beams are traveling in a common vacuum chamber for about 120 m. One can easily calculate that for bunches traveling with the speed of light and spaced by 25 ns, around 30 parasitic collisions would take place. Such unwanted collisions would degrade the beam-lifetime and would produce additionally large backgrounds for the nominal collisions. For this reason the beams are colliding with a crossing angle θ_C, that is in the vertical plane for IP1 and IP2, and in the horizontal plane for IP5 and IP8. The values used during the last running periods are shown in Table 3.1. They were chosen large enough to minimize beam-beam long-range encounters that could lead to bunch instabilities. However, as explained in 2.3, they also lead to a luminosity reduction, which is $\approx 21\%$ at nominal values. The present values of β^* are high enough, that the reduction due to the hourglass-effect is negligible, and even at nominal LHC values a reduction will be only of the order of $\approx 1\%$ [6].

3.2.1 LHC Filling Scheme

This section will present an overview of the LHC beam structure. The LHC RF frequency f_{RF} is 400.79 Mhz and the revolution frequency f_{rev} of the protons is 11.245 kHz. This gives a chain of 35640 RF-buckets around the machine which could potentially be filled with bunches. In the nominal filling scheme bunches are spaced by 25 ns, i.e. 40 MHz. Therefore 3564 potential *slots* are available, each of which is given a unique bunch crossing identifier (BCID).
The injections from the SPS have a *bunch train* structure, i.e. a certain number of equally spaced bunches. Between the trains short gaps for the injection kicker magnets must be left in. In addition, a 3 μs abort gap is kept free, in order to allow for a safe abort of the LHC beam. The first BCID after the abort gap is by definition numbered as 1.

Figure 3.4 gives a schematic view of the bunch dispersion for the nominal filling scheme. In practice the LHC is flexible to run with several different filling schemes designed for various purposes. In addition to the nominal 25 ns spacing, the bunch-splitting in the PS allows different bunch bunch spacings: 50 ns, 75 ns and 150 ns. For several reasons the LHC was running in 2011 with a 50 ns bunch spacing for protons, allowing 1782 potential slots and 1380 nominal bunches that can be filled. In general

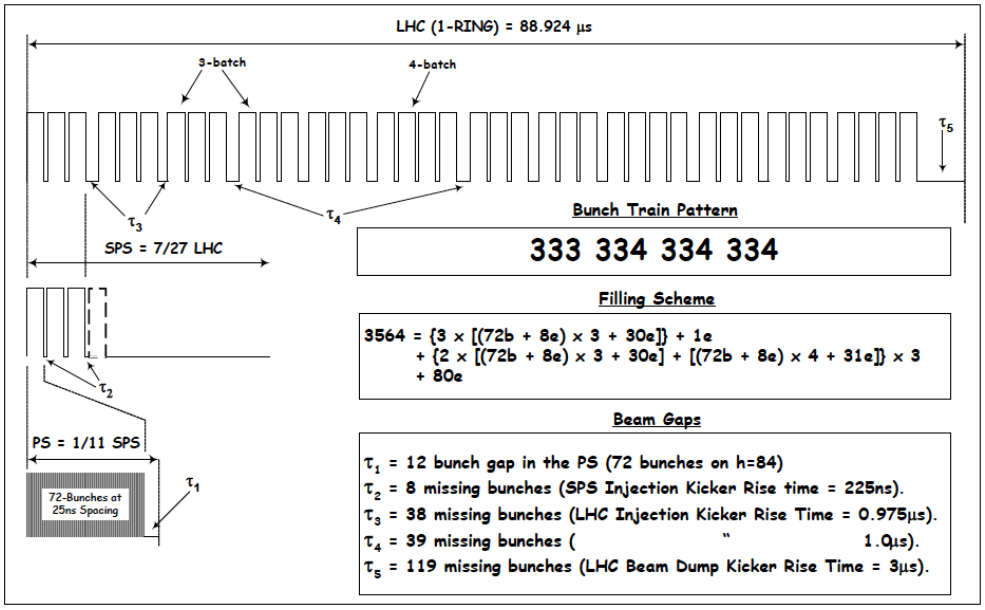

Figure 3.4 Schematic of the bunch dispersion around the LHC ring for the nominal 25 ns filling scheme. The beam is arranged in the form of 39 batches of 72 bunches, where the bunches in each batch are spaced at 25 ns. Between the batches are gaps for the SPS and LHC kicker rise times, which gives a total of 2808 nominally filled bunches in the ring [36].

not all bunches are paired, i.e. colliding and one can define different groups of BCIDs[1]:

- *Paired:* A bunch in both beams in the same BCID.
- *Unpaired isolated:* A bunch in only one beam, with no bunch in the other beam within 3 BCIDs.
- *Unpaired non-isolated:* A bunch in only one beam, with a nearby bunch in the other beam (within 3 BCIDs).
- *Empty:* A BCID without a proton bunch.

3.3 Beam-Related Background at the LHC

Not all rate measured by the LHC experiments is actually coming from *pp* collisions. As in any particle accelerator different backgrounds can contaminate the measurements. This section will give an overview over the most relevant ones, in particular in view of luminosity measurements.

Beam induced backgrounds are *non-collision backgrounds*, which refer to backgrounds measured in the detector, that are not produced in normal *pp* collisions [37]. They are

[1] These definitions are taken from [37] and commonly used within the ATLAS experiment.

in general produced by protons colliding with material upstream of the IP, e.g. the tertiary collimator (TCT) 150 m away of the IP, or with residual gas in the beam-pipe. These collisions induce secondary particle cascades which can reach the detector and produce a signal while they travel from one side to the other. The rate is proportional to the intensity of each beam and depends on the operational conditions of the LHC, like machine optics, collimator settings, residual gas densities and filling scheme. It is observed that this *single-beam background* can be considerably different between the two beams, because e.g. the amount of residual gas on the two sides of the IP may be different, but is however uniform for the bunches in a given beam. According to their production mechanism they can be subdivided into *beam-gas* and *beam-halo*. Where the latter is produced when particles from the beam interact with material upstream of the detector, which causes a "halo" of secondary particles that travel with the beam. Beam-gas background is produced in interactions of the beams with gas particles in the beam pipe.
In general these beam-related backgrounds can be determined from unpaired events, as will be shown later. Other non-collision backgrounds are noise or cosmic rays, they belong to the group of *non-beam-related backgrounds*.
In addition, activity that scales with the luminosity is observed in bunches right after the collisions. This background is called *afterglow*. Even though the rate following a single collision is rather low (around 0.01% of the luminosity, depending on the detector and algorithm) it scales with the bunch pattern and can get significant in fills with larger bunch trains. Its source is not fully understood. But it is believed to be caused by photons from nuclear de-excitation.

3.3.1 Luminosity Lifetime at the LHC

Degradation of emittances and intensities in both beams lead to a time-dependent decrease of the luminosity within an LHC fill. Beam loss happening due to collisions and effects such as emittance blow-up due to scattering of particles with residual gas, or the non-linear part of the beam-beam interaction lead to a luminosity reduction by time. However, a small amount of the emittance blow-up is compensated by synchrotron radiation damping, which leads to a beam size reduction. The luminosity decay can in general be described with an exponential parametrization introducing a parameter called *luminosity lifetime* τ_L that corresponds to the time of a luminosity reduction by a factor $1/e$ of its initial value $\mathscr{L}_0$. The measured luminosity lifetime in 2011 was at maximum $\sim 20\,\mathrm{h}$ [38]. In order to maximize the integrated luminosity one has to decide at what stage of luminosity degradation one has to inject a new fill. Therefore one has to consider the time that is needed to set up a new fill, also called *turn-around time*. Up to now, such an optimization was hardly ever done, because the periods between

fills were often dominated by equipment failures and operational issues. However, the minimum achieved in 2011 at the LHC was 2 h 07 min, which includes the time needed by the pre-accelerators, ramping of the magnets etc..

3.4 Beam Instrumentation

The precise measurement of beam parameters is important for controlling and understanding the machine. The LHC is therefore equipped with several devices, whose tasks are to measure the essential beam properties, to provide diagnosis, and to give information on beam behavior. A summary of the main systems, in particular about the ones relevant for *vdM* scans, will now be given.

3.4.1 Beam Position Measurement

Trajectory and closed orbit measurements are crucial for the operation of accelerators. The LHC is therefore equipped with more than a thousand Beam Position Monitors (BPM) that are located around the two rings. All BPMs measure the beam intensity and position in both, horizontal, and vertical planes. The majority of the monitors are electrostatic button electrode pick-ups, where the electromagnetic signal induced by the passage of the beam allows the determination of the transverse beam position.

3.4.2 Transverse Emittance Measurements

The transverse emittance of the beams can be measured by *wire scanners* and *synchrotron light monitors* designed to observe the particles transverse distributions. A total of eight wire scanners are installed in IP4 in the LHC [39]. A wire scanner device consists of a thin wire which crosses the beam. As the wire passes through the beam, particles that collide with it are producing a cascade of secondary particles with an intensity proportional to the number of beam particles. The secondary particles are intercepted by a scintillator paddle, and a photo multiplier tube coupled to the paddle measures the intensity of the light. These measurements are usually considered as a reference for the calibration of other instruments. However, due to the interaction of the beam with the wire, the wire can get damaged at a certain beam intensity. In the LHC the wire scanners are only intended to be used up to a tenth of the nominal beam intensity [6].
In the LHC each beam is equipped with one synchrotron light monitor in IP4 [40]. The synchrotron light monitor profits from the radiation emitted by the accelerated particles for imaging the transverse beam distribution. The light is transported and focused in an optical line to dedicated cameras that provide an image. This technique avoids any

interception with the beam, but, depending on the beam energy, different synchrotron light sources must be used to generate enough radiation.
Alongside the synchrotron light monitors so called longitudinal density monitor (LDM) are installed. These devices are capable of producing a longitudinal profile from synchrotron light photons with a high time resolution of 50 ps. This allows for the precise measurement of the longitudinal bunch shape and the number of particles in the bunch tail and in the neighboring RF buckets, which is extremely useful to correct the final beam intensity measurements (see Section 3.4.4).

3.4.3 Luminosity Measurements

The LHC is equipped at each IP with luminosity monitors called BRANs (Beam Collision Rate of Neutrals) that complement and cross-check the measurements provided by the experiments [41]. In general they are poorly calibrated, but they are in particular useful for the LHC machine operators to monitor the relative luminosity in case the measurements from the experiments are not available. The interaction rate is measured by monitoring the flux of small angle neutral particles produced by the collisions. The monitors are placed on each side of the IP in the neutral beam absorber (TAN) at IP1 and IP5, where the detector itself is a pressurized gas ionization chamber, and in IP2 and IP8 where lower luminosity is expected the detectors are behind a converter and are based on solid state polycrystalline Cadmium-Telluride sensors.

3.4.4 Beam Intensity Measurements

Recalling Equation 2.13 one main ingredient for the determination of the total luminosity from beam-parameters is the precise knowledge about the bunch population product $n_1 n_2$, where $n_{1(2)}$ denotes the number of protons per BCID in beam 1(2). At the LHC, the bunch current measurement is performed by the Bunch Current Normalization Group (BCNWG) [42]. Intensity measurement are provided by two types of beam intensity monitors: The DC Current Transformers (DCCT) [43] and the Fast Beam Current Transformers (FBCT) [44]. In the long straight section at Point 4 on the vacuum chamber of each circulating beam, two identical and redundant DCCT and two FBCT systems are installed. The DCCTs are based on the principle of magnetic amplifiers. By detecting the magnetic field induced by the moving charge of the beam they give an accurate absolute measurement of the total circulating current in each ring, irrespectively of the time structure of the beam. The FBCTs are designed to measure the bunch population in each of the 3564 nominal slots of each beam using a toroidal transformer which couples inductively to the beam current. They are only sensitive to bunched beams and measure the current above a threshold of about 5×10^8 protons.

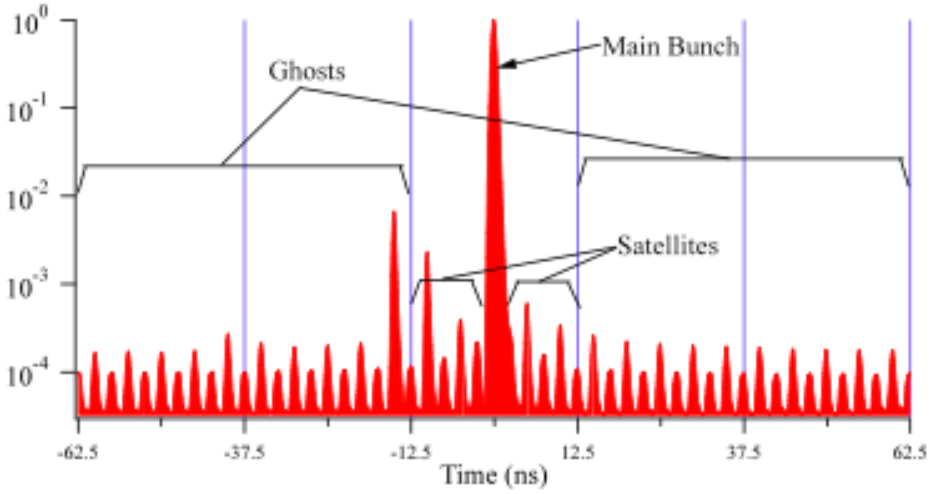

Figure 3.5 Example profile showing the measured charge in five BCID slots is plotted on a logarithmic scale, measured in the heavy ion run 2010 with the LDM [46]. The plot can be used to illustrate the definition of ghosts charge and satellite bunches.

The relative fraction of the total current in each BCID is thus determined by the FBCT and is then normalized to the total scale provided by the DCCT [45].

However, additional corrections for *ghost charge* and *satellite bunches* need to be made. Ghost charge is defined as the total beam population outside the nominally filled 25 ns bunch slots [47]. Within the 25 ns of a nominally filled slot, the *main bunch* occupies only one of ten RF buckets. Bunches that populate any of the other nine buckets are called satellite bunches. Figure 3.5 shows an example profile with satellite bunches around the colliding BCID, and ghost charge populating the BCIDs next to it.

To determine the bunch charge $n_{1(2)}$ in BCID i for beam 1 or beam 2 the ghost charge contribution N_{ghost}, that is included in the total calibrated charge observed by the DCCT $N_{\text{tot}}^{\text{DCCT}}$, but not in the per-bunch population, is first removed from the total bunch population $N_{\text{tot}}^{\text{DCCT}}$. The result is then multiplied by the per-bunch fraction measured in the FBCT:

$$n_{1(2)}(i) = (N_{\text{tot}}^{\text{DCCT}} - N_{\text{ghost}}) \cdot \frac{S_i^{\text{FBCT}}}{\sum_i S_i^{\text{FBCT}}} \tag{3.1}$$

where S_i^{FBCT} is the signal observed by the FBCT in BCID i. The total DCCT charge is further computed as:

$$N_{\text{tot}}^{\text{DCCT}} = \alpha \cdot S^{\text{DCCT}} - N_0^{\text{DCCT}} \tag{3.2}$$

where α is a calibration constant referred to as the DCCT scale factor, S^{DCCT} is the signal observed by the DCCT, and N_0^{DCCT} is the DCCT baseline offset correction. Each

of these quantities have a contribution to the final uncertainty, that will be discussed in the following:

- *DCCT baseline offset:*
  Baseline drifts have a variety of reasons such as temperature drifts, electromagnetic pick-up in cables, mechanical vibrations etc. The baseline offsets can be determined by comparing the average baseline offsets during a period before injection and then again after the beam-dump. The systematic uncertainty from the baseline drifts is taken as the maximum difference in the measured offsets. The baseline offsets vary by at most $\pm 8 \times 10^9$ protons in each beam. Therefore, the associated relative error from the baseline determination decreases when the total circulating charge goes up.

- *DCCT scale variation:*
  The main source of uncertainty on the scaling factor α is the stability over time. To estimate the long-term stability regular calibration checks during technical stops are performed. Other potential sources such as unexpected non-linearities from a potential dependency of the DCCT on the LHC filling pattern or inaccuracy of the commercial current generator used for calibration have been found to be negligible.

- *Bunch-to-bunch fraction:*
  Possible non-linearities on the relative per-bunch population measured by the FBCT system can be checked and estimated by comparing the measurements to those of the ATLAS beam-pick-up (BPTX) system, which also measures per-bunch currents. The variation seen between these systems is taken as a systematic uncertainty.

- *Ghost charge and satellite bunches:*
  The LDMs can be used to measure the relative population of ghost charge within different RF buckets. An independent determination can be provided by the ATLAS Beam Condition Monitors (see Chapter 4.4.1), by measuring the fraction of incoming-beam halo in all but the nominally filled BCIDs, relative to the halo associated with the unpaired bunches in each beam [48].
  Satellite bunches will produce luminosity within the given 25 ns BCID window, but with an offset both in space and time from the nominal IP. In ATLAS they can be detected by extending the tracking and vertexing algorithms to cover a longitudinal distance ± 1 m from the nominal IP. This distance covers the expected satellite interaction points for bunches displaced by up to ± 75 cm which corresponds to a displacement of ± 5 ns, i.e. the four RF buckets next to the nominal bunch.

Chapter 4

The ATLAS Experiment and its Luminosity Measurements

This Chapter will start with a brief overview of the general detector, followed by a description of the different sub-detectors that are used by ATLAS for relative luminosity measurements. Several operational aspects concerning luminosity measurements will be covered in the last sections, where in particular the Online Luminosity Calculator will be described in detail.

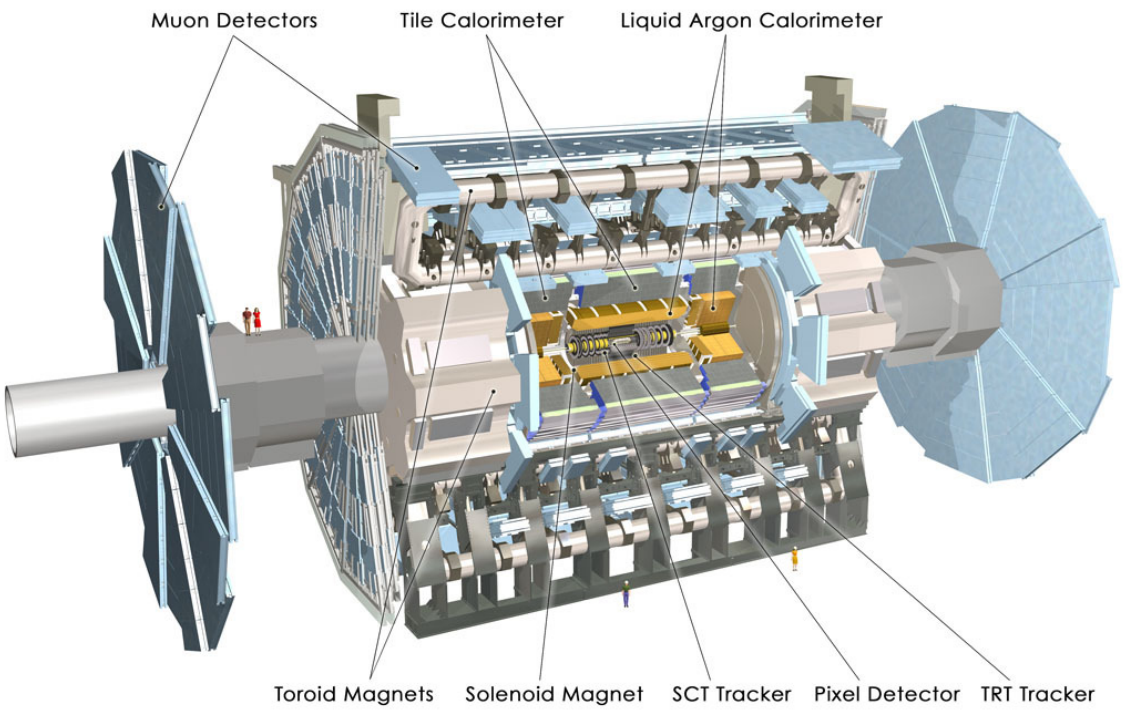

Figure 4.1 The ATLAS Detector [30].

4.1 The ATLAS Detector

The overall detector layout is shown in Figure 4.1. The ATLAS detector covers almost the entire solid angle around the collision point up to a pseudo-rapidity[1] $|\eta|$=4.9. The azimuthal angle ϕ in the right-handed ATLAS coordinate system is defined with respect to the x-axis, which points towards the center of the LHC ring. The z-axis points along the LHC beam 2 direction. Side A of ATLAS is defined as the side of the incoming beam 1, side C is the side of the incoming beam 2. A detailed description of the detector and all its components can be found in [30].

The Inner Detector (ID) of ATLAS is contained within a cylinder of length 7 m and a radius of 1.15 m, surrounded by a solenoidal magnetic field of 2 T. It is designed for tracking of charged particles that is achieved with a combination of semiconductor pixel and strip detectors in the inner part, and straw-tube tracking detectors with transition radiation capability in its outer part. The ID is surrounded by the calorimeter system. A highly granular liquid-argon (LAr) electromagnetic (EM) calorimeter covers the pseudorapidity range $|\eta|< 3.2$. The ATLAS hadronic calorimeters cover the range $|\eta|< 4.9$ using different techniques. Over the range $|\eta|< 1.7$, the iron scintillating-tile technique is used (TileCal). Over the range $1.5 <|\eta|< 4.9$, LAr calorimeters are used. The hadronic end-cap calorimeter (HEC) extends to $|\eta|< 3.2$, while the range $3.1 <|\eta|<$ 4.9 is covered by the forward calorimeter (FCAL).

The calorimetry is surrounded by the muon spectrometer. The air-core toroid system, with a long barrel and two inserted end-cap magnets, generates a large magnetic field volume. Muon detection is achieved with three stations of high precision tracking chambers. The muon instrumentation also includes trigger chambers with very fast time response.

4.2 The ATLAS Trigger

The ATLAS Trigger System is designed to reduce the event rate from the 40 MHz bunch-crossing frequency to an average recording rate of 400 Hz [30]. It has three distinct levels, where each level refines the decision made by the previous level and, where appropriate, applies new selection criteria. The first level-1 is implemented in custom-built electronics, while the High Level Trigger (HLT), that is formed by level-2 and event filter (EF), is almost entirely implemented in software. Level-1 works on a subset of information from the calorimeter and muon detectors. These inputs are used by the level-1 Central Trigger Processor [49] (CTP) to generate the L1 Accept (L1A) decision. The CTP distributes the Luminosity Block number through ATLAS (more on

[1] The pseudorapidity is defined as $\eta = -\ln(\tan(\theta/2))$, with θ being the polar angle with respect to the z-axis.

this later) and provides meta-data for the Luminosity Block, dead-time and pre-scale corrections [50] which are quantities in particular relevant for luminosity determination. The ATLAS dead-time is introduced in the CTP by inhibiting level-1 triggers [51].
The L1A and timing information are sent to the sub-detectors front-ends and a summary information is sent to the level-2 trigger, including the location of the calorimeter clusters or muon tracks, known as the Region-of-Interest (RoI). The level-2 uses fast, dedicated algorithms to accept or reject the event by performing reconstruction with the full granularity data in the RoIs. The maximum level-2 output rate is limited to about 5 kHz.
In case of a level-2 accept, the full event data is read out by the EF and more refined algorithms are performed, in order to make the final trigger decision, i.e. to accept or reject the event.

4.3 The Beam Pick Ups - BPTX

The ATLAS BPTX are electro-static button pick-up detectors, located 175 m away on either side of IP1 [52]. Their precise timing allows to produce a signal each time a bunch passes through ATLAS. This signal is used to provide a level-1 filled-bunch trigger and is also used for general monitoring of the LHC bunches. Their relative per-bunch intensity measurement, is also used to cross-check the measurements by the FBCT (as mentioned in Section 3.4.4).

4.4 Luminosity Sub-Detectors of ATLAS

The ATLAS strategy to understand and control the systematic uncertainties affecting the luminosity determination is to compare results of several independent approaches. A large number of sub-detectors are used for this purpose. Their measurements of the inelastic *pp* rate are in general performed with multiple *event counting* algorithms, that are different in their statistics and background sensitivity (more on this in Chapter 5.3.1). Out of this variety of data, the ATLAS luminosity community chooses one preferred detector and algorithm, that is considered the most reliable. This measurement is then providing the official ATLAS luminosity and is called *ATLAS preferred*. ATLAS further distincts between the *online*- and *offline*- preferred. The offline-preferred is used for physics analysis, while the online-preferred is the one sent to the LHC in order to provide fast feedback on the luminosity conditions at IP1.
Many of those sub-detectors have proven to provide very useful cross-checks but are not suited for a precision luminosity determination, nor can they be absolutely cali-

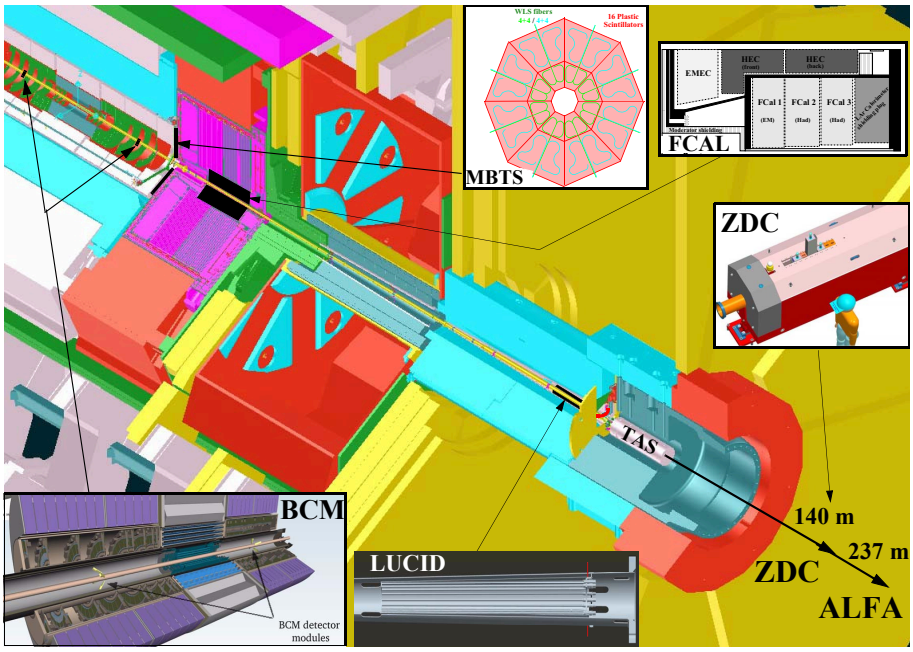

Figure 4.2 Positions of the ATLAS luminosity detectors and distance from the interaction point. All having different acceptances, systematic uncertainties and sensitivity to background.

brated. Long-term stability, within changing running conditions and for a large span of luminosity, independence of dead-time and the ability to determine the luminosity at a per-bunch level, are requirements for the device that is supposed to be the ATLAS preferred one.

Picture 4.2 shows the position of the main luminosity detectors within the ATLAS detector. The positioning of the detectors versus the distance to the IP ranges from ± 1.84 m for the BCM to ± 140 m for the ZDC. Most detectors have in common that they have two stations on either side of the IP, which allows to perform a coincidence requirement as will be explained later. One can subdivide "online" and "offline" measurements. Offline algorithms use data triggered and read out through the standard ATLAS data acquisition system and must therefore also be corrected for dead-time in order to measure the delivered luminosity. They do not have the necessary rate to measure luminosity independently for each BCID under normal physics conditions [2]. Online measurements are provided by detectors with fast read out electronics, that allow luminosity algorithms to be applied in *real time* and in general per BCID separately. Such measurements are providing instantaneous rates, typically of the order of 1 Hz that are used to provide fast diagnostic signals to the LHC and to monitor the luminosity evolution versus time. The luminosity is also integrated in intervals of the order of minutes, to be used for physics analysis (see more in section 4.6). The two main luminosity sub-detectors BCM and LUCID provide such online measurements. They are fast detectors with electronics capable of making per-bunch luminosity mea-

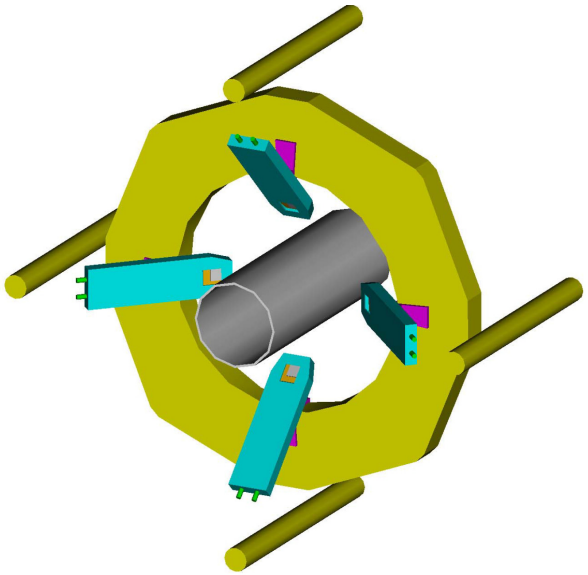

Figure 4.3 Schematic illustration of 4 BCM stations mounted on the ATLAS beam pipe support structure (here shown for side A, an identical station is mounted on side C) [53]. The horizontal and vertical modules deliver separate luminosity measurements.

surements with almost no internal dead-time. Their FPGA-based front-end electronics run autonomously from the main ATLAS data acquisition system, and in particular are not affected by any dead-time from the CTP. The following will give a brief introduction to each of the systems, with an emphasis on these two main luminosity sub-detectors.

4.4.1 The Beam Condition Monitors - BCM

The primary goal of the ATLAS Beam Conditions Monitor (BCM) system is to monitor beam conditions close to the IP and to protect the ATLAS detector against damaging beam losses [54]. If several protons hit the TAS[2] collimators or the beam pipe this could result in an enormous instantaneous rate of secondary particles that might cause detector damage. The BCM consists of two sets of four modules on each side of the IP. The modules are mounted symmetrically at a positions of $z_{bcm} = \pm 1.84$ m and at a radius of 55 mm with respect to the beam axis. The sensors are made of 500 μm thick radiation hard polycrystalline chemical vapor deposition (pCVD) diamonds. With respect to the beam axis the sensors are mounted with a tilt of 45°. Figure 4.3 shows a sketch of the side-A station. The very low acceptance of the BCM requires that they are sensitive to single minimum ionizing particles (MIPs). A fast readout (≈ 2 ns shaping time) enables measurements on a per-bunch level and allows to measure time of

[2]The Target Absorber Secondaries collimators (TAS) are copper blocks, installed at z=±18 m from the IP. They are used to protect parts of the detector.

flight and pulse amplitudes. The precise timing and exact location of the BCM enables it to distinguish collision from background events. Collisions originating at the IP give signals in both detector stations simultaneously (*in-time hits*). Events originating at $|z| > |z_{bcm}|$, e.g. beam-gas, will hit both detector stations with a time difference of 12.5 ns. They are called *out-of-time hits* and can be used for background studies.
The signals of the 8 modules are routed via 14 m long coaxial cables to the readout electronics [55]. In order to expand the dynamic range each signal is split into a high and low amplitude channel. The low-threshold channels have MIP sensitivity and are thus suited for luminosity determination. The high threshold produces signals only above very high multiplicities [56]. All signals are then transmitted over 70 m optical fibers to the ATLAS USA15 cavern. There one readout path uses the low-threshold channels of the four horizontal modules, which is called BCM-H . Another uses the low-threshold channels of the vertical modules, which is called BCM-V . In this way the BCM delivers two independent measurements, that can be used for opposite redundancy and cross-checks. The absolute luminosity calibration and the luminosity measurements of the BCM is subject of this thesis.

4.4.2 The Cherenkov Detector - LUCID

The LUCID detector is the only detector of ATLAS that is dedicated solely for relative luminosity measurements. It consists of two stations that are positioned symmetrically around the beam pipe at about ± 17 m from the ATLAS IP [57]. Each station consists of 20 aluminum tubes that are arranged along the beam line. The tubes are 1.5 m long and have a diameter of 15 mm. They are filled with a low refractive index gas[3]. Charged particles entering a tube with a momentum larger than the Cherenkov threshold in the gas, emit light at an angle of about 3° with respect to their flight direction. The produced photons undergo reflections on the inner tube walls until they reach the end of the vessel, where they are read out by a photomultiplier (PMT). If the PMT signal is above a certain threshold, the tube has registered a hit. The signals of all tubes are sent to the readout system where the dedicated LUMAT card is able to apply fast online luminosity algorithms at the per-bunch level.

4.4.3 The Minimum Bias Trigger Scintillators - MBTS

The MBTS consist of two sets of sixteen scintillation counters which are installed on the inner side of the end-cap calorimeter cryostats. They cover a large area in pseudorapidity and the full azimuthal angle. Light emitted by each scintillator segment is

[3] On 30 July 2011, the LUCID operators removed the radiator gas from the Cherenkov tubes and ran for the rest of the 2011 physics run without gas. This acceptance reduction was motivated by several factors, in particular because of the increasing interaction rate the measurements started to saturate.

collected by wavelength-shifting optical fibers and guided to a PMT. The main purpose of the MBTS was to provide a trigger on minimum collision activity. It has been extremely valuable in early data taking at luminosities below $10^{33}\text{cm}^{-2}\text{s}^{-1}$ due to its high acceptance and efficiency. However, this in turn lead to early saturation, and the detector is therefore not suited as a luminosity detector anymore.

4.4.4 Zero Degree Calorimeter - ZDC

The ZDC consists of six modules with tungsten absorber plates and quartz strips. Cherenkov-light that is emitted in the quartz fibers is read out by PMTs [58]. For *pp* running the ZDC is mainly used for forward particle studies. Their role as a luminosity monitor is only relevant within the ATLAS heavy ion (HI) program, where they additionally provide triggers and measure the centrality of the collisions.

4.4.5 Primary Vertex Counting in the ID

The Inner Detector is used to measure the momentum of charged particles over a pseudorapidity interval of $|\eta|< 2.5$. It is also possible to give a luminosity estimate by counting the number of primary vertices produced in inelastic *pp* collisions. However, vertex counting suffers from nonlinear behavior with an increasing number of interactions per bunch-crossing, which makes a precision luminosity determination using this technique difficult [2].

4.4.6 Calorimeters - FCAL and TileCal

In order to provide a cross-check of the stability and μ-dependence of the main luminosity sub-detectors, an independent measure of the luminosity has been developed using the ATLAS calorimeters. The PMT current drawn in TileCal modules and the current drawn across the liquid argon gaps in the FCAL modules is used for this purpose. These measurements provide the average particle rate over longer time scales, and are thus not on a per-bunch level [2]. Another draw-back is that an absolute calibration in a *vdM* scan of these sub-detectors was not possible up to now, since the luminosity in the scans is below their minimum sensitivity [59]. However, they can be cross-calibrated by comparing the currents to an absolutely calibrated measurement of another sub-detector.

4.5 ATLAS Time Unit - Luminosity Blocks

The time unit in which ATLAS data is recorded is called Luminosity Block (LB). It is an interval of normally roughly 1 min, during which the luminosity is supposed to

remain stable. To properly estimate the delivered luminosity, a LB transition is also issued when e.g. trigger prescale settings are changed. The LB-concept allows to time-average and thus makes comparisons between measurements of different sub-detectors possible. The CTP of the ATLAS level-1 trigger system issues this signal with the corresponding time stamps. All data recorded in ATLAS is labeled with a Luminosity Block Number (LBN) and the ATLAS Run Number (RunN). A LB-interval can then offline be assigned a data quality flag, in order to mask corrupt data if e.g. a sub-system had unsatisfactory performance. Data from such a LB can than easily be discarded from physics analysis.

In a typical cross-section measurement, the cross-section of a process can be calculated by the number $N_{x,i}^{\text{obs}}$ of signal events that have passed certain selection cuts, minus the number of background events $N_{x,i}^{\text{bkg}}$, divided by the efficiency $\varepsilon_{x,i}$, which includes detector acceptance, trigger- and reconstruction efficiency, and the integrated luminosity:

$$\sigma_x = \frac{\sum_i N_{x,i}^{\text{obs}} - N_{x,i}^{\text{bkg}}}{\sum_i L_i \cdot \varepsilon_{x,i}} \tag{4.1}$$

The sum needs to be taken over all the LBs that have been analyzed (even if a given interval does not contribute any events that have passed the selection cuts). The average luminosity in each LB is multiplied by the LB duration to provide the integrated luminosity delivered in that LB. Each LB value needs to be dead-time and pre-scale corrected. These corrections are also recorded on a per-LB basis.

4.6 Online Luminosity Data-Flow

Luminosity measurements at a particle collider serve two main purposes: Monitoring of the conditions at the experimental insertions, and storage of the data for offline use e.g. for physics analysis. While for monitoring the luminosity is preferred in *real time*, the offline luminosity needs to be stored in well defined time intervals, i.e. in LBs in the case of ATLAS. In order to be able to compare the measurements from all previously described luminosity sub-detectors a central and coherent processing of their data is required. In ATLAS this is achieved with a software application called *Online Luminosity Calculator* (OLC) [60] which has been developed along the work of this thesis. Its main tasks are to translate the *raw event counts* of the luminosity sub-detectors into luminosity in units of $\text{cm}^{-2}\text{s}^{-1}$, to integrate these measurements along with data from beam-instrumentation over the duration of LBs, and to publish this data in a coherent format for online and offline usage. A schematic view of the online luminosity data-flow is given in Figure 4.4.

The luminosity sub-detectors publish event counts using multiple algorithms to dif-

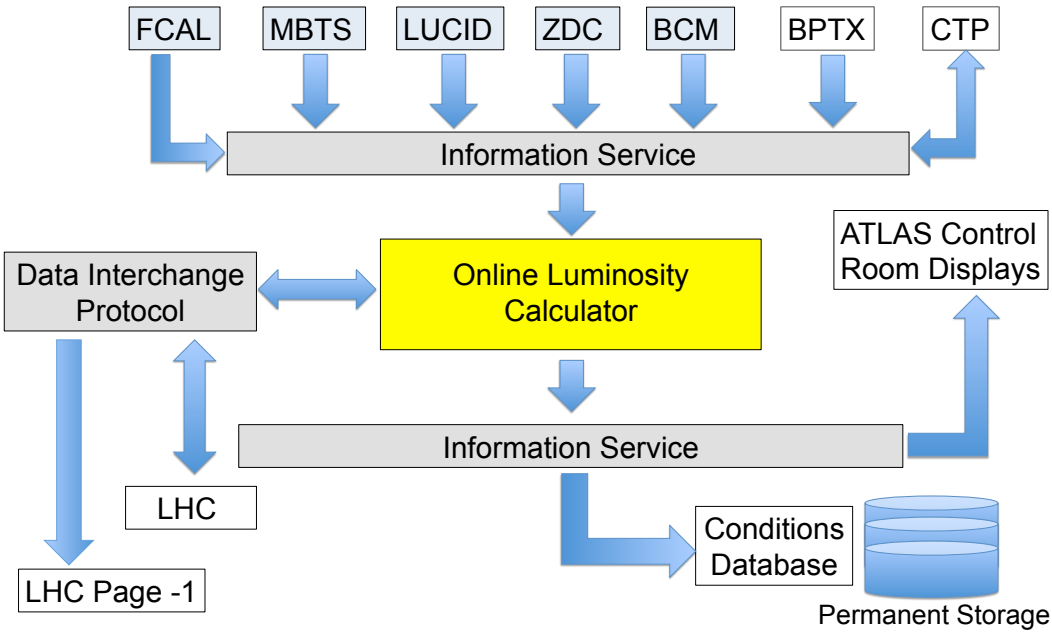

Figure 4.4 Online luminosity data-flow. The OLC collects the raw luminosity from the sub-detectors and values from beam instrumentation from the LHC. Here, the application of calibration constants, time integration and normalization is performed and the data are sent to monitoring displays in the ATLAS Control Room, to the LHC and for permanent storage to the conditions database.

ferent servers on the Information Service[4] (IS) [61]. Most of these measurements are published multiple times, in different format and with different integration time, depending on the ability of the corresponding detector. One has to distinguish between the following publications:

- *Instantaneous BCID-Blind*: The event-counts are published roughly every second, integrated over all BCIDs. (Provided by all sub-detectors)
- *LB-Averaged BCID-Blind*: The event-counts are accumulated by the sub-detector per Luminosity Block, integrated over all BCIDs. (Provided by almost all sub-detectors)
- *LB-Averaged Per-Bunch*: Vector of event-counts per BCID, accumulated per Luminosity Block. (Provided only by LUCID and BCM)

The OLC collects all these publications from IS, together with data from the LHC beam-instrumentation that is published via the Data Interchange Protocol[5] (DIP). In the OLC the raw-event counts are translated into luminosity values in units of $\mathrm{cm}^{-2}\mathrm{s}^{-1}$. The luminosity-calibration constants, necessary for this calculation, have been previously determined in *vdM* scans, and are retrieved by the OLC from the ATLAS online database. Details on the calculation will be given in the next Chapter.
Upon the publication of a LB-object, that is issued by the CTP, the OLC calculates Luminosity Block averages from instantaneous quantities. To illustrate this Figure 4.5 shows a simplified schema of how LB-averaged luminosity is calculated from instantaneous raw counts in the OLC. The luminosity calculation is performed on the integer BCID-blind measurements, as well on per-bunch vectors. Where from the latter a so-called *PHYS* quantity is derived. This quantity contains the luminosity averaged over only the colliding bunches[6], and is thus the most precise method, as background from non-colliding BCIDs is removed.

The variety of data is published by the OLC in a coherent format on a dedicated IS server. Instantaneous values are published with a frequency of 1 Hz, LB-averaged quantities corresponding to a specific LB are first gathered and published as soon as the next LB object is received. Figure 4.6 shows a screenshot of an IS monitoring tool. The top box shows the list of luminosity objects that is published by the OLC on the IS-server. One algorithm, in this case from LUCID, is selected, and in the bottom box

[4] IS is an ATLAS specific software which allows information exchange between different online applications. The information is held on dedicated IS-servers, to which clients can publish, read, and subscribe for information

[5] DIP is a simple and robust point to point, publish/subscribe system which is used LHC wide.

[6] Where the information on which BCIDs are colliding is taken from the *Bunch-Group* publication of the level-1 CTP.

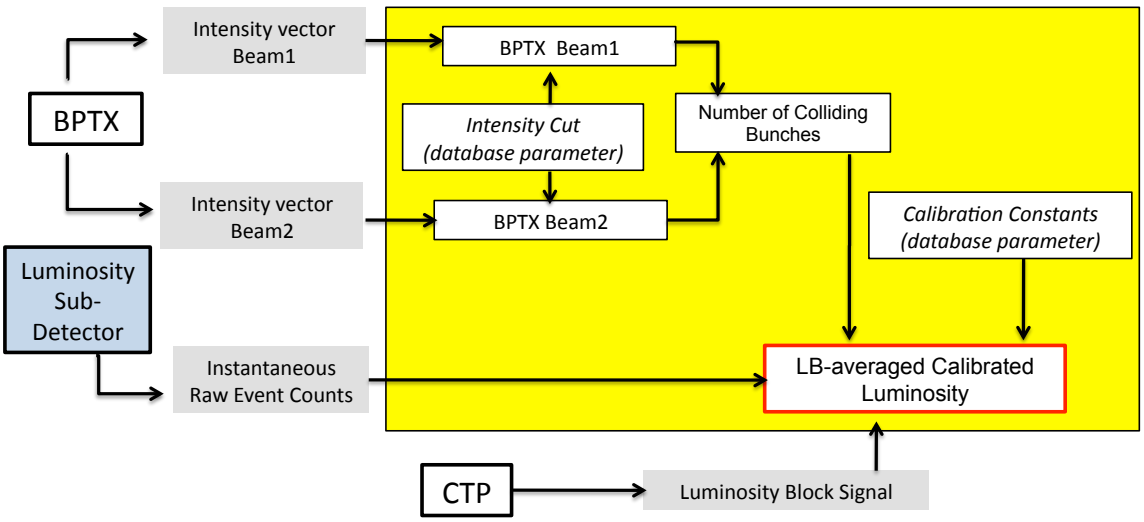

Figure 4.5 Simplified schema of how LB-averaged luminosity is calculated from instantaneous raw counts in the OLC. The yellow box indicates OLC internal quantities that can optionally be published to IS. From the BPTX intensities the OLC creates two objects containing the intensities per beam with a noise cut applied. From the noise suppressed intensities, an integer quantity containing the number of colliding bunches is calculated. Together with a calibration constant, that is defined in the ATLAS online database, the instantaneous raw event counts from a given sub-detector are then translated using a specific OLC-class into instantaneous luminosity. Another OLC object receives the LB-signal from the CTP and averages the instantaneous luminosity over the time of two subsequent LB publications and thus calculates a LB-averaged luminosity quantity.

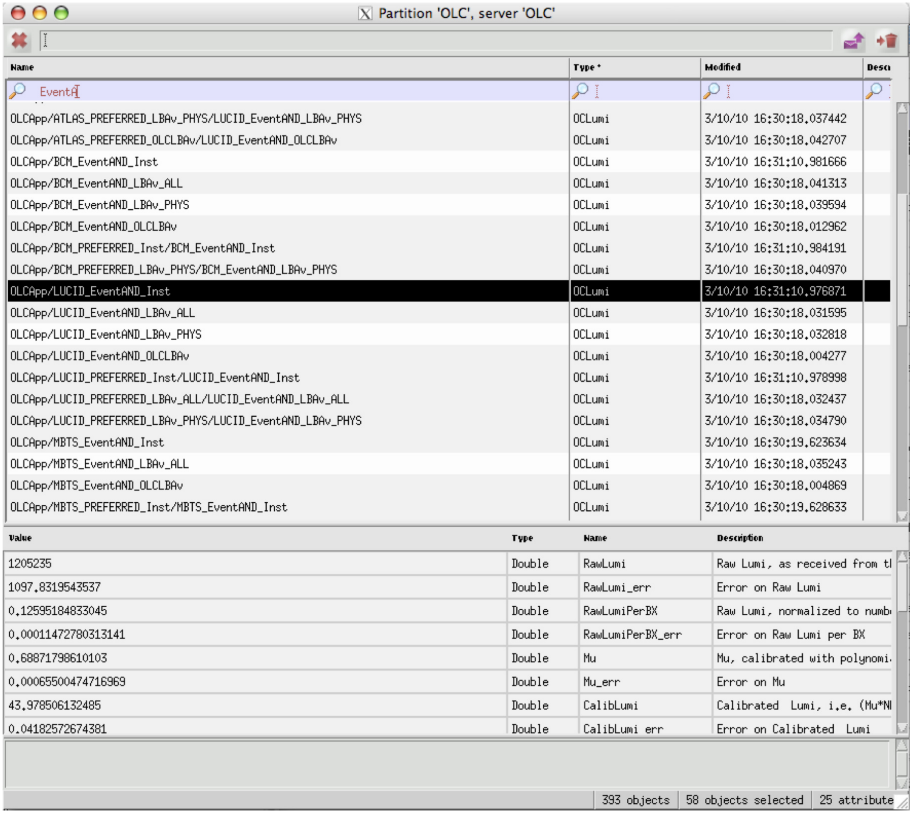

Figure 4.6 Screenshot of luminosity data published in the OLC partition, viewed with the monitoring tool is_monitor. The objects of type OCLumi contain all relevant information regarding the luminosity measurement of the corresponding detector-algorithm. This includes the calibrated luminosity, raw-event counts, calibration constants, etc.

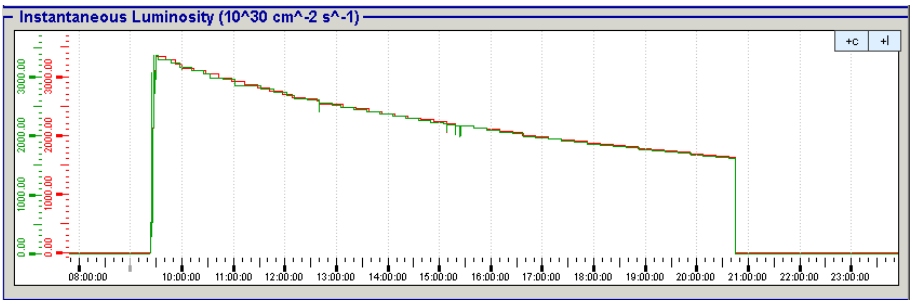

Figure 4.7 DCS screenshot of instantaneous luminosity reported through the OLC in LHC fill 2216. In red is the luminosity measured by BCM Event-OR and in green that of LUCID Event-OR . Optional, the values of different sub-detectors can be switched on and off in these displays. Occasional dips in the measurements can appear if e.g. if the instantaneous number of colliding bunches from the BPTX is not correctly estimated and thus the measurements get a wrong normalization.

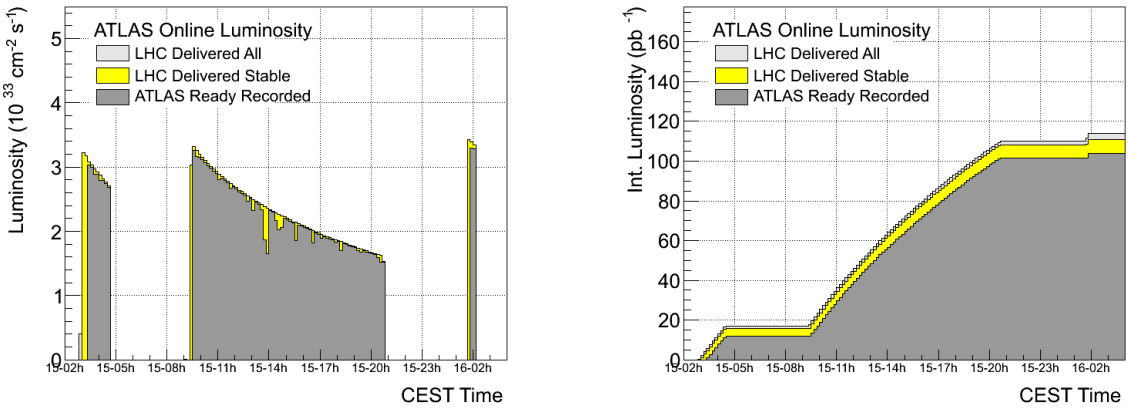

Figure 4.8 Instantaneous (left) and integrated (right) luminosity, measured in ATLAS on Oct 15th. These plots are reconstructed from the OLC data that was stored to COOL and are published the Data Summary Page [62].

the attributes corresponding to that object are shown. The luminosity object contains amongst the calibrated luminosity and its statistical error, also the initial raw counts, the LBN and RunN, start- and end- time of the corresponding LB, and also a quality flag.

For monitoring purposes including time trends this data is also sent to slow control displays in the ATLAS control room (ACR) where it is also stored in the ATLAS online-monitoring archive.

An example screen-shot as it is displayed in the ACR is shown in Figure 4.7. Various control panels, including ones showing ratios of different luminosity measurements, allow the shifter to perform fast online diagnostics and to compare the measurements from different sub-detectors. A number of instantaneous measurements is

also transmitted via DIP to the LHC. These measurements are providing fast feedback on the luminosity conditions at IP1 and are is also used in collision optimization at the IP, which becomes in particular relevant in *vdM* scans. Also via DIP the *online preferred* algorithm is also sent to the LHC Page-1 [63].

LB-averaged luminosities and beam parameters, such as the beam currents and the LHC bunch-pattern, are permanently stored on the ATLAS conditions database. Also the raw event counts are stored, in order to allow offline background correction and re-calibration, in case the calibration constants have changed. The raw event counts are also relevant for the analysis of *vdM* scans. Example diagnostic plots from online data are shown in Figure 4.8. They are taken from the Data Summary Page [62], which serves as a historical summary of the ATLAS data recorded.

Chapter 5

Absolute Luminosity from Beam Parameters with *vdM* Scans

As already mentioned in Chapter 2.4 it is possible to obtain the absolute luminosity directly from beam parameters, without the *a priori* knowledge of any physics cross-section. For the derivation of this method it is useful to recall the general definition of luminosity. A simplified case for a bunch crossing is shown in Figure 5.1. The luminosity can be expressed from geometry and the particle flux per time unit:

$$\mathscr{L} = \frac{n_1 n_2 f_r}{A_{\text{eff}}} \tag{5.1}$$

The revolution frequency f_r is in general well known. The number of particles $n_{1(2)}$ can be measured by dedicated beam charge monitors (see Chapter 3.4.4), while the transverse area of beam overlap A_{eff} is more delicate to determine. As explained previously emittance measurements can be performed by different profile monitors such as wire scanners or synchrotron light monitors. But since they cannot be located at the collision points a precise knowledge of the β function is required to extrapolate the results to the interaction region. However, in the year 1968 Simon van der Meer has proposed a pioneering idea how to measure A_{eff} which he described in [64]. This method is known as *van der Meer- (vdM-)* or *beam separation-* scans and will be summarized in the following section.

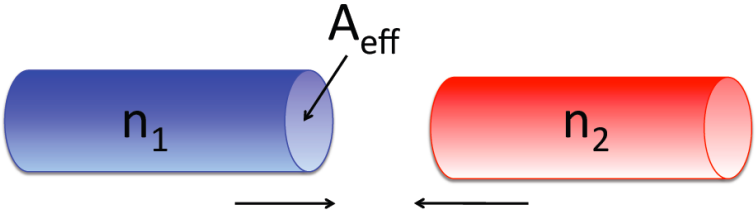

Figure 5.1 Two colliding bunches with bunch populations n_1 and n_2 and an affective overlapping area A_{eff}.

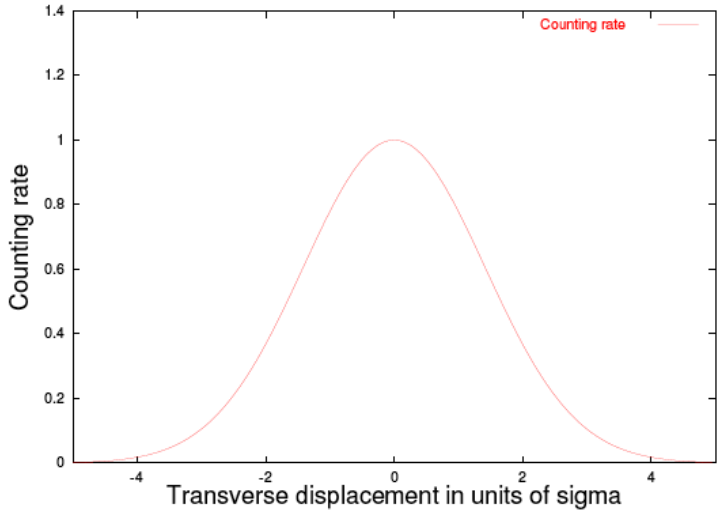

Figure 5.2 Example scan curve showing the counting rate measured by a luminosity monitor versus the transverse displacement of the beams [7].

5.1 Historical Formalism

The Intersecting Storage Rings (*ISR*) was the world's first *pp* collider. The beams were brought into collision with a large crossing angle of $\approx 15^\circ$ in the horizontal plane [65]. Since the beams were unbunched ("coasted") the luminosity was independent of the beam dimension in the plane of the crossing angle[1]. Simon van der Meer proposed that it is possible to measure the effective[2] vertical height h_{eff} of the colliding ISR beams by observing the counting rate R in a suitable monitor system, while scanning the two beams vertically through each other. If ρ_1 and ρ_2 are the particle density functions of the vertical coordinate y, he defines h_{eff} as:

$$h_{\text{eff}} = \frac{\int \rho_1(y)\mathrm{d}y \int \rho_2(y)\mathrm{d}y}{\int \rho_1(y)\rho_2(y)\mathrm{d}y} \tag{5.2}$$

De-placing one beam by δy with respect to the other one can express the counting rate R as:

$$R(\delta y) = C \int \rho_1(y)\rho_2(y-\delta y)\mathrm{d}y, \tag{5.3}$$

where C is an unknown constant, including the interaction cross-section and the acceptance of the counting monitor.

An example scan curve showing the rate versus the displacement is shown in Figure 5.2. Calculating the area under the curve by integrating over $\mathrm{d}\delta y$ one gets:

[1] In the plane of the crossing angle all particles of the one beam intersect all particles of the other beam.

[2] "Effective" because the beam profiles do not have sharp defined edges.

$$A = \int R(\delta y)\mathrm{d}\delta y = \int [C \int \rho_1(y)\rho_2(y-\delta y)\mathrm{d}y]\mathrm{d}\delta y = C \int [\rho_1(y) \int \rho_2(y-\delta y)\mathrm{d}\delta y]\mathrm{d}y \tag{5.4}$$

Since the integrals are calculated over the entire region where the integrands are non-zero one gets:

$$\int \rho_2(y-\delta y)\mathrm{d}\delta y = \int \rho_2(y)\mathrm{d}y, \tag{5.5}$$

with R_0 at $\delta y = 0$:

$$R_0 = C \int \rho_1(y)\rho_2(y)\mathrm{d}y \tag{5.6}$$

the effective height is:

$$h_{\mathrm{eff}} = \frac{\int [\rho_1(y) \int \rho_2(y-\delta y) d\delta y]\mathrm{d}y}{\int \rho_1(y)\rho_2(y)\mathrm{d}y} = \frac{\int [\rho_1(y) \int \rho_2(y)\mathrm{d}y]\mathrm{d}y}{\int \rho_1(y)\rho_2(y)\mathrm{d}y} = \frac{\int \rho_1(y)\mathrm{d}y \int \rho_2(y)\mathrm{d}y}{\int \rho_1(y)\rho_2(y)\mathrm{d}y} \tag{5.7}$$

Expressed in rates:

$$h_{\mathrm{eff}} = \frac{\int R(\delta y)\mathrm{d}\delta y}{R_0} \tag{5.8}$$

which is the fundamental statement of S. van der Meer [64]:

> *"One of the two beams is displaced vertically with respect to the other one, and the counting rate in the monitor is plotted versus displacement. A bell-shaped curve will result with its maximum at zero displacement (...) irrespective of beam shape* h_{eff} *is equal to the area under this curve, divided by the ordinate for zero displacement."*

5.2 Extension to Bunched Beams

At the ISR the luminosity depended only on the beam dimension in one plane. At the LHC, however, bunched beams are colliding and therefore the measured counting rate depends on both horizontal and vertical beam sizes. The main assumption in this more general case is that the density distributions can be factorized, and two scans along the transverse planes are sufficient. If one assumes that the beam density functions are uncorrelated one can write:

$$R(\delta x, \delta y) = R_x(\delta x)R_y(\delta y) \tag{5.9}$$

By scanning the two transverse planes, one gets a direct measurement of the transverse effective beam sizes and therefore of the effective area A_{eff}:

$$A_{\text{eff}} = \frac{\int R_x(\delta x)\mathrm{d}\delta x}{R_x(0)} \frac{\int R_y(\delta y)\mathrm{d}\delta y}{R_y(0)} \tag{5.10}$$

The convolved transverse width per plane of the two beams can be written as:

$$\Sigma_u = \sqrt{\sigma_{1u}^2 + \sigma_{2u}^2} = \frac{1}{\sqrt{2\pi}} \frac{\int R_u(\delta u) d\delta u}{R_u(0)} \quad \text{where } u = x, y \tag{5.11}$$

Inserting 5.10 into 5.1 one gets for the luminosity per bunch:

$$\mathscr{L} = \frac{n_1 n_2 f_r}{2\pi \Sigma_x \Sigma_y}, \tag{5.12}$$

which is equivalent to the result derived in Equation 2.13. It is worth mentioning that in case of a crossing angle, the *vdM* scan measures directly the correct effective beam size, including the effect of a crossing-angle for scans performed exactly in the crossing plane [6].

5.2.1 Extension to Double-Gaussian Beams

In hadron machines the particle distributions in the beams often have non-Gaussian tails. In this case they are better described by a double-Gaussian density function of the form:

$$R(\delta u) = C \cdot [f_a \cdot \mathrm{G}(u, \sigma_a, \mu = 0) + (1 - f_a) \cdot \mathrm{G}(u, \sigma_b, \mu = 0)] \tag{5.13}$$

where u is the transverse coordinate, μ the common mean, C an overall normalization constant, σ_a the standard deviation of the core Gaussian, σ_b the standard deviation of the tail Gaussian, and f_a is the relative fraction of the core Gaussian in $R(\delta u)$. One gets:

$$R(0) = \frac{C}{\sqrt{2\pi}} \left[\frac{f_a}{\sigma_a} + \frac{1 - f_a}{\sigma_b} \right] \tag{5.14}$$

$$\text{with } : C = \int R(\delta u)\mathrm{d}\delta u \tag{5.15}$$

and thus for the convolved transverse beam widths as defined in Equation 5.11:

$$\Sigma_x = \left[\frac{f_a}{\sigma_a} + \frac{1 - f_a}{\sigma_b} \right]_x^{-1} \tag{5.16}$$

$$\Sigma_y = \left[\frac{f_c}{\sigma_c} + \frac{1 - f_c}{\sigma_d} \right]_y^{-1} \tag{5.17}$$

where σ_a, σ_b, σ_c, σ_d, are the parameters of the double Gaussian representing the convolution integrals $R_x(\delta x)$ and $R_y(\delta y)$ along the $x-$ and $y-$ axis, respectively.
It is not fully understood, what caused double-Gaussian beam shapes. There are many mechanisms that could be responsible. At low energy they are generally caused by *intra bunch scattering*, i.e. interactions of particles within the bunch. Often they are also caused by instabilities in the injector chain.

5.3 From Raw Counts to Luminosity

As explained in Section 4.4, ATLAS uses a variety of different detectors and algorithms to measure and monitor the luminosity. Each of these algorithms, once calibrated, should be able to extrapolate the absolute luminosity measurement of the *vdM* scan to any other luminosity scenario. If one takes R_{inel} to be the rate of inelastic pp events, σ_{inel} the pp inelastic cross-section, f_r the revolution frequency of the bunches, and μ to be the average number of pp-collisions per bunch-crossing one can write Equation 2.1 as:

$$\mathscr{L} = \frac{R_{\text{inel}}}{\sigma_{\text{inel}}} = \frac{\mu f_r}{\sigma_{\text{inel}}} \tag{5.18}$$

A certain sub-detector with efficiency ε will only see a subset of the events:

$$\mathscr{L} = \frac{\varepsilon \mu f_r}{\varepsilon \sigma_{\text{inel}}} = \frac{\mu_{\text{vis}} f_r}{\sigma_{\text{vis}}} \tag{5.19}$$

The index "vis" labels a *visible value*. μ_{vis} is therefore a measurable quantity and $\sigma_{\text{vis}} = \varepsilon \sigma_{\text{inel}}$ can be seen as the calibration constant for the absolute luminosity of a given detector-algorithm. In general, this equation is valid only in the case of a linear response of the detector with respect to μ, otherwise corrections for the non-linearity must be taken into account.
This section will first introduce the different types of *event counting algorithms*. It will then be explained how μ_{vis} is determined from the raw algorithm counts, and finally how σ_{vis} is extracted, once the peak rate and the convolved beam sizes are determined within a *vdM* scan.

5.3.1 Luminosity Algorithms

Most of the luminosity detectors of ATLAS consist of two symmetric detector arms, placed on each side (A and C) of the interaction point. Typically each side is further divided into a number of readout segments, each with a separate readout channel. A threshold is applied to the analogue signal output of each readout channel. Particles passing through one of these segments are counted as a *hit* if their energy is above this threshold. A bunch crossing is counted as an *event* when there is at least one hit in the detector. Figure 5.3 shows an example detector with stations in the forward region on each side of the IP and illustrates different event counting conditions:

- Event-OR: At least one hit on either side of the IP, i.e. the sum of the three event conditions shown in Figure 5.3.
- Event-ORA(C), At least one hit on the A-side (C-side), i.e. the sum of event conditions 1 & 3 (2 & 3) shown in Figure 5.3.

- Event-XORA(C), At least one hit on the A-side (C-side) and not on the C-side (A-side), i.e. only event condition 1 (2) shown in Figure 5.3.
- Event-AND, A coincidence of hits on both sides of the IP, i.e. only event condition 3 shown in Figure 5.3.

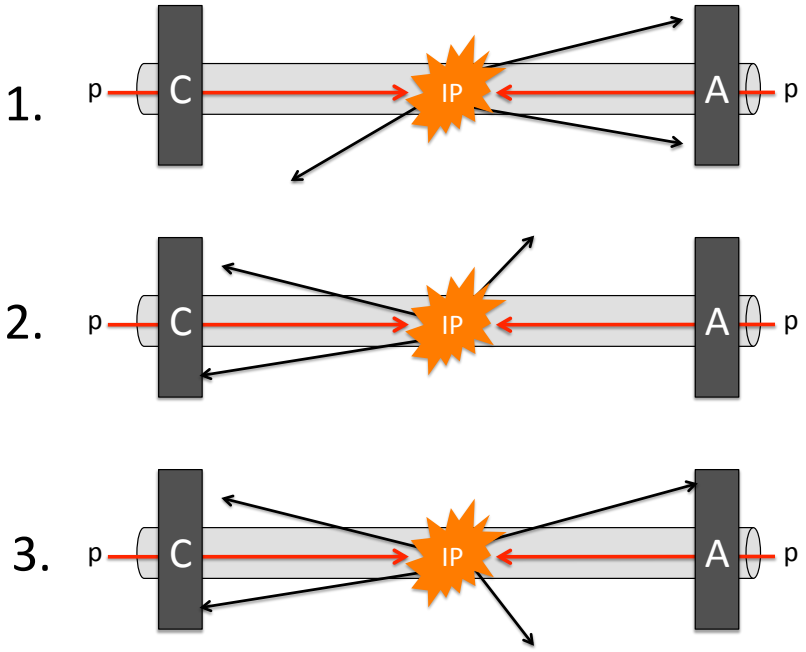

Figure 5.3 Illustration of three different event-counting conditions.

The different conditions have individual advantages and disadvantages. The single sided algorithms (Event-XORA(C), Event-ORA(C)) are useful tools for background studies and to monitor the detector performance, as they enable a direct comparison of measurements on the two sides of the IP. Contrary to real collisions, events from beam-gas and beam-halo are more likely to give hits only on one side of the detector, therefore the coincidence algorithm Event-AND has a strong suppression of such background. On the other hand, a coincidence requirement results in lower statistics than the inclusive Event-OR counting, and the correction for multiple interactions and background is more delicate.

An example of the background suppression is given in Figure 5.4. Where the measured luminosity versus BCID for an LHC fill with many colliding bunches is shown. The upper plot shows μ, as measured with Event-OR , and the lower with Event-AND , both with BCM-H . The bunch-train structure of the colliding BCIDs at a $\mu \approx 10$ is clearly visible. The colliding bunches are followed by background tails due to afterglow, that was mentioned in Chapter 3.3. For Event-OR their background contribution is about 0.5% of the colliding bunch μ, while Event-AND supresses this background

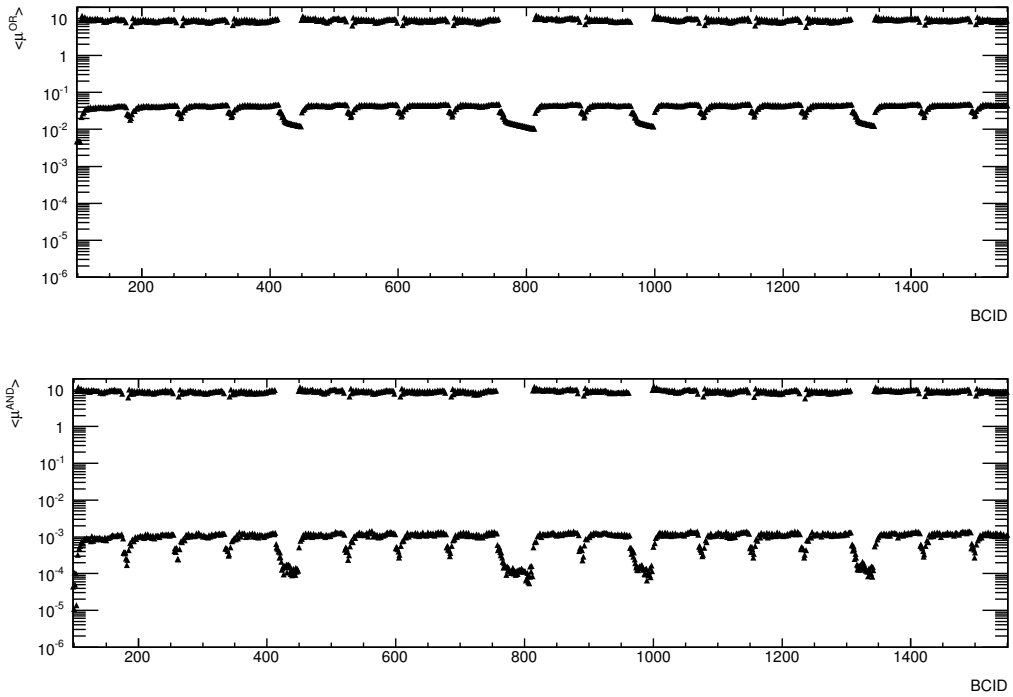

Figure 5.4 This plot shows the μ averaged over several LBs versus BCID as measured with Event-OR (top) and Event-AND (bottom) in LHC fill 2182. The fill had a total of 1332 bunch pairs colliding. The upper values at a $\mu \sim 10$ correspond to trains of colliding bunches. The μ values below the trains correspond to background measured in the non-colliding BCIDs. In order to give a better clarity of the structure only the first 1500 BCIDs are shown.

further by almost two orders of magnitude.
At present the ATLAS luminosity is determined only by Event-counting, as this is the simplest and statistically best understood. However, additional algorithms such as *Particle-* or *Hit-* counting have been developed. But these methods demand a better understanding of the detector-response and are presently not fully under control. [3] One drawback for event counting is that each algorithm is limited to measure only either *true* or *false*, i.e it is just counted if a particular bunch crossing either passes the event condition or not. It is therefore determined that, at a certain value of μ, the probability P_{algo} that the event condition is fulfilled approaches one. Thus every bunch crossing will be counted as an event, which leads to a *saturation* of the algorithm. The tolerable value of μ is detector- and algorithm- dependent: The higher the efficiency, the earlier it saturates. Another problem that can occur is called *migration*. This effect happens if the number of interactions per crossing increases, and signals from particles, that are individually below threshold, combine above threshold and produce a hit. In order to avoid this, the threshold for registering a hit should be chosen low enough, compared to the average single-particle response. The high single-MIP sensitivity of the BCM is therefore an advantage to the LUCID detector, where migration turned out to be a problem.

5.3.2 Determination of the Interaction Rate

The probability functions for the different event counting algorithms will be derived in this section. Knowing these, it is possible to translate the raw events counts of a detector-algorithm in a given time interval into the average *pp* interaction rate per bunch crossing, as seen by this algorithm [66].

p_{00}	$= 1 - \varepsilon_{OR}$	The probability of not detecting an interaction in either A or C
p_{10}	$= \varepsilon_{ORA} - \varepsilon_{AND}$	The probability of detecting an interaction in A, but not in C
p_{01}	$= \varepsilon_{ORC} - \varepsilon_{AND}$	The probability of detecting an interaction in C, but not in A
p_{11}	$= \varepsilon_{AND}$	The probability of detecting an interaction in either A or C

Table 5.1 Exclusive probabilities and their relation to the inclusive efficiencies of the different Event counting algorithms. Note that the efficiencies are for types of events where there is exactly one interaction per bunch crossing.

At the beginning it is useful to define a set of exclusive efficiencies for a single interaction, that are given in Table 5.1, and are labeled with a small p. To derive the

[3] Average particle counting by the FCAL and TILECAL is used to provide a cross-check to the linearity of the event counting algorithms.

probabilities for multi-interaction events, which will be labeled with a capital P, one needs to make two assumptions: First, to assume that the number of *pp* interactions occurring in any bunch crossing obeys a Poisson distribution:

$$\mathrm{P}_{\mu}(n) = \sum_{n=0}^{\infty} \frac{\mu^n \mathrm{e}^{-\mu}}{n!}, \tag{5.20}$$

where $\mathrm{P}_{\mu}(n)$ is the probability to have n interactions in a bunch crossing, when the average number of interactions is μ. The other assumption is that the efficiency ε_1 to detect a single *pp* interaction in a bunch crossing is constant, i.e. not changing when several events occur in the same bunch-crossing.

$$\varepsilon_n = 1 - (1 - \varepsilon_1)^n \tag{5.21}$$

Note that this is only true in the absence of migration.

1. *Event-OR Counting:*

   The probability function for not detecting a bunch crossing that has exactly n interactions is now:

   $$\mathrm{P}_{00}(n) = \mathrm{p}_{00}^n = (1 - \varepsilon_{\mathrm{OR}})^n \tag{5.22}$$

   Assuming n is a Poissonian distributed quantity and using the Taylor series expansion[4], one gets:

   $$\mathrm{P}_{00}(\mu) = \sum_{n=0}^{\infty} (1 - \varepsilon_{\mathrm{OR}})^n \frac{\mu^n e^{-\mu}}{n!} = e^{-\varepsilon_{\mathrm{OR}}\mu} \tag{5.23}$$

   The probability P_{OR} to have an OR-event can be expresses by the number of OR-events N_{OR} divided by the number of bunch crossings N_{BC} in that interval, which is just $1 - \mathrm{P}_{00}$:

   $$\mathrm{P}_{\mathrm{OR}}(\mu) = \frac{N_{\mathrm{OR}}}{N_{\mathrm{BC}}} = 1 - \mathrm{P}_{00} = 1 - e^{-\varepsilon_{\mathrm{OR}}\mu} = 1 - e^{-\mu_{\mathrm{vis}}^{\mathrm{OR}}}, \tag{5.24}$$

   where P_{OR} describes the probability to observe an OR-Event, and P_{00} the probability to observe no event in a given bunch-crossing [67]. Solving this equation for $\mu_{\mathrm{vis}}^{\mathrm{OR}}$ results in:

   $$\mu_{\mathrm{vis}}^{\mathrm{OR}} = -\ln\left(1 - \frac{N_{\mathrm{OR}}}{N_{\mathrm{BC}}}\right) \tag{5.25}$$

[4] The Taylor series expansion is given by $\mathrm{e}^x = \sum_{n=0}^{\infty} \frac{x^n}{n!}$

with Equation 5.18 the luminosity for one bunch can be expressed as:

$$\mathscr{L}_{\mathrm{BC}} = \frac{-\ln\left(1-\frac{N_{\mathrm{OR}}}{N_{\mathrm{BC}}}\right)}{\sigma_{\mathrm{vis}}^{\mathrm{OR}}} \tag{5.26}$$

A Taylor expansion of the logarithm gives:

$$\ln\left(1-\frac{N_{\mathrm{OR}}}{N_{\mathrm{BC}}}\right) = -\sum_{n=1}^{\infty}\frac{\frac{N_{\mathrm{OR}}}{N_{\mathrm{BC}}}}{n} \tag{5.27}$$

the first order in the expansion shows:

$$\mu_{\mathrm{vis}}^{\mathrm{OR}} \approx \frac{N_{\mathrm{OR}}}{N_{\mathrm{BC}}}, \text{ for } \mu_{\mathrm{vis}}^{\mathrm{OR}} \ll 1, \tag{5.28}$$

which is the intuitive statement that the average number of visible interactions per bunch-crossing, and thus also the luminosity, is linearly related to the raw event count n if $\mu_{\mathrm{vis}}^{\mathrm{OR}}$ is much smaller than one.

2. *Single-Sided Event-OR Counting:*
   The derivation is equivalent to the inclusive-OR case, i.e.:

$$\mu_{\mathrm{vis}}^{\mathrm{ORA(C)}} = -\ln\left(1-\frac{N_{\mathrm{ORA(C)}}}{N_{\mathrm{BC}}}\right) \tag{5.29}$$

3. *Coincidence Event Counting:*
   The Event-AND algorithm can be satisfied, either from a single *pp* interaction, or from individual hits on either side coming from different *pp* interactions in the same bunch crossing. Here the relationship between $\mu_{\mathrm{vis}}^{\mathrm{AND}}$ and $\mathrm{N_{AND}}$ is more complicated. Starting with the probability to have a coincidence event in exactly one interaction, by making use that the sum of the exclusive probabilities is exactly one:

$$\mathrm{p}_{11} = 1-(\mathrm{p}_{00}+\mathrm{p}_{10}+\mathrm{p}_{01}) \tag{5.30}$$

For the following it is assumed, that the probability to observe a single interaction is the same, also in multiple-interactions. To calculate the single-sided probabilities for multiple-interactions, one has to take into account the sum of all permutations of k interactions detected in A(C), and n-k interactions not detected in any module. By using the Binomial Identity[5] P_{10} can be written as:

$$\mathrm{P}_{10}(n) = \sum_{k=1}^{n}\mathrm{p}_{10}^{k}\mathrm{p}_{00}^{n-k}\binom{n}{k} = (\mathrm{p}_{10}^{n}+\mathrm{p}_{00}^{n})^{n}-\mathrm{p}_{00}^{n} \tag{5.31}$$

[5] According to the Binomial Identity one has: $\sum_{k=0}^{n}\binom{n}{k}x^{n}y^{n-k} = (x+y)^{n}$

and equivalently P_{01}:

$$P_{01}(n) = \sum_{k=1}^{n} p_{01}^{k} p_{00}^{n-k} \binom{n}{k} = (p_{01}^{n} + p_{00}^{n})^{n} - p_{00}^{n} \tag{5.32}$$

these expressions together with 5.22 can now be used to obtain $P_{11}(n)$:

$$\begin{aligned} P_{11}(n) &= 1 - (P_{00}(n) + P_{10}(n) + P_{01}(n)) \\ &= 1 - (p_{00}^{n} + (p_{10} + p_{00})^{n} - p_{00}^{n} + (p_{01} + p_{00})^{n} - p_{00}^{n}) \end{aligned} \tag{5.33}$$

Taking n as a Poissonian distributed quantity with an average μ one can write:

$$\begin{aligned} P_{11}(\mu) &= 1 - \sum_{n=0}^{\infty} ((p_{10} + p_{00})^{n} + (p_{01} + p_{00})^{n} - p_{00}^{n}) \frac{e^{-\mu}\mu^{n}}{n!} \\ &= e^{-\mu(1-p_{10}-p_{00})} + e^{-\mu(1-p_{01}-p_{00})} - e^{-\mu(1-p_{00})} \end{aligned} \tag{5.34}$$

The probability of observing a coincidence using the efficiencies of Table 5.1 becomes:

$$P_{11}(\mu) = 1 - e^{-\mu\varepsilon_{ORA}} - e^{-\mu\varepsilon_{ORC}} + e^{-\mu(\varepsilon_{ORA}+\varepsilon_{ORC}-\varepsilon_{AND})} \tag{5.35}$$

with $\varepsilon_{OR} = \varepsilon_{ORA} + \varepsilon_{ORC} - \varepsilon_{AND}$ and the assumption that $\varepsilon_{A} \approx \varepsilon_{C}$ the probability for a coincidence count is given by:

$$P_{AND}(\mu_{vis}^{AND}) = \frac{N_{AND}}{N_{BC}} = 1 - 2e^{-(1+\sigma_{vis}^{OR}/\sigma_{vis}^{AND})\mu_{vis}^{AND}/2} + e^{-(\sigma_{vis}^{OR}/\sigma_{vis}^{AND})\mu_{vis}^{AND}} \tag{5.36}$$

The μ-dependency on ε_{OR} and ε_{AND} is different to the Event-OR case, where ε_{OR} factors out of Equation 5.25. Equation 5.36 cannot be inverted analytically and must be solved numerically.

With the above derived equations one can calculate the visible number of interactions μ_{vis}^{algo} per bunch crossing from the measured event probabilities $P_{algo} = \frac{N_{algo}}{N_{BC}}$ for a given algorithm.

Figure 5.5 illustrates the distribution of the event-probabilities versus μ assuming typical efficiencies for the BCM: $\varepsilon^{OR} = 6 \cdot 10^{-2}$ and $\varepsilon^{AND} = 1.9 \cdot 10^{-3}$. One can see that the Event-OR algorithm has high statistics and is linear at low μ, but saturates earlier than Event-AND. With these comparatively low efficiencies of the BCM the graph illustrates that both algorithms are usable up to very high values of μ.

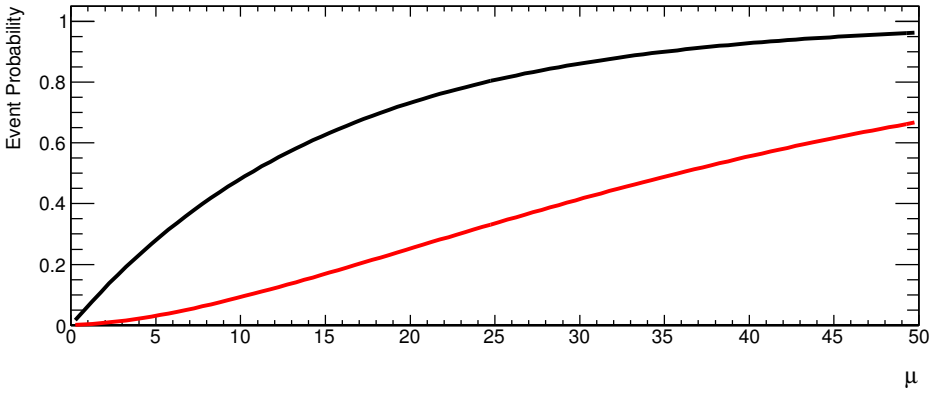

Figure 5.5 Event probability versus the average number of interactions per bunch crossing μ for Event-OR (black) and Event-AND (red).

5.3.3 Extraction of the Calibration Constant σ_{vis}

It has been derived previously in this Chapter, that it is possible to determine the luminosity by performing two subsequent scans in the horizontal and vertical plane of the beam. Setting the expressions for luminosity as given in 5.12 and 5.19 equal, one obtains:

$$\sigma_{\text{vis}} = \frac{2\pi\mu_{\text{vis}}\Sigma_x\Sigma_y}{n_1 n_2} = 2\pi\mu_{\text{vis,sp}}\Sigma_x\Sigma_y \tag{5.37}$$

As the intensities of both beams decay with time it is useful to define *specific values*. These values are corrected for the currents and labeled with the index "*sp*", i.e. $\mu_{\text{vis,sp}} = \mu_{\text{vis}}/(n_1 n_2)$. Equation 5.37 can be used to calculate σ_{vis} from measured scan data (μ_{vis}, Σ_x and Σ_y) and a simultaneous determination of the bunch intensities n_1 and n_2. Since there are two independent measurements for μ from horizontal and vertical scans and both having the same statistical significance, Equation 5.37 uses the arithmetic average of the two. The final formula for σ_{vis} becomes:

$$\sigma_{\text{vis}} = \pi\left(\mu^x_{\text{vis,sp}} + \mu^y_{\text{vis,sp}}\right)\Sigma_x\Sigma_y, \tag{5.38}$$

The specific luminosity per bunch is obtained from Equation 5.12 by dividing with the intensity product $n_1 n_2$:

$$\mathscr{L}_{\text{sp}} = \frac{f_r}{2\pi\Sigma_x\Sigma_y} \tag{5.39}$$

It can be seen that, unlike σ_{vis}, the value of $\mathscr{L}_{\text{sp}}$ does not depend on any quantities that would involve properties of the detector or algorithm. It is therefore a useful quantity to compare between different algorithms and detectors.

5.4 van der Meer Scans in ATLAS

A *vdM* scan is ideally done in a dedicated fill with special settings that are very different to normal physics operation. Special parameter settings for the filling scheme, bunch intensities and beam optics need to be chosen carefully to optimize the result [68]. The following summarizes the general strategy for the 2010/2011 *vdM* scans. To reduce backgrounds from satellite currents and afterglow the scans are performed with a limited number of isolated bunches in the machine. In addition, this has the advantage of gathering more statistics per-BCID with the capabilities of the DAQ systems.
In principle a low number of colliding bunches (14 for ATLAS and CMS in the latest scan) does not require any crossing angle at the IP, since the chance of parasitic collisions is greatly reduced. But to reduce the time spent for specific machine development it is in general chosen to use optics settings from physics fills that include a non zero crossing angle. To reduce beam-beam effects (more on this in Section 5.5.2) it is preferred to maximally decouple the different Interaction Points of the LHC. Bunches that only collide at IP1 and IP5[6] are also referred to as *private bunches*. The average number of interactions per bunch crossing μ depends on the beam parameters ε and β^*, and the bunch intensities. μ should not be chosen too high, to keep the pile-up under control, but still at a value that minimizes the time necessary to accumulate enough statistics (especially in the tails of the rate measurements, where the separation is large). For ATLAS and CMS typically a value between 1-2 is chosen.
Up to now, four sets of *vdM* scans have been performed in ATLAS at an energy of 3.5 TeV per beam. Additionally there were two scans within a heavy-ion fill and one scan at a lower energy of 1.38 TeV per beam. The first two were performed in early LHC-operation in April and May 2010 with one colliding bunch. The main characteristics of these scans, that are labeled as I-III, are summarized in Appendix B. At this early stage not all the online luminosity infrastructure was in place and the scans were performed with comparatively low intensity. For this reason the BCM event counting algorithms had a very low rate and only preliminary calibrations for Event-OR could be performed. For the May 2010 scan the total luminosity could be determined to a level of 11%. The main sub-detectors taking part in this analysis were LUCID, MBTS and offline algorithms for the Inner Detector and Liquid Argon End-caps. Details on the analysis can be found in [1]. The following set of scans (labeled as IV-V) in October 2010, were performed with a much higher peak luminosity and multiple colliding bunches such that the BCM detector started to play a key role. The BCM analysis of the October scan will be subject of the following Chapter 6. Due to a number of hardware changes in the winter-shutdown of 2011, the luminosity calibrations needed to

[6] due to their location at the LHC ring ATLAS (IP1) and CMS (IP5) always share the same colliding bunches.

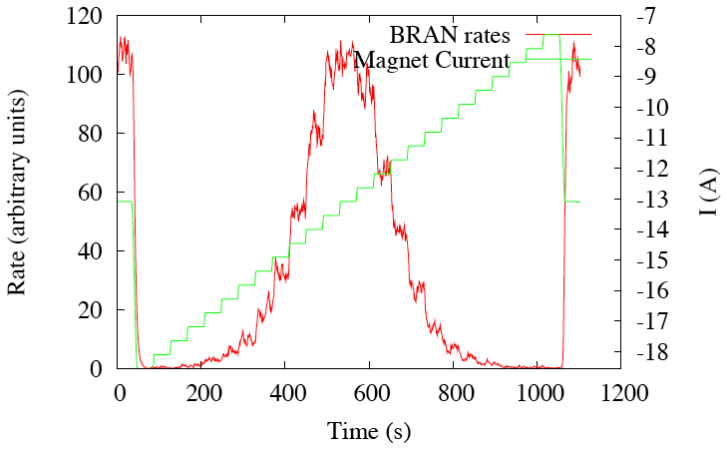

Figure 5.6 The current drawn in the dipole magnets that separate the beams at the IP, versus the counting rate measured by the BRAN detectors. The beams are separated from head-on collisions to the maximum separation and then moved stepwise across one another [6].

be re-done. Therefore a new set of scans (labeled as VII-VIII) was performed in May 2011, which will be discussed in Chapter 7.

5.4.1 Scan Procedure

The general procedure in each scan is to first center the beams in both planes with respect to each other with so-called *mini scans* in order to ensure that the beams are colliding head-on. This is done by varying the IP position of both beams by $\pm 1\sigma_b$ using the orbit corrector magnets, where σ_b is the nominal transverse size of either beam at the IP and the separation is defined by the difference of the beam 1 position to the position of beam 2. The relative positions of the two beams are then adjusted in each plane according to the maximum rate measured by one of the luminosity sub-detectors in order to find the optimum transverse overlap.

After the mini scans a full luminosity calibration scan is performed. First in horizontal direction, keeping both beams centered in the vertical plane. Both beams are displaced by up to $\pm 3\sigma_b$ symmetrically in opposite directions, spanning a total relative displacement of $\pm 6\sigma_b$. First the beams are moved to the maximum separation in the negative direction, i.e. to $-6\sigma_b$. Then they are moved back to zero and on to the maximum positive separation, to $+6\sigma_b$. In total 25 steps were performed, where the beams were left quiescent for 30 s. This time is supposed to be sufficient for the different detector-algorithms to accumulate enough statistics at each scan-point, in order to subsequently perform a proper fit to the resulting scan-curve. The horizontal scan is followed by the same procedure in the vertical direction, now keeping the beams centered in the horizontal plane. To test the reproducibility of the results the first set of

$x-$ and $y-$ scans is followed by a second one. An example plot of the current drawn in the steering dipole magnet, that separates the two beams at the IP, versus the measured rate is shown in Figure 5.6.

5.4.2 Scan Step Synchronization

Within a *vdM* scan the luminosity varies with the steps of beam displacement, that is introduced by steering magnets at the IP. This variation does not match the LB concept of a normal ATLAS run, where the LB length is generally fixed to one minute. To properly synchronize the rate measurement with the magnet setting, i.e. the scan steps, and to make sure that the data acquisition is performed only while the beams are not moving, a special scan-controller has been put in place. This *Lumi Scan Controller* receives the information about the beam movement from the LHC and issues so called *pseudo-LB* (PLB) boundaries. Upon a command, that is sent by the scan controller, the luminosity sub-detectors and the OLC are able to switch from ATLAS LBs to PLBs as soon as the *vdM* scan starts (and reverse, when the scan is over). The relevant data for each scan session is therefore stored in a number of PLBs corresponding to the movement of the beams. Each scan consists of a number of *acquisition* PLBs, where the beams were stable and proper data was recorded, and *movement* PLBs during which the beams were moving from one point to the next, which are discarded in the analysis. For several reasons ATLAS cannot synchronize to the PLB boundaries and continues to run in parallel with normal LB settings. This data becomes therefore invalid during the time of a *vdM* scan.

5.4.3 Recording and Analyzing the Data

The data-flow of the online luminosity has been explained in Chapter 4.6. The rates measured by the different luminosity monitors are stored together with the value of the scan-step as specified by the LHC control system (*nominal separation*), beam currents and the other relevant accelerator parameters from the online-data stream. The rates and currents, accumulated over the duration of the PLB, are stored as a per-bunch vector of 3564 entries. For various reasons one needs to assume different convolved beam sizes and peak-μ values for each colliding bunch. Therefore the *vdM* analysis must be performed on a per-bunch level.
For each scan point and BCID the event counting rates of the different algorithms are normalized to the number of bunch-crossings in the time interval. The resulting raw event rate per bunch crossing is then first corrected for pile-up, as explained in Section 5.3.2, to calculate μ_{vis} and then divided by the bunch current product $n_1 n_2$ to calculate $\mu_{\text{vis,sp}}$. The convolved beam sizes $\Sigma_{x,y}$ are then extracted by a fit to $\mu_{\text{vis,sp}}$ versus the

nominal separation.

5.4.4 Length Scale Calibration

The beams at the interaction point are displaced by modifying the beam orbit with a *closed orbit bump* that is generated by four bump amplitudes from the dipole steering magnets close to the IP [6]. The *nominal beam separation* is the desired value of beam displacement that is input into the LHC control system, e.g. in μm. The scale of the nominal displacement are computed from the optics settings used at the time of the *vdM* scan.

Determining the total luminosity from beam parameters with Equation 5.12 relies directly on the accuracy of the transverse convolved beam sizes $\Sigma_{x,y}$. An error on the relative scale of the beam position would directly translate in an uncertainty on the fitted beam size and therefore also on σ_{vis} and the luminosity. To make sure that the nominal separation yield the predicted beam-separation an independent measurement of the displacement at the IP is needed. This can be done by calibrating the length-scale in dedicated length-scale calibration scans, where the displacement at the IP is measured precisely with primary vertices, reconstructed in the ATLAS Inner Detector. These scans are done close in time to each *vdM* scan set with the same collision optics configurations.

Four different scans are performed to calibrate four bump amplitudes, one for each beam, in both horizontal and vertical planes. In each of these scans both colliding beams are moved in the same direction from the nominal beam position in a number of steps and a given step size. At each scan point the beam being calibrated is kept stationary, while the other beam performs a mini scan. By fitting the measured rate of each mini scan as measured by the active luminosity monitors one can determine the luminous centroid position of maximum beam overlap at each scan point. The actual length scale calibration is then performed by a linear fit to the luminous centroid positions relative to the nominal bump amplitude for each of the two beams in the two transverse planes. Since the *vdM* scans are performed by separating the two beams symmetrically in opposite directions, the relevant scale factor in the determination of $\Sigma_{x,y}$ is the average of the scale factors for beam 1 and beam 2 in each plane. A schematic illustration of the different steps for one scan is shown in Figure 5.7, more details can be found in [67].

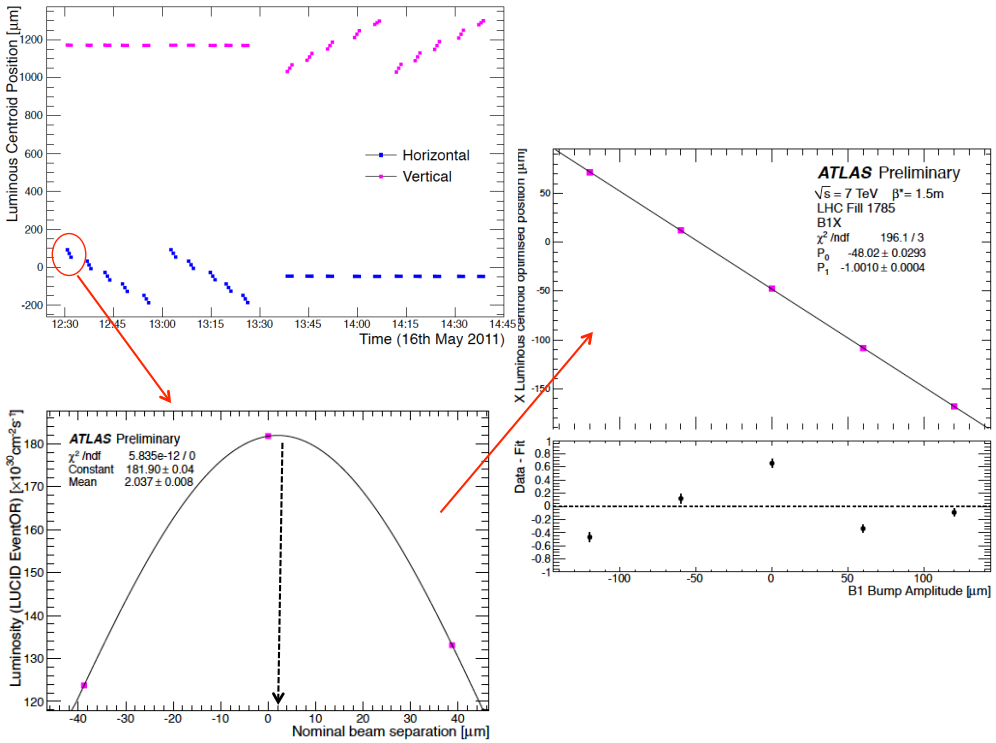

Figure 5.7 Schematic illustration of the analysis steps of a length-scale calibration scan for one beam and one plane [67]: The plot on the top left shows the horizontal and vertical luminous centroid position as determined by vertex reconstruction. Clearly visible are the mini-scans in one transverse plane, while the other beam is kept stationary. The rate measured with a luminosity sub-detector of each mini-scan is plotted against the nominal separation and is fitted with a Gaussian (plot on the lower left). From this the luminous centroid position at optimal beam overlap can be determined. Five of these values, one from each mini-scan, are then plotted against the bump amplitude from which the calibration constant for the corresponding beam and plane can be determined.

5.5 Calibration Uncertainties

A number of systematic uncertainties for the determination of σ_{vis} and the luminosity have to be taken into account. Some of them are detector specific, others are common to all luminosity detectors involved in the *vdM* analysis. The uncertainties will be qualitatively explained in this Section and quantitatively discussed in the analysis Chapters 6 and 7. Note that some of the systematics were not accounted for at the given time of the October analysis (Chapter 6) and are thus only examined for the May scans (Chapter 7).

5.5.1 BCM DAQ Issues

The *vdM* analysis in this thesis is based on time averages over acquisition PLBs, during which the beams were kept stable. These PLB-averages were calculated "on-detector", i.e. in the BCM. The BCM registers are read every 9000 LHC orbits (1.25 Hz) and the PLB integrals are calculated from all samples within the PLB boundaries. A feature of the Data Acquisition software of the BCM was that if such a 9000 turn sample falls across a PLB-boundary the whole sum in the preceding PLB is interpolated with respect to the boundary. Since in a *vdM* scan an acquisition PLB is always followed by a PLB where the beams are moving, this interpolation induces a problem. The interpolation over the entire PLB causes that a small random fraction of the data in which magnets were not stable gets accounted into the integral over the acquisition PLB. This is clearly reflected in the data as the first point of each scan being much higher than the next. Due to the interpolation this first point gets a contribution from the movement PLB, during which beams were moving from head-on to maximum displacement (c.f. Figure 5.6). These points are far in the tail and can therefore be safely excluded from the fits. For this reason all scan-curves, in the following Chapters consist of only 24 acquisition PLBs, instead of 25. A similar consequence of this interpolation was that at the end of an acquisition PLB the interpolation could extend into the period when beams were already moving. The magnet movement started immediately when the acquisition PLB period had ended and in 5 s the new beam position was reached. The LHC provided a countdown towards this, but in 2010 it was not yet implemented in the scan controller. If the last 9000 turn sample extended into the period of magnet movement, the varying luminosity got accounted into the acquisition-PLB. The effect of this would be opposite to the one described before, i.e. it would bias points up on the rising edge and down on the falling edge. However, the change in luminosity is much lower than for the first scan-point and the pull distributions of fits to the data show no signs of such a bias. Therefore this effect is assumed to be negligible. Note that from beginning of 2012 this problem is fully fixed by discarding a 9000 turn sample if it

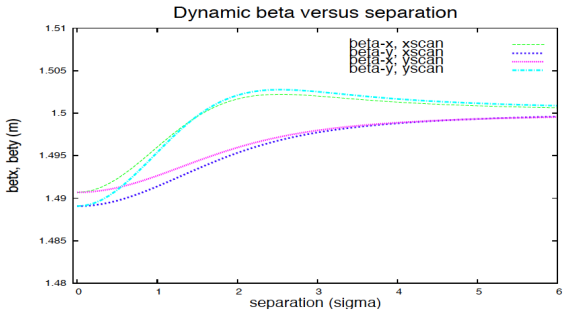

Figure 5.8 Change of β^* at IP1 versus nominal separation. with collisions at IP1 [11].

falls across a PLB boundary.

5.5.2 Beam-Beam effects

Beam-beam interactions have been described in Chapter 2.3.1. The impact of these effects within a *vdM* scan have recently been studied and are presented in [11]. It was explained that the beam-beam force is linear for small amplitudes (head-on collisions) and becomes non-linear for larger amplitudes. Within a *vdM* scan one must therefore expect the beam-beam force to change with the separation which can slightly distort the shape of the scan-curve and potentially bias the measurement of $\Sigma_{x,y}$ [2]. Every collision has an impact on the β function, therefore the change in β^* for a given BCID at IP1 depends on where else in the LHC this bunch is colliding.

Figure 5.8 shows the change in $\beta^*_{x,y}$ during horizontal and vertical scan, respectively, assuming collisions in IP1 only. The effect of changing beam-beam force is clearly visible, in particular when the focusing strength changes the sign at $\approx 1.6\sigma_b$. From Equation 2.13 one knows that the luminosity is proportional to $(\beta^*_x\beta^*_y)^{-1}$, thus one can calculate the change in luminosity due to dynamic-β versus the nominal separation. The effect on the luminosity calibration can be evaluated by comparing the σ_{vis} of two Gaussians with that of the same Gaussians multiplied with the change in luminosity per separation step due to dynamic-β [69].

5.5.3 Bunch Charge Product

Besides the transverse convolved beam sizes the main ingredient for determination of the total luminosity from beam parameters as given by Equation 5.12 is the determination of the bunch charge product $n_1 n_2$. This product has to be measured separately for each BCID to account for a per-bunch variation in the intensity and also because in general not all circulating bunches collide at the ATLAS IP. The determination of the systematic uncertainties on the bunch charge product is done by the BCNWG and has

been described in Chapter 3.4.4.

5.5.4 Beam Centering

If the beams are offset in the transverse direction orthogonal to the scanning plane at the start of a *vdM* scan, the overall rate for all scan-points is reduced. The assumption that the luminosity observed at the peak is equal to the maximum head-on luminosity is therefore not correct. The systematic uncertainty associated with imperfect beam centering can be estimated by considering the maximum deviation of the peak position from the nominal null separation. Equation 2.16 can be used to estimate the error on $\mu_{\text{vis,sp}}^{\text{MAX}}$ which translates then directly to the error on σ_{vis}.

5.5.5 Transverse Emittance Growth and Other Non-Reproducibility

The *vdM* scan formalism assumes that the transverse emittances, and therefore luminosity and the convolved beam sizes $\Sigma_{x,y}$, are constant during the horizontal- and vertical scans. Even if, as in the case of the LHC, beam conditions at low intensity are relatively stable and the emittance is not foreseen to grow significantly over the duration of a scan [6], potential effects on the *vdM* results need to be investigated.
A first bias could result from an increase of the emittance within a single $x-$ or $y-$ scan. This would lead to a slight distortion of the scan curve, meaning the rise of beam sizes contributes to an asymmetric shape of the scan curve. The amount of emittance growth within a scan can be estimated from both, the evolution of the beam spot size, and measurements from wire scanners versus time in the fill. The effects on σ_{vis} was studied by a toy Monte Carlo, where the scan-curves are distorted by the amount of emittance growth. The effect was found to be negligible and is covered by the fit model uncertainty [70].
A second problem could arise because horizontal and vertical scans are performed separated in time, and σ_{vis} is calculated using results from both scans. Emittance growth between horizontal- and vertical scans would show a slight increase in the measured $\Sigma_{x,y}$ and a simultaneous decrease in the measured peak rate. For the calculation of σ_{vis} using Equation 5.38 this effect should therefore cancel to a certain degree. This effect including further uncertainties due to non-reproducibilities can be estimated by comparing the bunch-average σ_{vis} values between the two consecutive scans. Resulting deviations are accounted for as systematic uncertainties.

5.5.6 σ_{vis} Consistency

The calibrated σ_{vis} values may differ between detectors and algorithms, but should be independent of BCID and scan. Therefore two consistency checks need to be made.

First, to look for any variation per BCID and scan in the σ_{vis} results, that is not of statistical nature. Second, how well do the bunch-averaged results agree between the two consecutive scans.

5.5.7 Length Scale Calibration

The length scale of each scan step enters directly into the extraction of $\Sigma_{x,y}$, as explained in the previous section 5.4.4. An overall correction factor on the nominal separation and an estimate on the uncertainty can be extracted from dedicated length scale calibration scans. However, the accuracy of these scans relies directly on the absolute length scale of the ATLAS Inner Detector, i.e. that the length scale of the ATLAS tracking system being correct in measuring displacements of vertex positions. An uncertainty on this length scale has been estimated via Monte Carlo studies using several different miss-aligned ID geometries [67]. Samples are produced with displaced interaction points to simulate the transverse beam displacements seen in a *vdM* scan. The variations between the true and reconstructed vertex positions in these samples can give an estimate on the uncertainty on the determination of σ_{vis} due to the absolute ATLAS ID length scale [67].

5.5.8 Beam Position Jitter

Besides correcting the absolute scale of the nominal separation, one needs to estimate effects of random deviations of the beam positions from their nominal setting. This so called "jitter", that is probably due to small instabilities in the dipole magnets, could cause the points of the *vdM* scan curve to be slightly misplaced. These deviations can also be estimated within the length scale calibration scans. The RMS of the variations in the peak positions measured by the mini scans can give an estimate of the amount of the jitter. The effect on σ_{vis} can be evaluated by randomly displacing the nominal position of each measurement point in a simulated scan by this value. The RMS of the resulting variations in the fitted visible cross-section can then be taken as a systematic uncertainty [70].

5.5.9 Fit Model

In general the *vdM* scan-curves, i.e. the rate measurement versus nominal separation, are fitted with either a Gaussian or a Double-Gaussian fit function plus a constant term. This term should account for any non-Gaussian tails or background that is independent of the beam separation. However, there is no physics argument that the convolved beam sizes prefer any particular fit function. Furthermore, if a background correction is applied before the fit to the data one needs to carefully evaluate if the rate fitted by

the constant term is solely background or also contains "real" luminosity. Therefore different fit models are applied to the data:

- (double-) Gauss + $p0$(B): This fit model uses an analytical Gaussian fit plus a 0^{th} order coefficient $p0$. The $p0$ term is assumed to be background and is therefore not taken into account. Consequently this model should be used for non-background subtracted data. The convolved beam size Σ and the $\mu_{\text{vis,sp}}^{\text{MAX}}$ in this case can be directly taken from the fit.

- (double-) Gauss + $p0(\mathscr{L})$: This model uses the same analytical function as the one above, but instead the $p0$ term is assumed to contain luminosity. Therefore this fit model should be used for background-corrected data. The $\Sigma_{x,y}$ cannot be taken directly from the fit, but must be calculated by using Equation 5.11, i.e. by:

$$\Sigma_k = \frac{1}{\sqrt{2\pi}} \frac{\int_{-6\sigma_b}^{6\sigma_b} \left[\mu_{\text{vis,sp}}(k) + p0\right] \mathrm{d}k}{\mu_{\text{vis,sp}}(k_0) + p0} \tag{5.40}$$

  Hence the integral of the curve including the $p0$ term over the scan-range, divided by $\mu_{\text{vis,sp}}^{\text{MAX}}$, which is the maximum height of the fit, plus the $p0$ term.

- Cubic Spline: The third method is to refit the data with a cubic spline, i.e. a piecewise 3^{rd} order polynomial function. In this case the $\Sigma_{x,y}$ are also calculated by the integration method mentioned above, and the $\mu_{\text{vis,sp}}^{\text{MAX}}$ is just the highest point of the spline-fit.

The maximum deviation in the results of σ_{vis} can be taken as a measure of the systematic uncertainty due to the fit model.

5.5.10 Transverse Correlation

A correlation in the beam profile between horizontal and vertical planes can have an impact on the convolved beam sizes and hence on the luminosity. Such distortions could be caused e.g. by beam-beam effects.

One method to investigate $x-y$ correlations is to perform an offset-scan right after the actual *vdM* scan. These scans are similar to a normal *vdM* scan, just that the beams are offset on purpose in the non-scanning plane. It can then be tested if the beam shapes measured in the *vdM* scan can be reproduced (of course the rates are downscaled by a factor) or if the offset leads to a modulation of the shape. Potential correlations can also be estimated by measuring the transverse displacements of the luminous region during the scan, i.e. by fitting the transverse distribution of event vertices. Linear x-y correlations in both beams would have no effect on round beams. If Σ_x and Σ_y are sufficiently different, however the luminosity distribution in the transverse planes would

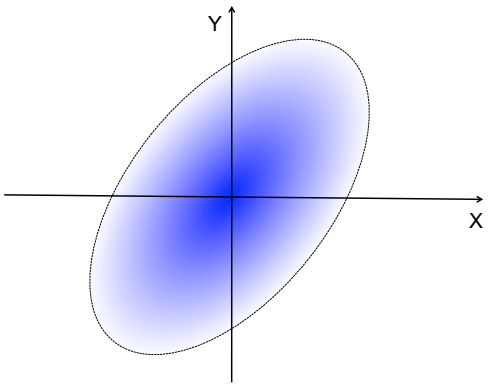

Figure 5.9 Sketch of a tilted ellipsoid convolved beam profile.

transform from an upright ellipse into a tilted ellipse, as demonstrated in Figure 5.9. If the transverse profiles of the luminous region can be described by a single Gaussian any linear correlation between horizontal and vertical plane would modify the specific luminosity by a factor $(\sqrt{1-\rho^2})^{-1}$, where ρ is the correlation coefficient between the two transverse axes which can be measured by a fit to this ellipse. If the luminous region is described by a double Gaussian beam density profile the situation is more delicate. Here non linear correlation terms can appear. For example they could arise if the luminous region consists of two distinct sub-populations, one that reflects *pp* collisions in the Gaussian core, and one corresponding to collisions in the tails. In this case the factorization that was assumed for a single Gaussian in Equation 5.9 is not valid anymore. A possible impact of this effect can be studied by employing a generalized double-Gaussian fit simultaneously to the *x*- and *y*- scan data. A detailed discussion of these effects can be found in [71] and [72].

5.5.11 μ Dependence

The *vdM* scans are taken over a certain μ range. Any uncertainties on the pile-up correction can directly affect the evaluation of σ_{vis}. An estimate on the uncertainty can be made by comparing the relative deviation in the average value of μ from different algorithms and detectors, to that of a reference algorithm within the *vdM* scan, where σ_{vis} was calibrated.

5.5.12 Long Term Stability and Consistency

The *vdM* scans are taken under special conditions that are very different to the settings of physics data taking. It is therefore necessary to evaluate the stability and linearity of the calibrations also during normal running. Furthermore several effects can have an impact on the long-term stability of a given detector and also varying LHC beam con-

ditions, e.g. the detector responses, can depend in particular on the number of bunches in a fill. The agreement between the luminosity observed by the various algorithms can provide a test of the stability of the calibration over long time periods and under differing beam conditions, including higher μ values and shorter bunch spacing. On the basis of the agreement of their μ values a systematic uncertainty can be estimated.

Chapter 6

October 2010 *vdM* scan

	vdM Scan IV–V (1 October, 2010)
LHC Fill Number	1386
Scan Directions	2 Sets of x- and y- Scans
Total Scan Steps per Plane	25
Scan Range	$(\pm 6\sigma_b)$
Scan Duration per Step	20 s
Number of Colliding Bunches in ATLAS [n_b]	6
Total Number of Bunches per Beam	19
Number of Protons per Bunch [$n_{1,2}$]	$\sim 0.9 \times 10^{11}$
β-Function at IP [$\beta^\star$] (m)	~ 3.5
Transverse Single Beam Size σ_b (μm)	~ 60
Full Crossing Angle [θ_c] (μrad)	200
Typical Luminosity/Bunch (Hz/μb)	0.22
Typical μ	1.3

Table 6.1 Summary of the main characteristics of the October *vdM* scan performed at the ATLAS interaction point in 2010. The values of luminosity/bunch and μ are given for zero beam separation. The transverse single beam size is given assuming nominal emittances of $\varepsilon_N = 3.75\mu$m

This Chapter describes the calibration of the Event-OR and Event-AND algorithms of BCM-H [1], with two *vdM* scans, performed on October 1st, 2010. The main characteristics of these scans, labeled as IV–V, are summarized in Table 6.1. If not otherwise stated all results presented are extracted from the online BCM data stored to COOL.

[1] By the time of this scan neither the data from BCM-V , nor data from Event-XORC, were stored to COOL

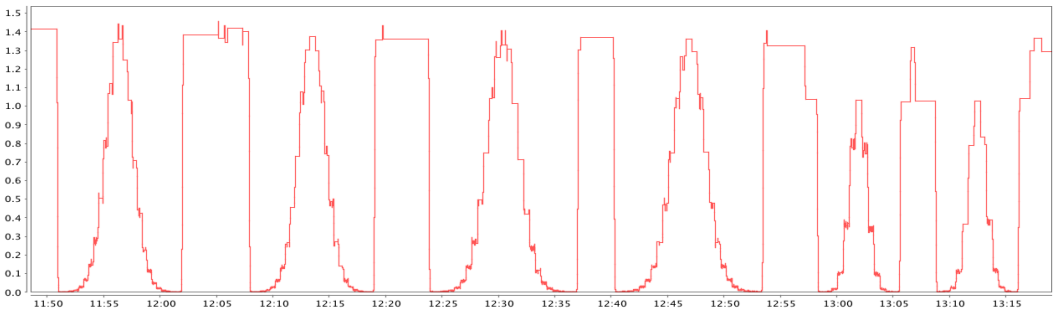

Figure 6.1 Screen-shot of the instantaneous luminosity versus time, as reported by BCM-H Event-OR online during the October *vdM* scan in the ATLAS control-room. The third set of scans was done with an offset in the non-scanning plane, therefore the peak rate is reduced.

The October scans, that are labeled as IV–V, took place in the LHC fill with number 1386. The fill had 19 filled bunches per beam of which 6 well separated bunches (BCIDs 1, 501, 862, 1451, 1651, 2301) were colliding in IP1 (and IP5). The injected bunch pattern is shown in Figure 6.3 in the form of Event-OR μ, averaged over the time where the beams were colliding head-on. The beams were brought into collision with an energy of 3.5 TeV, a full-crossing angle of 200 μrad and a β^* of 3.5 m. The *vdM* scan spans a range of $0 < \mu < 1.3$. The scan sequence in form of online luminosity reported by BCM-H Event-OR versus time is shown in Figure 6.1. The first horizontal scan (IV_x) started around 13:51, followed by a scan in vertical direction (IV_y). Subsequently another set of scans in x- and y- was performed, labeled as V_x and V_y, in order to test the reproducibility of the scan IV results. These were followed by a third scan set, that was performed with a $1\sigma_b$ offset in the non-scanning plane, in order to investigate any possible x-y coupling.

In a given plane the beams were displaced to the maximum nominal separation in negative direction of -355.9μm. The nominal separation was changed in 25 steps of 29.66 μm such that the beams were brought back into head-on collision and then again displaced from each other in the other direction to a maximum positive separation of 355.9μm. In total this spans the range of $\pm 6\sigma_{\mathrm{beam}}$. Figure 6.2 shows the nominal beam separation versus time for the scan IV_y. At each separation point when the beams were kept stable, data are recorded for all luminous BCIDs for an interval of $\approx$ 20 seconds.

6.1 Fitting the Data

For each algorithm 24 scan-curves are to be analyzed, representing the six colliding bunches each with two sets of horizontal- and vertical scans. Figure 6.4 shows the raw Event-OR and Event-AND rates per bunch crossing versus nominal separation for

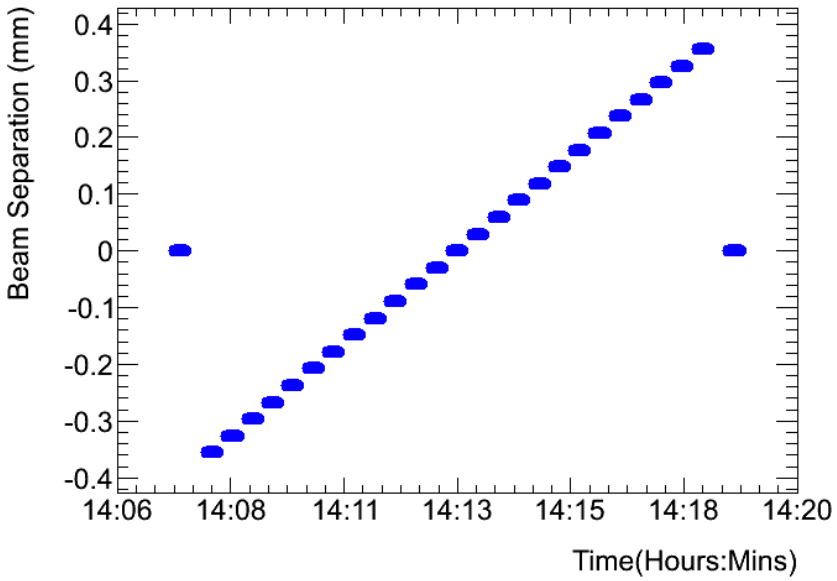

Figure 6.2 The nominal separation that is specified by the LHC control system versus time (for scan IV_y).

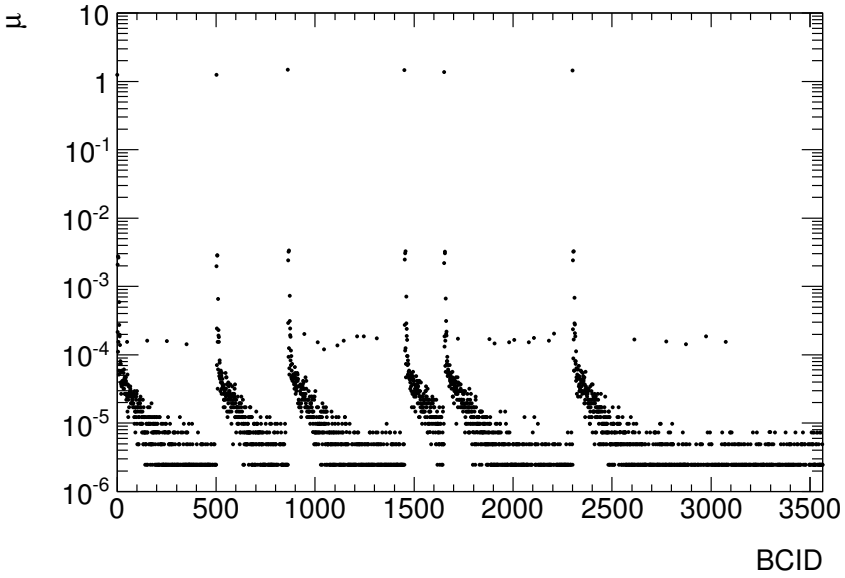

Figure 6.3 The number of interactions per bunch crossing μ as measured per BCID with BCM-H Event-OR . This plot is averaged over several LBs between the scans, i.e. where the beams were centered. The six peaks of colliding bunches can be seen. The points forming a horizontal line at about 2×10^{-4} are due to the 26 unpaired bunches. The tails after each colliding bunch are afterglow.

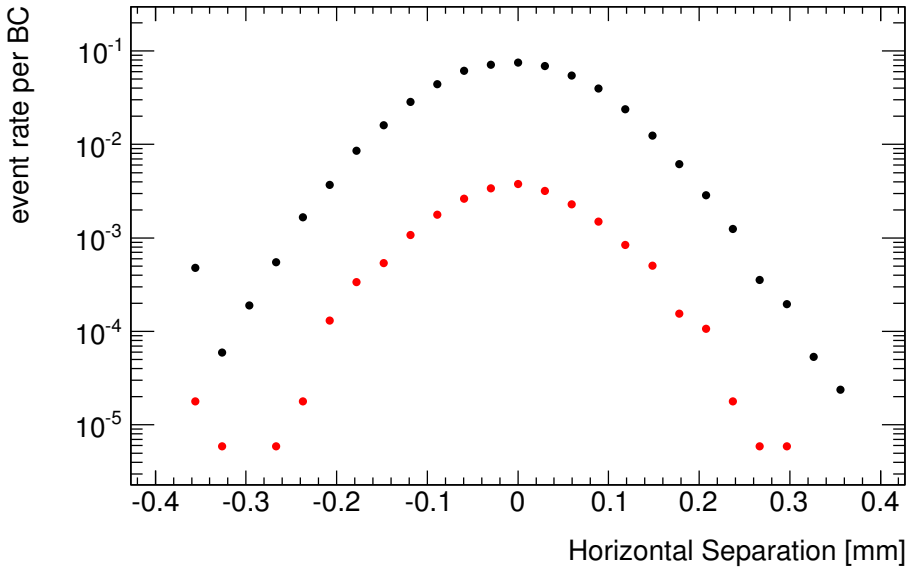

Figure 6.4 Raw Event-OR (black) and Event-AND (red) rates of BCM-H versus nominal separation for BCID 1 scan IV$_x$. The first scan-point for both algorithms is significantly higher, due to the interpolation problem in the BCM readout. This scan-point will be discarded in the following.

an example BCID, plotted on a logarithmic scale. It is clearly visible that the first scan-point at -0.36 mm separation is much higher for both algorithms, which can be assigned to the interpolation problem explained in 5.5.1. This plot also illustrates the significant difference in the efficiency of the two algorithms. The Event-AND rate is about 19 times smaller than that of Event-OR. These low statistics of the event-counts are problematic, in particular in the tails of the scans. With N being the number of observed events, the general assumption for the statistical uncertainties on the event-rates per bunch-crossing R to be $\Delta R = \sqrt{N}$ becomes invalid for very small N. If the number of events drops to zero for a given scan-point, as it is the case for some Event-AND curves, the error on it would become zero as well, and a χ^2 fit would be forced to pass exactly through this point.
For this reason it was decided to follow the prescription for low statistics Poisson distributed data: $\Delta R = 0.5 + \sqrt{N + 0.25}$, as suggested by the CDF experiment [73]. This allows to do proper binned χ^2 fits to all scan-curves, even if N drops to zero.

Figure 6.5 shows the bunch intensity product of the two beams as measured by the FBCT for each colliding BCID versus time. The arrows indicate when the four *vdM* scans took place. The plot demonstrates that the intensities drop at slightly different rate for the individual bunches. In general per-bunch variations of the level of 10-20% are observed. Such per-bunch intensity variations are typical to physics operation and mainly caused by the pre-injectors of the LHC [75]. This current decay is implicitly taken into account at each acquisition point by fitting the current corrected

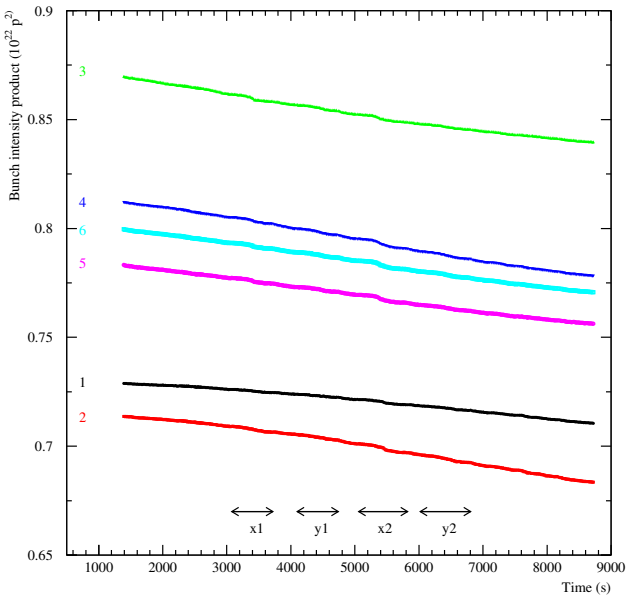

Figure 6.5 Bunch intensity product of the two beams for the colliding BCIDs versus time [74]. The time of the scans is indicated by the arrows. One sees that the intensity decay is different for each BCID, which shows that the intensity correction needs to be performed at a per-bunch level.

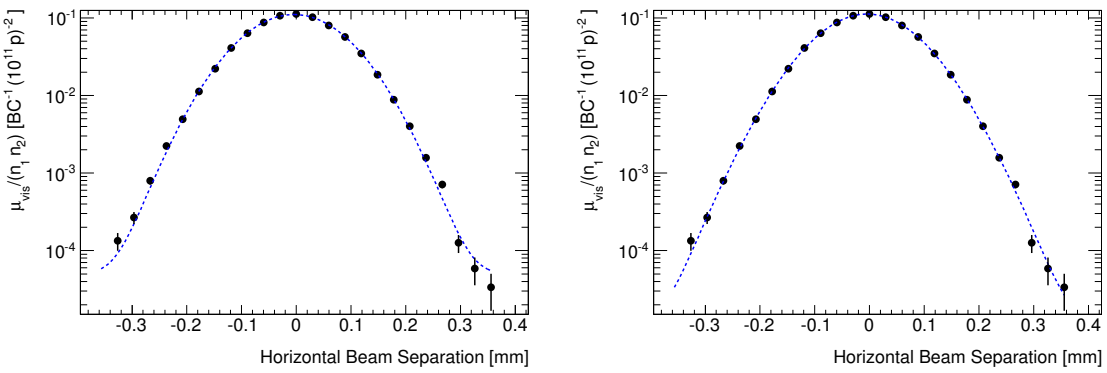

Figure 6.6 Comparison of a single-Gauss (left) and double-Gauss (right) fits to BCM-H Event-OR data. Plotted is the example of $\mu^{\mathrm{OR}}_{\mathrm{vis,sp}}$ for BCID 501 in scan IV$_x$.

$\mu_{\mathrm{vis,sp}}$ values, where the intensities are taken individually per BCID.

6.2 Event-OR

The pile-up correction on the OR-rate per bunch crossing is straight-forward using Equation 5.25. To extract the convolved beam sizes, the $\mu^{\mathrm{OR}}_{\mathrm{vis,sp}}$ values for each valid scan-point are plotted against the nominal separation and fitted with an appropriate

function. Figure 6.6 shows an example BCID of Event-OR data, plotted on a logarithmic scale to highlight the points in the tails. The left plot shows a single-Gauss+p0 fit, the right a double-Gauss+p0 fit to the data. It is clearly visible that the distribution has a non-negligible double-Gaussian component, and thus the tails are better described by the double-Gaussian model. For the Event-OR data this is the general case for all scan-curves.

The double-Gaussian model used, consists simply of the sum of two single-Gaussians with a common mean. For the horizontal coordinate the fit-function has the form (equivalently for the vertical coordinate):

$$\mathrm{P}(x) = \frac{\mathrm{P}_0}{\sqrt{2\pi}} \left[\frac{f_a \mathrm{e}^{-(x-x_0)^2/2\sigma_a^2}}{\sigma_a} + \frac{(1-f_a)\mathrm{e}^{-(x-x_0)^2/2\sigma_c^2}}{\sigma_c} \right] + p0, \tag{6.1}$$

with σ_a being the standard-deviation of the inner and σ_c of the outer Gaussian and f_a being the fraction of the inner- Gaussian.

As derived in the Section 5.2.1, the convolved beam size can be calculated as:

$$\Sigma_x = \left[\frac{f_a}{\sigma_a} + \frac{1-f_a}{\sigma_c} \right]_x^{-1} \tag{6.2}$$

Setting $x = x_0$ in Equation 6.1, one gets:

$$\mathrm{P}(x_0) = \frac{\mathrm{P}_0}{\sqrt{2\pi}} \left[\frac{f_a}{\sigma_a} + \frac{1-f_a}{\sigma_c} \right] = \frac{\mathrm{P}_0}{\sqrt{2\pi}\Sigma_x} \tag{6.3}$$

If Equation 6.2 is used to substitute σ_c in Equation 6.1, the resulting fit-function has Σ_x as one of the fit parameters. Therefore the fitted statistical uncertainties and correlation coefficients between $\Sigma_{x,y}$ and $\mu_{\mathrm{vis,sp}}^{\mathrm{MAX}}$ can be directly taken from the fit result.

6.3 Event-AND

Different to the Event-OR case, the expression, that relates $\mu_{\mathrm{vis}}^{\mathrm{AND}}$ to the raw event counts R_{AND} cannot be solved analytically. The Event-AND formula for pile-up correction (Equation 5.36) depends on $\sigma_{\mathrm{vis}}^{\mathrm{AND}}$, but this is exactly the value that is intended to be extracted. To get to the correct visible cross-section an iterative procedure is therefore used, that needs to be applied for each colliding bunch separately. One starts with the value of $\sigma_{\mathrm{vis}}^{\mathrm{OR}}$ for the corresponding BCID, that was extracted previously in the Event-OR analysis, and sets $\sigma_{\mathrm{vis}}^{\mathrm{AND}} = 1$. With these values $\mu_{\mathrm{vis}}^{\mathrm{AND}}$ gets numerically calculated from the measured rate R_{AND} per bunch crossing.
After correcting for the intensities, the resulting $\mu_{\mathrm{vis,sp}}^{\mathrm{AND}}$ values are then fitted for both scans to calculate a new $\sigma_{\mathrm{vis}}^{\mathrm{AND}}$. This is then input to a new μ-correction of the raw data. The procedure is repeated until $\sigma_{\mathrm{vis}}^{\mathrm{AND}}$ converges. Figure 6.7 illustrates the iterative procedure for the BCID-average $\left\langle \sigma_{\mathrm{vis}}^{\mathrm{AND}} \right\rangle$ in scans IV and V. It is clearly visible

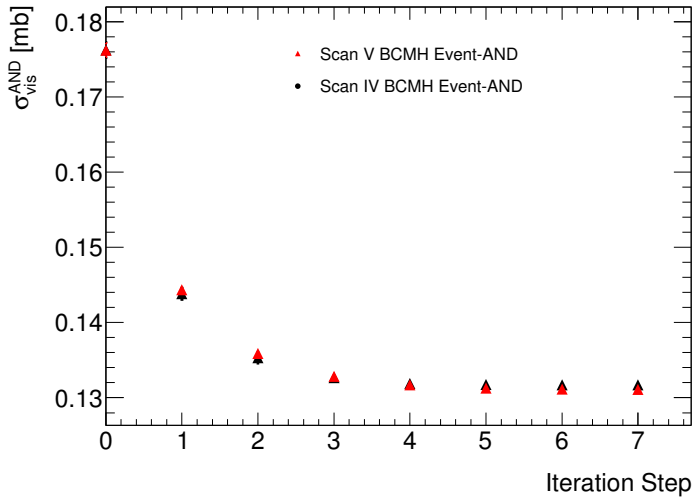

Figure 6.7 Iterative calculation of $\sigma_{\text{vis}}{}^{AND}$ using a numerical method. The first iteration step uses $\sigma_{\text{vis}}^{\text{AND}}$=1 for the μ correction. It is visible that the value converges after about six iterations.

that both calibration constants converge after about six iterations.
At each iteration step the $\mu_{\text{vis,sp}}^{\text{AND}}$ values are fitted with an appropriate function to extract $\Sigma_{x,y}$. While the double-Gaussian model describes the Event-OR data very well, attempts of fitting Event-AND data with Function 6.1 fail for many scan-curves, mainly for those of the horizontal scans. Although the fits converge, the error covariance matrix is often not positive definite and the fit-output has meaningless errors for $\Sigma_{x,y}$. The fit parameters clearly show that the scan curve tends to a single-Gaussian. For most fits either the widths of inner- and outer-Gaussian are equal, $\sigma_a \approx \sigma_c$, i.e. $\Sigma = \sigma_a = \sigma_c$ or the fraction $f_a \approx 1$, i.e.$\Sigma = \sigma_a$ or $f_a \approx 0$, i.e. $\Sigma = \sigma_c$. However one knows from statistically more reliable data (BCM Event-OR and from the analysis of the LUCID data [1]) that the convolved beam sizes are of double-Gaussian shape. Since the shape of the rate distribution should be independent of the algorithm, this inconsistency is most probably to be due to the low statistics of the Event-AND data. This will be investigated in the following Section with the help of a toy study.

6.3.1 Toy Study for Event-AND

The basic question of this test is: If one has true double-Gaussian distributions, but with low statistics - can the fallback to a single-Gaussian be explained by statistical fluctuations? The proper Event-OR double-Gaussian fits for each BCID and scan are taken as the true distributions. At each scan-point the $\mu_{\text{vis,sp}}^{\text{OR}}$ values are downscaled to $\mu_{\text{vis,sp}}^{\text{AND}}$ at head-on collisions, i.e. by the factor:

$$f = \frac{\mu_{\text{vis,sp}}^{\text{OR,MAX}}}{\mu_{\text{vis,sp}}^{\text{AND,MAX}}} \tag{6.4}$$

The downscaled $\mu_{\text{vis,sp}}^{\text{OR}}$ are then multiplied with the bunch charge product $n_1 n_2$ and an inverted Event-AND $\mu-$correction is applied. One is thus getting a distribution of events per BC that has the double-Gaussian Event-OR shape, but is downscaled to the Event-AND rate (which will be denoted as Event-AND$_{\text{gen}}$).

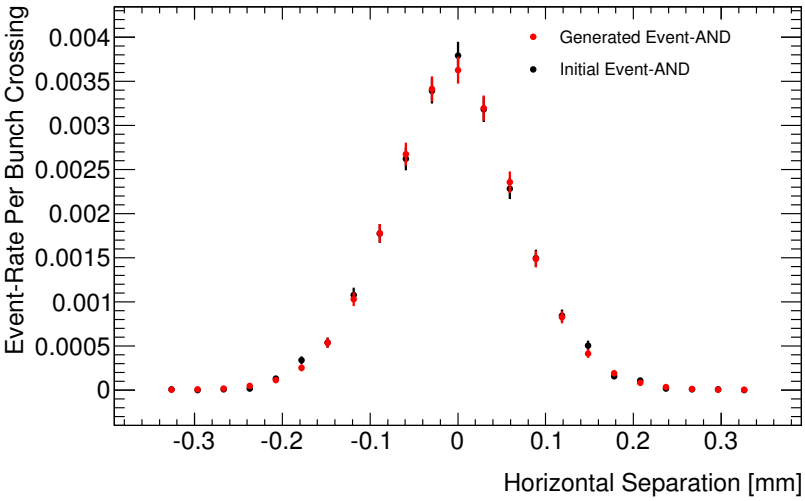

Figure 6.8 The red points show the Event-AND$_{\text{gen}}$ rate, generated from the Event-OR distribution, in black the real Event-AND distribution.

Figure 6.8 shows a comparison of Event-AND$_{\text{gen}}$ versus the true Event-AND data. It is visible that the black points, from the original Event-AND distribution, fluctuate around the generated double-Gaussian distribution (red). The Event-AND$_{\text{gen}}$ values are now multiplied with the number of bunch-crossings in the corresponding PLB, in order to calculate the total number of events for each scan-point. The resulting values are now randomized by a Poisson function to generate a number of toy-distributions:

$$\text{P}(N, \text{Raw}) = \frac{\text{e}^{-\text{Raw}}\text{Raw}^N}{N!} \tag{6.5}$$

where Raw is the Event-AND$_{\text{gen}}$ number of events per PLB, representing the mean expected number, and N the randomly generated value. From these generated raw Event-AND$_{\text{gen}}$ scan-curves the corresponding $\mu_{\text{vis,sp}}^{\text{AND}}$ are calculated and the double-Gaussian model using Equation 6.1 is again applied. The results from the toy-Event-AND data for both horizontal scans show that on average 45% of all BCIDs fall back to a single-Gaussian. This is in agreement with the real Event-AND data, where in these scans 50% of the BCIDs had a single-Gaussian shape.

One can thus conclude that random deviations at such low rates distort the double-

Gaussian scan shape significantly, and that the Event-AND single-Gaussian shape is solely due to the low statistics.

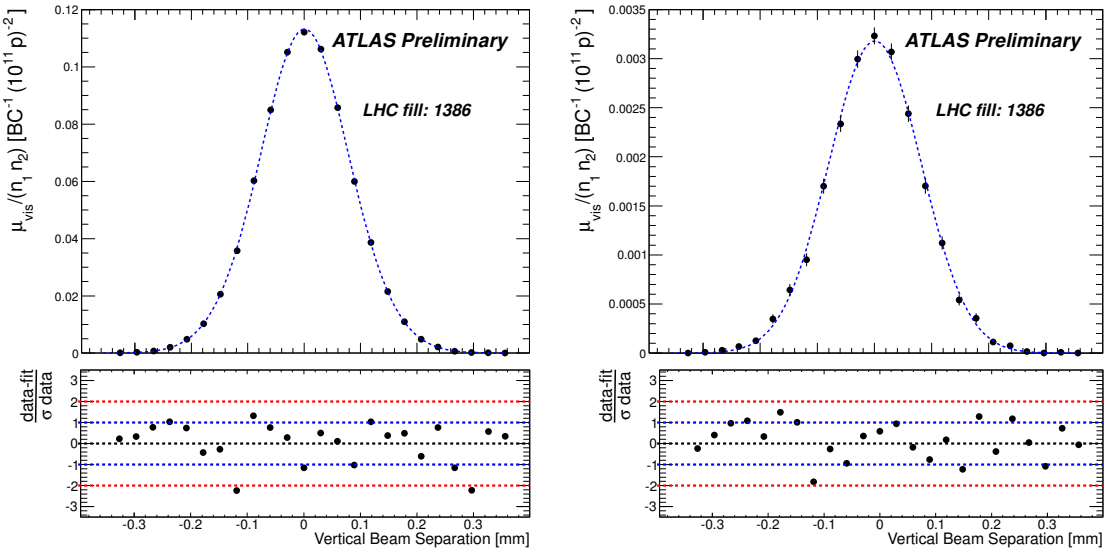

Figure 6.9 Example fits to the BCM-H scan data of BCID 1651 in scan IV_y, with the pull distribution below. Left is a single-Gaussian fit to Event-OR data, right a double-Gaussian fit to Event-AND. The vertical axis shows the colliding bunch number. The errors are statistical only.

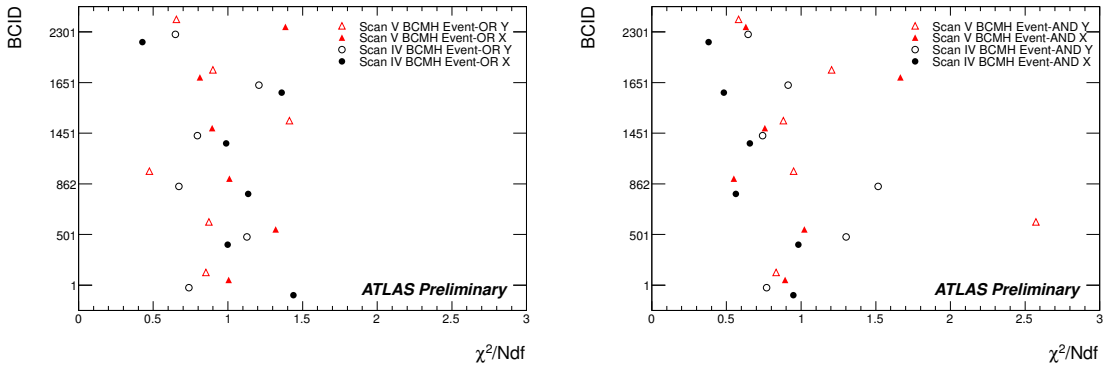

Figure 6.10 BCM-H χ^2/Ndf values of the double-Gaussian fits to the Event-OR data (left) and single-Gaussian fits to the Event-AND data (right) for scans IV and V. The vertical axis shows the colliding bunch number

6.4 Fit Results

Figure 6.9 shows two example fits to the specific visible number of interactions per bunch crossing $\mu_{\text{vis,sp}}$. It is visible from the pulls, shown in the lower canvas, that the fit to data-point differences are equally distributed around zero. The general fit quality for each colliding bunch and scan can be evaluated from the χ^2/Ndf values shown in Figure 6.10. Except Event-AND for BCID 501 V_y, the χ^2/Ndf values are generally below 2 which indicates a good fit quality.

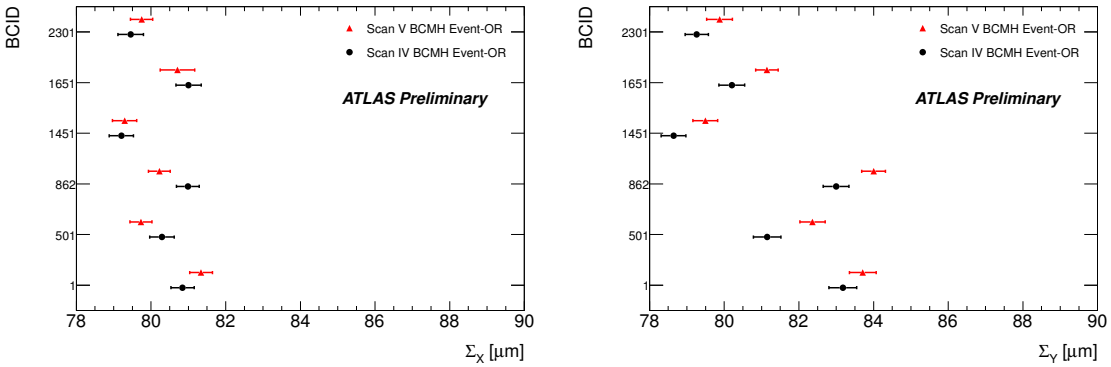

Figure 6.11 BCM-H horizontal (left) and vertical (right) convolved transverse beam sizes per BCID measured with Event-OR . In black scan IV, in red scan V. The errors are statistical only.

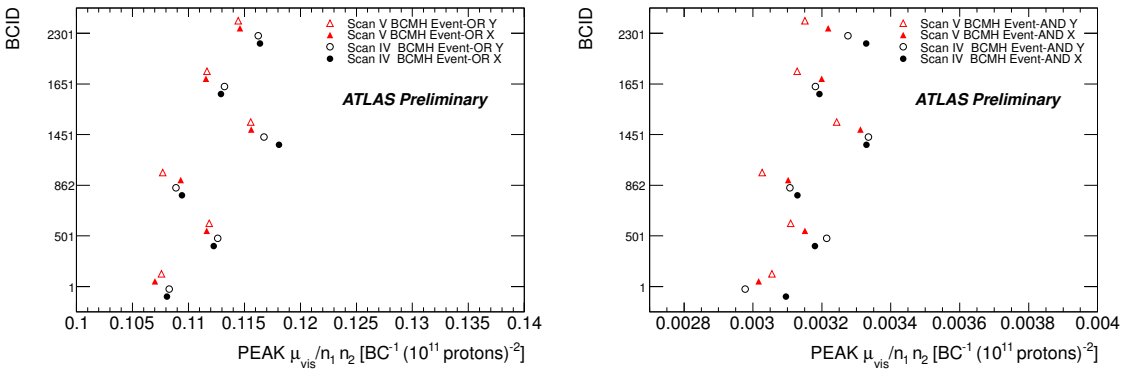

Figure 6.12 BCM-H peak $\mu_{\mathrm{vis,sp}}^{\mathrm{MAX}}$ values for Event-OR data (left) and Event-AND data (right) for scans IV and V. The vertical axis shows the colliding bunch number. The errors are statistical only

The convolved beam sizes are plotted in Figure 6.11 for Event-OR . For a given BCID and scan $\Sigma_{x,y}$ should be independent of the algorithm or detector, as they are intrinsic properties of the beam. The variation of $\Sigma_{x,y}$ between BCIDs of 79μm - 84μm is well within the expected range of bunch to bunch emittance variation. All beam widths in V_y are larger than in IV_y , while the widths in both x-scans are consistent within their statistical uncertainties. This indicates that an emittance growth is present in the vertical plane.

The maximum $\mu_{\mathrm{vis,sp}}^{\mathrm{MAX}}$ values are plotted in Figure 6.12. As these values depend on acceptance and efficiency they do not need to agree between algorithms. The peak rate for a given plane drops from scan IV to scan V, even though $\mu_{\mathrm{vis,sp}}$ includes an implicit correction for beam intensity decays. As observed in the Σ_y plots, this effect provides further evidence of emittance growth.

The peak positions of the fits, i.e. the position where the beams are colliding head-

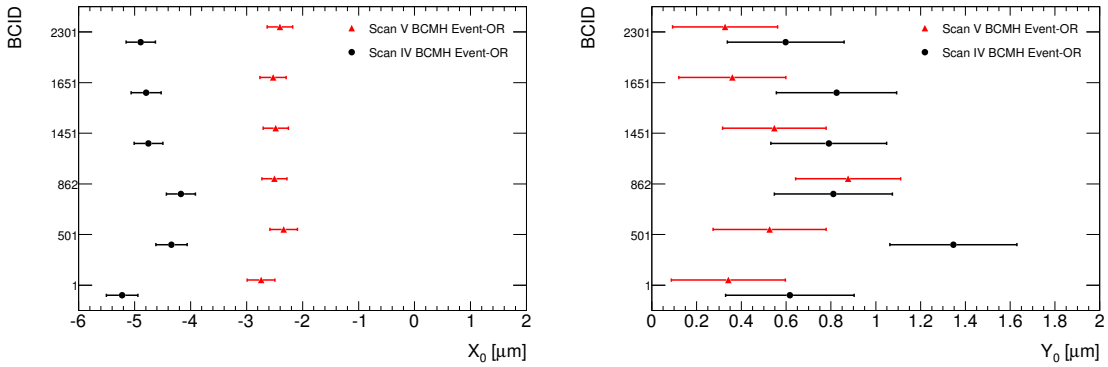

Figure 6.13 BCM-H horizontal (left) and vertical (right) peak position per BCID for Event-OR . In black scan IV, in red scan V. The errors are statistical only.

on, are plotted for both coordinates in Figure 6.13. This fit parameter does not directly enter the analysis, but is a significant indicator of reproducibility. The values are slightly offset from zero, less in the vertical than in the horizontal plane. All BCIDs in the horizontal plane have an offset of about 4.5μm for scan IV. This offset, which was discovered during the scan was corrected for by the LHC prior to the next scan. However, they did not succeed to adjust to zero nominal separation since scan V showed again a shift in the peak position by $\approx 2.5\mu$m.

For Event-OR the $p0$ term is about 10^{-4} smaller than $\mu_{\text{vis,sp}}^{\text{MAX}}$. The order of magnitude is also in agreement with the μ measured in the non-colliding bunches in Figure 6.3. Since no background correction was applied on the initial event-rates, one must assume that most of this term is background from beam-halo and beam-gas. Therefore this term is subtracted from the fit to $\mu_{\text{vis,sp}}$. Due to the strong background suppression of Event-AND no such contribution is expected.

6.5 Visible Cross-Section and Specific Luminosity Measurement

The combination of one $x-$ and one $y-$scan is needed to perform a measurement of the visible cross-section (see Equation 5.38). It is observed that in the fits $\Sigma_{x,y}$ and $\mu_{\text{vis,sp}}^{\text{MAX}}$ are highly anti-correlated (around to 80% for Event-OR). Thus, to calculate the statistical uncertainty on the visible cross-section, the correlation coefficient between these two parameters needs to be taken into account for each fit. The final values for σ_{vis} per BCID are listed in Table 6.2 and plotted in Figure 6.14. Since the values should be independent of BCID or scan number, the agreement of these values for a given algorithm reflects the reproducibility and stability of the calibration procedure

	BCMH_Event-OR σ_{vis}		BCMH_Event-AND σ_{vis}	
BCID	Scan IV	Scan V	Scan IV	Scan V
1	4.571 ± 0.0178	4.59 ± 0.0169	0.1323 ± 0.00187	0.1298 ± 0.00171
501	4.603 ± 0.0182	4.611 ± 0.0166	0.1322 ± 0.00191	0.1296 ± 0.00160
862	4.61 ± 0.0175	4.594 ± 0.0153	0.1312 ± 0.00167	0.1332 ± 0.00154
1451	4.595 ± 0.0173	4.578 ± 0.0164	0.1321 ± 0.00180	0.1326 ± 0.00153
1651	4.615 ± 0.0175	4.593 ± 0.0185	0.1307 ± 0.00184	0.1284 ± 0.00149
2301	4.603 ± 0.0174	4.584 ± 0.0161	0.1319 ± 0.00178	0.133 ± 0.00155
Average	4.6 ± 0.0071	4.592 ± 0.0067	0.1317 ± 0.00074	0.1311 ± 0.00064
χ^2/Ndf	0.7861	0.4747	0.1232	1.849

Table 6.2 Values of σ_{vis}[mb] as obtained from the fits per BCID. The average values are a weighted average of the individual bunches. The errors are statistical only.

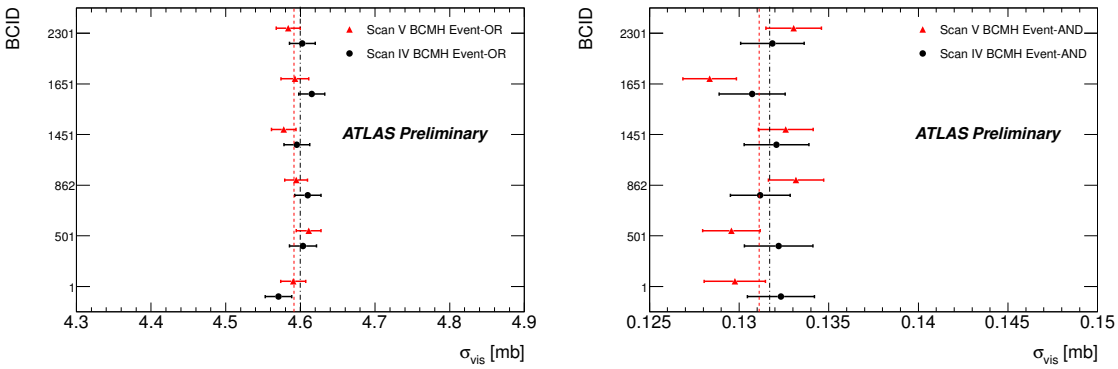

Figure 6.14 Results for the visible cross-section per BCID for BCM-H Event-OR (left) and Event-AND (right). In black scan IV, in red scan V. The dashed lines show the corresponding ratios of the weighted averages over all BCIDs. The errors are statistical only.

	BCM-H Event-OR $\mathscr{L}_{sp}$		BCM-H Event-AND $\mathscr{L}_{sp}$	
BCID	Scan IV	Scan V	Scan IV	Scan V
1	26.62 ± 0.2208	26.29 ± 0.2108	25.81 ± 0.6067	26.31 ± 0.5867
501	27.47 ± 0.2363	27.25 ± 0.2133	27.19 ± 0.6698	27.17 ± 0.5528
862	26.63 ± 0.211	26.56 ± 0.1975	26.73 ± 0.5721	25.88 ± 0.5002
1451	28.73 ± 0.2383	28.4 ± 0.2353	28.37 ± 0.6596	27.79 ± 0.5445
1651	27.55 ± 0.2332	27.33 ± 0.2576	27.42 ± 0.6596	27.72 ± 0.5331
2301	28.42 ± 0.2342	28.1 ± 0.2251	28.16 ± 0.6449	26.92 ± 0.5300

Table 6.3 Values of $\mathscr{L}_{sp}[10^{28}\text{cm}^{-2}\text{s}^{-1}\text{bunch}^{-1}(10^{22}\text{p})^{-1}]$ as obtained from the fits per BCID. The errors are statistical only.

during a single fill. The averages of measurements x_i, calculated in the following are weighted by their errors σ_i:

$$\langle x \rangle = \frac{\sum_{i=1}^{n_b}(x_i/\sigma_i^2)}{\sum_{i=1}^{n_b}(1/\sigma_i^2)}, \tag{6.6}$$

with the variance of the weighted mean calculated as:

$$\sigma^2_{\langle x \rangle} = \frac{1}{\sum_{i=1}^{n_b}(1/\sigma_i^2)} \tag{6.7}$$

The average values of σ_{vis} for Event-OR differ by 0.15% and by 0.45% for Event-AND between scan IV and scan V. This consistency between the two scans demonstrates that, to first order, the emittance growth cancels out of the measured luminosity calibrations (the increase of $\Sigma_{x,y}$ is compensated by a decrease of $\mu^{MAX}_{vis,sp}$). The consistency per BCID is expressed by χ^2/Ndf values, where χ^2 is calculated by:

$$\sum_{i=0}^{n_b} \frac{[x_i - \langle x \rangle]^2}{\sigma_i^2} \tag{6.8}$$

and the degrees of freedom Ndf is just $n_b - 1$, i.e. 5 for the October scan.

They are given in the last row of Table 6.2. With a maximum value of 0.8, for Event-OR scan IV, and a maximum of 1.9 for Event-AND in scan V, these values show that there is a good agreement of σ_{vis} within a scan which demonstrates again the reproducibility of the calibration technique.

By considering the distribution of the specific luminosity $\mathscr{L}_{sp}$, given by Equation 5.39, further checks can be made. Since this quantity depends only on the product of the convolved beam sizes, one expects consistent results from each algorithm for a given BCID. Table 6.3 shows the measured values per algorithm and scan for each colliding bunch plus the error weighted BCID-average. The variations between BCIDs are about 5-10%. This reflects the difference in transverse emittances which

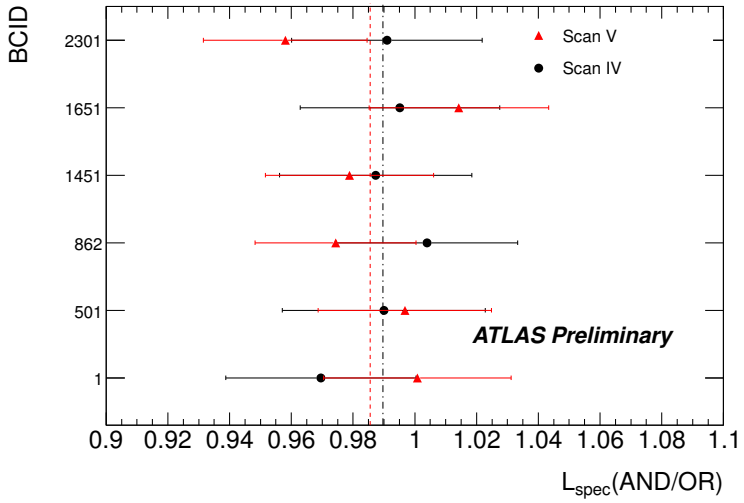

Figure 6.15 Ratio of BCM-H Event-AND and Event-OR specific luminosities per BCID. The dashed lines show the weighted average over all BCIDs.

is a typical value in physics operation. Again, the small systematic reduction between the averages of scan IV and V can be associated to emittance growth of the colliding beams. Figure 6.15 shows the AND/OR-ratio of $\mathscr{L}_{\mathrm{sp}}$ per BCID. The dashed lines are the AND/OR-ratio of the averages which are 0.99±0.0127 for scan IV and 0.986±0.0114 for scan V. The values being close to unity show that both algorithms give consistent results.

It was shown that the beam sizes and thus the luminosity can vary significantly amongst the colliding bunches within the same fill. Averaging the raw counts over the six colliding BCIDs before performing the analysis (a method also called *BCID-blind*) one ends up with final values that deviate by up to 1.4% for the calibration constant σ_{vis} and by up to 3.3% for the specific luminosity $\mathscr{L}_{\mathrm{sp}}$ to the per-bunch analysis. This clearly confirms the importance of performing the luminosity calibration on a per-bunch level. The final σ_{vis} values for all algorithms and their efficiencies, averaged over all colliding BCIDs and both scans are given in Table 6.4. These values were entered into the ATLAS online database and were thus used by the OLC to calibrate online- and offline- luminosity of the BCM. The next section will discuss the uncertainties affection the final result of BCM-H Event-OR .

6.6 Calibration Uncertainties

The uncertainties affecting the calibration constant σ_{vis} have been qualitatively explained in Section 5.5. All errors on $\sigma_{\mathrm{vis}}^{\mathrm{OR}}$ that were found to be relevant at the time of the October-scan will now be evaluated. The focus of the uncertainty discussion will be on the Event-OR algorithm, since this algorithm was found to be better understood

	BCM-H	
	σ_{vis} [mb]	ε
Event-OR	4.596	6.4×10^{-2}
Event-AND	0.1314	1.8×10^{-3}

Table 6.4 Final values of σ_{vis} averaged over all colliding BCIDs and scans IV and V. The resulting efficiencies of the algorithms are calculated assuming an inelastic *pp* cross-section of σ_{inel} =71.5 mb.

and statistically stronger than Event-AND .

6.6.1 Bunch Charge Product

The systematic uncertainties on the bunch charge product were explained in detail in Section 3.4.4. The values as determined by the BCNWG are listed in Table 6.5.

Scan Number	IV–V
Fill Number	1386
DCCT Baseline Offset	0.1%
DCCT Scale Variation	2.7%
Per-bunch Fraction	1.6%
Total	3.1%

Table 6.5 Systematic uncertainties on the determination of the bunch charge product $n_1 n_2$ in the October 2010 *vdM* scans IV and V [45]. The uncertainty on the ghost-charge and satellite bunches is included in the per-bunch fraction.

6.6.2 Beam Centering

In Figure 6.13 a maximum shift in the horizontal plane of $\approx 2.3\mu$m is visible, no such shift is visible in the vertical plane. With $\Sigma_x \approx 80\mu$m it is possible to calculate the corresponding uncertainty on σ_{vis}^{OR} using Equation 2.16, which results in about 0.04%.

6.6.3 Transverse Emittance Growth and Other Non-Reproducibility

Looking at the pull distributions of the fits versus the data-points, e.g. in Figure 6.9, no strong sign of emittance growth within a scan can be observed. The pulls are generally well centered around zero, and no sign of a scan curve distortion is visible.
Clear signs of emittance growth between two consecutive scans were shown before, manifested as an increase in Σ and a decrease in $\mu_{vis,sp}^{MAX}$ (see Figures 6.12 and 6.11).

In Table 6.2 the difference in the average $\sigma_{\text{vis}}^{\text{OR}}$ between scans IV and V is 0.2%. The per-bunch variations in $\sigma_{\text{vis}}^{\text{OR}}$ are all within their statistical uncertainty, and thus no additional error is added.

6.6.4 Beam Position Jitter

The variation in the beam-position due to a jitter was estimated to 0.8μm RMS. The systematic error on σ_{vis} due was estimated to be $\pm$0.3% [67].

6.6.5 Length Scale Calibration

	Horizontal	Vertical
Beam 1 Length Scale	1.003 ± 0.002	0.997 ± 0.002
Beam 2 Length Scale	0.995 ± 0.002	0.999 ± 0.002
Beam Separation Scale	0.999 ± 0.003	0.998 ± 0.003

Table 6.6 Results of the length scale calibrations at IP1. The values are the ratios between the displacement reconstructed with the ATLAS ID and the nominal separation as input to the LHC. Errors shown are statistical only from the linear fits [67].

The length scale procedure is described in Section 5.4.4 and the resulting scale correction factors are listed in Table 6.6. The values shown are the ratio between the beam displacement measured by ATLAS using the primary vertex position and the nominal separation given by the LHC. Ratios are shown both for each individual beam in both planes, but also for the beam separation length scale, which is the average of the correction for both beams and is the value which determines the convolved beam size in the *vdM* scan. The associated systematic uncertainty was estimated to $\pm$0.3%. The additional uncertainty from the absolute length scale of the ID was estimated in a Monte Carlo study to be $\pm$0.3% [67].

6.6.6 Fit Model

The fit model that is used in this scan to provide the final $\sigma_{\text{vis}}^{\text{OR}}$ values is double-Gauss+p0(B) , i.e. the p0 term is treated as background. In order to give an estimate about the fit model uncertainty, the Event-OR data has additionally been fitted with a double-Gauss+p0($\mathscr{L}$) , where the p0 term is added to the integral, and a Spline fit. The resulting values of $\sigma_{\text{vis}}^{\text{OR}}$ per BCID are plotted in Figure 6.16. The comparison shows that the results from all fit models agree well. Table 6.7 shows the averages over the colliding bunches. The highest deviation of about 0.25% can be found between the

Fit Model	Scan IV	Scan V
double-Gauss+p0(B)	4.60	4.592
double-Gauss+p0($\mathscr{L}$)	4.60	4.599
Spline	4.612	4.599

Table 6.7 BCID averages of $\sigma_{\text{vis}}^{\text{OR}}$ [mb] for Event-OR from three different fit-models.

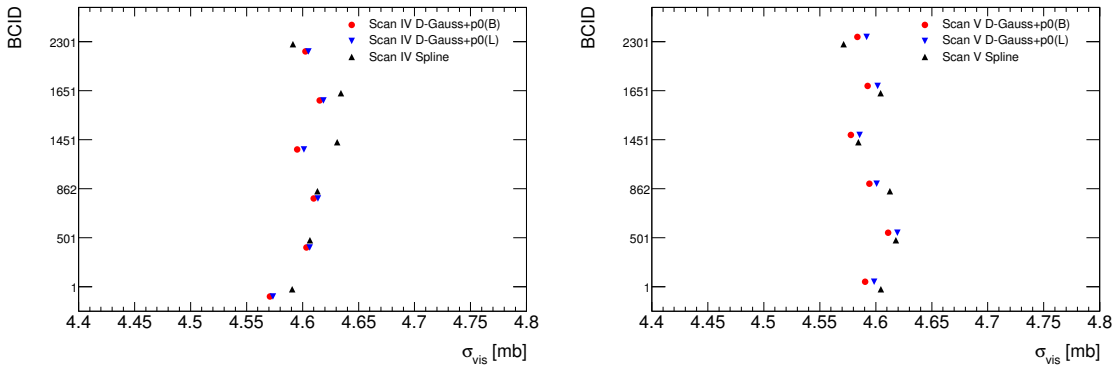

Figure 6.16 Results of σ_{vis} per BCID using three different fit models for BCM-H Event-OR . Shown is scan IV (left) and scan V (right).

double-Gauss+p0(L) and the double-Gauss+p0(B) fit in scan V. This value is taken as the systematic uncertainty on how well the beam shape is understood.

6.6.7 Transverse Correlation

Possible effects of $x-y$ correlations on σ_{vis} have been estimated by fitting the transverse distribution of event vertices measured with the ID, where an uncertainty of $\pm 0.9\%$ was determined [67].

6.6.8 μ Dependence

Scans IV and V were taken over the range of $0 < \mu < 1.3$. Figure 6.17 shows the variation between Event-AND and Event-OR in their predicted luminosity. Shown is the relative deviation of the BCID averaged $\langle \mu_{\text{AND}} \rangle$ to that of $\langle \mu_{\text{OR}} \rangle$ for all scans performed. One can discover a quite large discrepancy at low values. However, these values correspond to only a very short period of data acquisition where the statistics for Event-AND are very bad. Therefore small fluctuations in the measured rate can lead to large discrepancies in this ratio. The agreement between the two algorithms in the higher μ range is much better, and deviations are at maximum at the level of $\pm 3\%$. The stability of the Event-OR over a longer period can be evaluated by plotting its relative

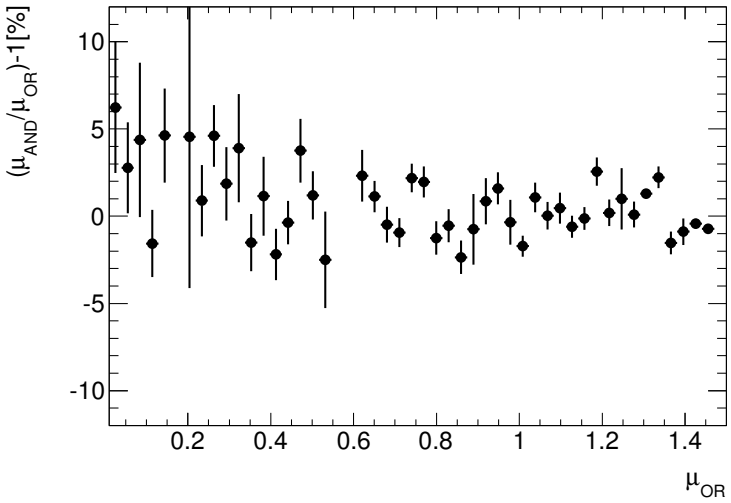

Figure 6.17 Relative deviation of the BCID-average value of μ obtained with Event-AND with respect to Event-OR both measured with BCM-H .

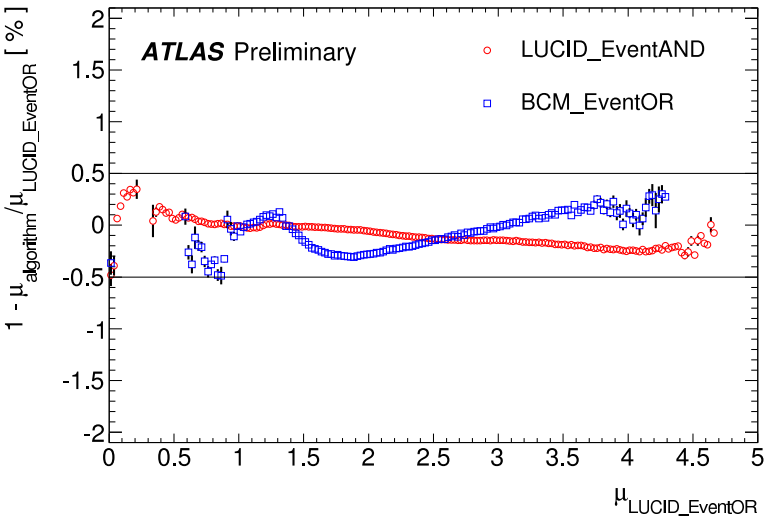

Figure 6.18 Relative deviation in the average value of μ obtained using different algorithms with respect to the LUCID Event-OR value as a function of μ over the 2010 data sample [67].

difference to that of LUCID Event-OR . Results over the full 2010 data sample are plotted in Figure 6.18. They show that the deviation is at most 0.5% [67], also within the range of the *vdM* -scan. On this basis an uncertainty of ±0.5% is assigned to the determination of σ_{vis} due to the μ correction within the scan.

6.6.9 Total Uncertainty of the Results

Scan Number	IV–V
Fill Number	1386
Source	Relative Uncertainty
Bunch Charge Product	3.1%
Beam Centering	0.04%
Emittance Growth	
and Other Non-Reproducibility	0.2%
Beam-Position Jitter	0.3%
Length Scale Calibration	0.3%
Absolute ID Length Scale	0.3%
Fit Model	0.25%
Transverse Correlations	0.9%
μ Dependence	0.5%
Total Calibration Uncertainty	3.4%

Table 6.8 Relative systematic uncertainties that affect the visible cross section $\sigma_{\text{vis}}^{\text{OR}}$ of BCM-H from *vdM* scans IV and V. For the total uncertainty the individual contributions are added in quadrature.

The final systematic uncertainties affecting σ_{vis} from scans IV and V are summarized in Table 6.8. The total uncertainty is given by the square-root of the individual uncertainties, added in quadrature. The final value of 3.4% is clearly dominated by the uncertainty affecting the bunch charge product.

By time of the October scan the preferred ATLAS luminosity detector-algorithm was LUCID Event-OR , however, the results from BCM provided important cross-checks on the LUCID measurements. For the total luminosity uncertainty affecting the 2010 data, the relative agreements between LUCID and BCM-H Event-OR are plotted versus date in Figure 6.19. The BCM was only fully operational at the end of the 2010 data taking period, the agreement up to a level of 5% proves the stability of both detectors. The total uncertainty affecting the BCM-H luminosity, can be estimated by the quadratic sum of the total uncertainty on σ_{vis} and the total uncertainty from the long-term stability, and is found to be 3.4%, as shown in Table 7.9. For illustration, the

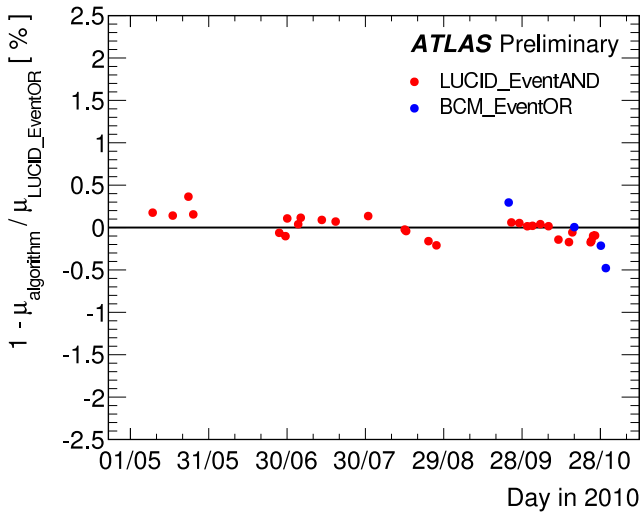

Figure 6.19 Relative deviation in the average value of μ obtained using different algorithms with respect to the LUCID Event-OR value as a function of time. Each point shows the average deviation for a single ATLAS run [67].

cumulative luminosity versus day within the 2010 running as determined by LUCID Event-OR is shown on Figure 7.23. In 2010, a total intregrated luminosity of 45 pb^{-1} was recorded by the ATLAS experiment.

Scan Number	IV–V
Fill Number	1386
Source	Relative Uncertainty
Long Term Stability	0.5%
Total, Luminosity Calibration Uncertainty	3.4%
Total, Luminosity Uncertainty	3.4%

Table 6.9 Relative systematic uncertainties on the luminosity.

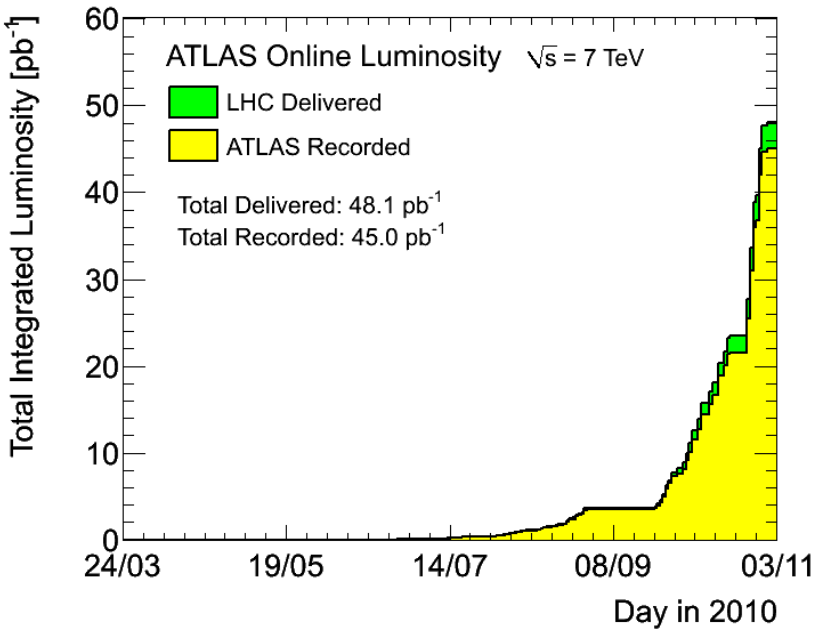

Figure 6.20 Cumulative luminosity versus day delivered to (green), and recorded by ATLAS (yellow) during stable beams for *pp* collisions at 7 TeV center-of-mass energy in 2010. The delivered luminosity accounts for the luminosity delivered from the start of stable beams until the LHC requests ATLAS to turn the sensitive detector off to allow a beam dump or beam studies. Given is the luminosity as determined with LUCID Event-OR [62].

Chapter 7

May 2011 *vdM* scan

	vdM Scan VII–VIII (15 May, 2011)
LHC Fill Number	1783
Scan Directions	2 Sets of x- and y- Scans
Total Scan Steps per Plane	25
Scan Range	$(\pm 6\sigma_b)$
Scan Duration per Step	20 s
Number of Colliding Bunches in ATLAS $[n_b]$	14
Total Number of Bunches per Beam	38
Number of Protons per Bunch $[n_{1,2}]$	$\sim 0.8 \times 10^{11}$
β-Function at IP $[\beta^\star]$ (m)	~ 1.5
Transverse Single Beam-Size $[\sigma_b]$ (μm)	~ 40
Full Crossing Angle $[\theta_c]$ (μrad)	240
Typical Bunch Luminosity (Hz/μb)	0.38
Typical μ	2.3

Table 7.1 Summary of the main characteristics of the 2011 *vdM* scan performed at the ATLAS interaction point. The values of luminosity/bunch and μ are given for zero beam separation. The transverse single beam size is given assuming nominal emittances $\varepsilon_N = 3.75\mu$m

Before and during the early 2011 data taking period a number of changes were made in order to improve the readout of LUCID and BCM. In early April 2011, at the time of an LHC technical stop, the LUCID receiver cards were changed to improve the performance of the readout with 50 ns bunch-spacing. This was found to have an impact on the LUCID calibration of about 3%. During the winter shut-down in 2010/11, resistors of the BCM front-end boards were replaced to increase the dynamic

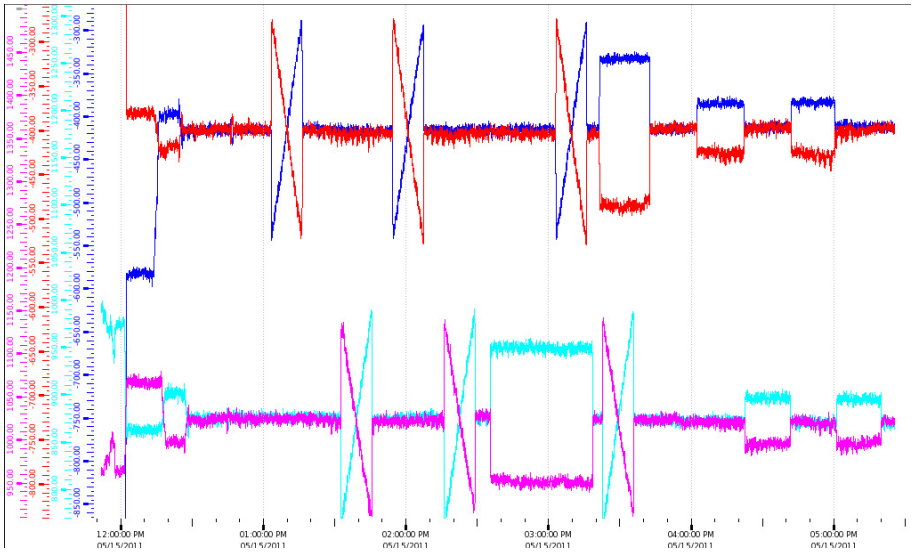

Figure 7.1 The position of the beams versus time during the May 2011 scans, as measured with the BPM. The horizontal position of beam 1 (beam 2) is plotted in blue (red), the vertical position of beam 1 (beam 2) in magenta (pink). Clearly visible are three scan-sets, where in the last one the beams were offset in the non-scanning plane. After 4 p.m. a *vdM* scan in CMS (IP5) took place where the beams at the ATLAS IP were offset by $1.4\sigma_b$. Note that this beam position measurement can be used only for illustration purposes only and is e.g. not suited to optimize the collision point.

range of the low-gain BCM signal, that is used for beam abort decisions. For the high gain BCM signal, that is used for luminosity measurements it was assumed that variations in the efficiency at the level of a percent were possible. A second change in 2011 happened during data taking, where on the 21st of April the BCM thresholds were adjusted [2]. After this change the luminosity measured by BCM-H Event-OR was observed to increase with respect to other detectors by 3.1%, and that of BCM-V by about 4.1%, which implies that σ_{vis} also increased by these amounts. Due to these changes the calibrations extracted from the October 2010 scans were not expected to be directly applicable to the 2011 data. For this reason it was decided to re-calibrate the luminosity detectors. And a new set of *vdM* scans took place on the 15th of May 2011.

The sequence of the May scans was similar to the ones taken during the October scans. Two "standard" *vdM* scans (VII and VIII) were performed in order to test the reproducibility of the results. These were followed by an offset scan, where the beams were offset by $4\sigma_b$ in the non-scanning plane, in order to study systematics due to possible transverse correlations. The procedure for each scan itself was left unchanged with respect to the October scans, a horizontal scan was followed by a vertical scan. Each scan consisted of 25 scan-steps spanning a nominal separation of $\pm 6\sigma_b$. At the acquisition points where the beams were kept stable, data were recorded for a duration

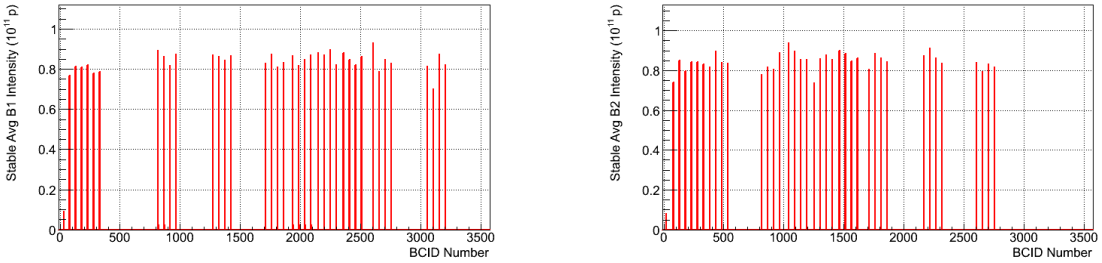

Figure 7.2 Per-bunch intensities versus BCID measured with the BPTX during the *vdM* scan for beam 1 (left) and beam 2 (right) [76]

Private bunches (shared only with IP5)						
BCID	81	131	181	231	181	331
Shared with IP5 and IP2						
BCID	817	867	917	967		
Shared with IP5 and IP8						
BCID	2602	2652	2702	2752		

Table 7.2 BCIDs of the private and shared bunches that were colliding in ATLAS during the May *vdM* scan. This table indicates at which IPs the BCIDs were additionally colliding. Note, bunch 917 was additionally colliding with a low intensity bunch in IP8

of 20 s. In view of only small $x-y$ offsets, that could be determined with an online analysis of the measured rates, no mini scans were performed. Figure 7.1 illustrates the scanning sequence by showing the beam position in horizontal and vertical direction for beam 1 and beam 2, respectively, versus time. The beam positions are determined by the beam position monitor measurements on either side of the IP, interpolated to the interaction region.

A summary of the scan characteristics is given in Table 7.1. While the scanning sequence remained the same, filling scheme and beam parameters did change substantially. The bunch intensities were increased to of the order of $8\times10^{10}\,p$. The nominal transverse single beam size was reduced to $\approx 40\,\mu$m, by squeezing the beam to $\beta^* = 1.5$ m. Compared to the October scan, this almost doubled the interaction rate per bunch crossing to $\mu \approx 2.3$. This had the big advantage of allowing to gather more statistics at each scan point, without expanding the duration of the *vdM* scan. On the other hand, a higher μ value requires a better understanding of the pile-up correction applied and higher bunch intensities give rise to higher beam background, which can potentially affect the measurements.

The total number of bunches was raised to 38 per beam. 14 of these bunches were

colliding in IP1(ATLAS) of which only six were *private bunches*, i.e. only colliding in IP1 and IP5 (CMS). Four bunches were additionally shared with IP2 (ALICE) and the four others with IP8 (LHCb). The corresponding BCIDs are listed in Table 7.2. The higher number of colliding bunches allows one to have a better handle on systematic effects, by comparing the results obtained from different BCIDs. The per-bunch intensities of the two beams, as measured with the BPTX, are plotted in Figure 7.2.

Improvements in the online luminosity infrastructure were made, so that this time also data from the exclusive Event-XORC and all algorithm-rates from the vertical BCM-V modules could be stored to the conditions database. Since the pile-up correction for the exclusive single sided OR-algorithms, i.e. XORA(C), are difficult to calculate [66], it was decided to calibrate the inclusive OR-algorithms, i.e. ORA(C) instead. The probabilities could be calculated offline by:

$$\mathrm{P_{ORC}} = \mathrm{P_{XORC}} + \mathrm{P_{AND}} \tag{7.1}$$

$$\mathrm{P_{ORA}} = \mathrm{P_{OR}} - \mathrm{P_{XORC}} \tag{7.2}$$

The following chapter will present the *vdM* analysis for Event-OR , Event-AND , Event-ORA and Event-ORC for both BCM-H and BCM-V . If not otherwise stated all results presented are done with the online BCM data stored to `COOL` .

7.1 Fitting the Data

The interpolation problem in the BCM read-out software, as described in 5.5.1, still persisted at the time of the scans. As in the October scan it was therefore decided to discard the first scan-point at -0.36 mm from the fits. The procedure of calculating $\mu_{\mathrm{vis,sp}}$ was left unchanged. The pile-up correction for the additional single-sided OR-algorithms is equivalent to that of Event-OR . However, attempts of fitting the data with the double-Gaussian model, defined in Equation 6.1, gave unacceptable χ^2 values, or non-positive definite correlation matrices for many scan-curves. From the fit parameters it became obvious that the second-Gaussian component in the beam profiles is very small (if present at all). Consistent with the observations from LUCID [77], the May-scan data was therefore found to be best described by a single-Gaussian plus constant term:

$$\mathrm{P}(x) = \frac{\mathrm{C}}{\sqrt{2\pi}} \mathrm{e}^{-(x-x_0)^2/2\Sigma_x^2} + \mathrm{p0} \tag{7.3}$$

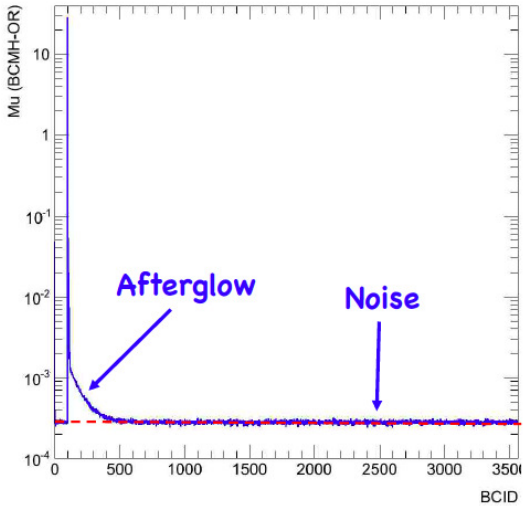

Figure 7.3 μ measured with BCM-H Event-OR versus BCID in ATLAS run 190728. The fill had only a single high intensity bunch. The signal-decay in the BCM Event-OR data suggests that the afterglow continues for roughly 300 BCIDs, then the shape flattens out to a constant noise level. The resulting shape of this fill can be used to model the afterglow in fills with any kind of bunch-pattern [78].

7.2 Background in the *vdM* scan

As explained in Chapter 3.3 one needs to consider single-beam backgrounds, in particular beam-gas events, produced by protons interacting with residual gas, and afterglow, that is producing rates following the collisions. In 2010 these backgrounds were assumed to be corrected for by subtracting the constant $p0$ term from the fit function, and not including it into the determination of $\Sigma_{x,y}$. For the May 2011 scans, a more detailed background subtraction was performed already on the raw rates measured in each BCID. Each background component is evaluated individually by a dedicated method, which will be explained in the following.

7.2.1 Estimating the Afterglow Background

Afterglow is known to scale with the luminosity and to produce rates typically of the order of 0.01% of the signal in the BCIDs right after collisions. In a fill with only 14 well separated colliding bunches the afterglow contribution is therefore expected to be rather low. Its contribution in the *vdM* -scan was estimated by using a single-bunch fill that was performed on October 2011. This fill provided a clean shape of the afterglow-tail following a single collision, which could then be used to model the afterglow in the *vdM* fill with multiple colliding bunches [74]. The μ versus BCID, as measured with BCM-H Event-OR , is shown in Figure 7.3. The BCM detectors were in addition found to have a small noise pedestal which can be estimated by averaging the BCIDs in the

abort-gap within the fill, as these BCIDs are empty and well separated of collisions. The resulting $\mu_{\text{vis,sp}}^{\text{AG,Noise}}$, i.e. the μ values for afterglow and noise, are determined for each colliding bunch separately.

7.2.2 Estimating the Beam-Gas Background

Background due to beam-gas interactions is known to scale with the intensity of the beams. Since the luminosity is scaling with the product of both beam intensities, the beam-gas contributions, relative to the signal, gets lower with higher beam intensity in normal physics fills. The situation is different in a *vdM* scan, because one needs to assume that the beam-gas is independent of the beam-separation. Therefore their relative contribution gets stronger with higher separation, i.e. in the tails of the scan-curves.
The 20 unpaired bunches in the LHC fill can be used to calculate the beam-gas contribution, and to estimate a correction for the OR-algorithm rates. Like the colliding bunches, the raw rate of each unpaired bunch must first be corrected for afterglow. The afterglow corrected rates are now used to calculate $\mu_{\text{vis,sp}}^{\text{BG}}$, i.e. the μ value of beam-gas. Each of the 20 $\mu_{\text{vis,sp}}^{\text{BG}}$ values is now divided by the current in the corresponding bunch, resulting in an intensity weighted average rate per bunch crossing for each unpaired bunch. The results are then averaged over all unpaired bunches of each beam separately to get two global beam-gas correction factors $\left\langle \mu_{\text{vis,sp,B}_1}^{\text{BG}} \right\rangle$ and $\left\langle \mu_{\text{vis,sp,B}_2}^{\text{BG}} \right\rangle$, where the indices B_1 and B_2 label the beam. A separate estimation for each of the two beams is necessary because their backgrounds are in general different. The beam-gas contributions for BCID i can now be calculated by multiplying the two averages with the intensity of BCID i in each beam:

$$\mu_{\text{vis,sp}}^{\text{BG}}(i) = n_1(i) \cdot \left\langle \mu_{\text{vis,sp,B}_1}^{\text{BG}} \right\rangle + n_2(i) \cdot \left\langle \mu_{\text{vis,sp,B}_2}^{BG} \right\rangle \tag{7.4}$$

7.2.3 Subtraction of the Total Background

According to Equation 5.25 $\mu_{\text{vis}}^{\text{OR}}$ is a non-linear function of the number of events. One therefore cannot simply subtract the μ values of signal and background. In order to correct the luminosity of a bunch, the raw event-rates N must be re-calculated by applying an inverse pile-up correction on the $\mu_{\text{vis,sp}}$ measured in the bunch to be corrected, and for each background contribution $\mu_{\text{vis,sp}}^{\text{BG}}$ and $\mu_{\text{vis,sp}}^{\text{AG,Noise}}$ separately. Furthermore one needs to assume that the background on side A- and C- is different and thus one also needs to take the correct combinatorics for Event-OR into account. With P_{ALGO} denoting the raw rate per bunch-crossing (i.e. the probability) of the signal, measured with the corresponding algorithm, and P_{bALGO} being the probability for background, measured with these algorithms, one gets the following correction [79]:

$$P_{OR} = \frac{P_{OR}^{meas} - (P_{bXORA} + P_{bXORC} - P_{bXORA}P_{bXORC})}{1 - P_{bXORA} - P_{bXORC} + P_{bXORA}P_{bXORC}} \tag{7.5}$$

A more detailed derivation of this formula can be found in Appendix D.3. Note that also the unpaired bunches for the beam-gas estimation must be corrected for afterglow using these formulas. The colliding bunches are then corrected for the sum of afterglow and beam-gas rate in the corresponding BCID. Note that due to the low statistics in the tails, the corrected rate at some scan-points gets negative. These values are then set to zero.

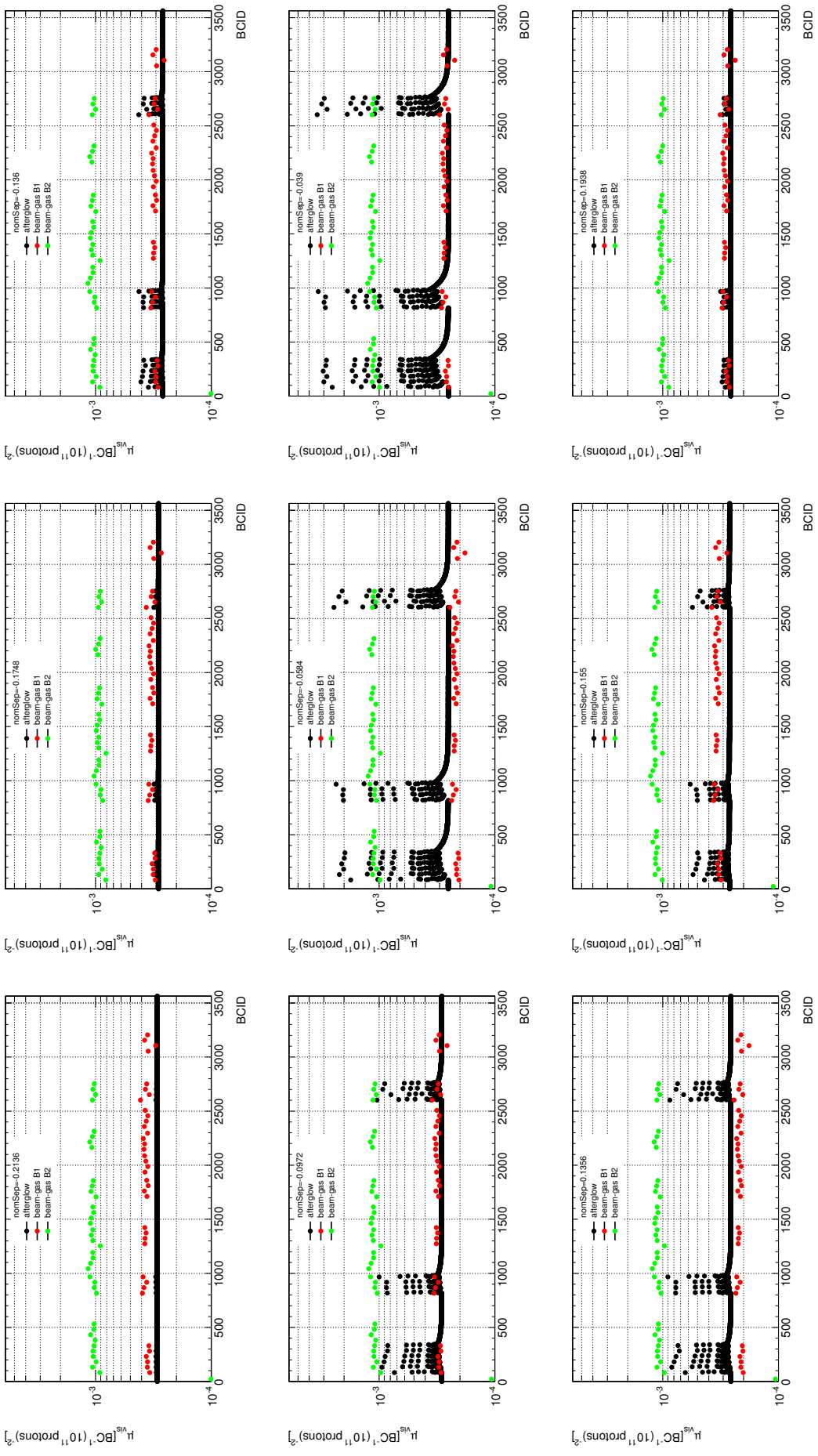

Figure 7.4 Background evolution in BCMH Event-OR versus BCID at different steps of nominal separation.

Figure 7.4 shows the background evolution at different scan-steps in form of μ_{vis}, as estimated for BCM-H Event-OR with the above described procedures. The afterglow plus noise contribution is shown in black. For large separated beams this background is at a constant noise level of 3×10^{-4}. When the beams are brought together it is clearly visible how afterglow is building up in the BCIDs following the collisions. The afterglow drops back below the noise level when the beams are separated again. The beam-gas component from beam 1 is plotted in red and that of beam 2 in green. Over the whole scan, both remain constant, independent of the separation. The beam-gas from beam 2, however, is at a μ_{vis} of about 10^{-3} and more than three times as large as that of beam 1. The source for such a discrepancy in the beam-background of the two beams is not fully understood. It might result from differences in the quality of vacuum on the two sides of the IP [74].

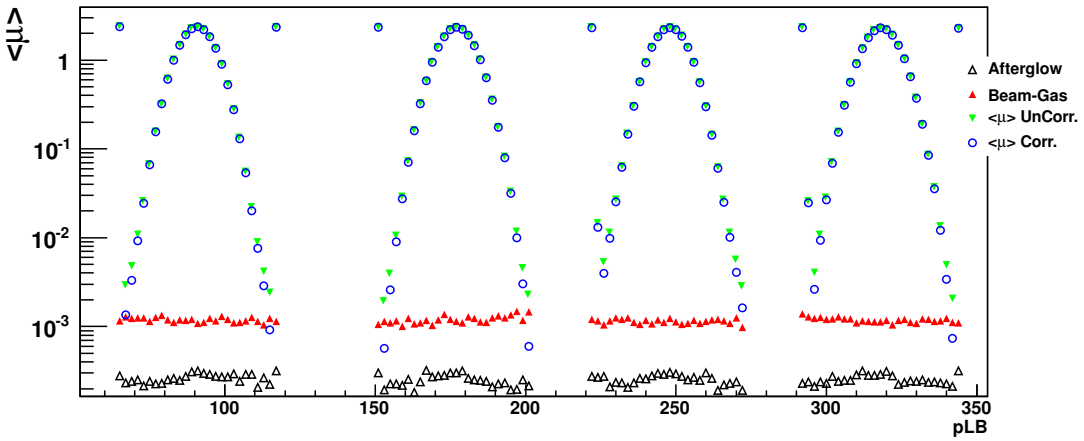

Figure 7.5 Average $\langle\mu\rangle$ values of beam-gas and afterglow and the signal values of the colliding bunches, before and after the background correction. Plotted are the rates versus PLB number for scans VII and VIII.

Figure 7.5 shows the May *vdM* scan in form of BCID-averaged $\langle\mu\rangle$ versus PLB. Plotted are the two background components (here the sum of beam-gas contributions from both beams is taken) and the signal rate of the average colliding bunches, before and after the correction. It is clearly visible, that in the center of the scans (i.e small separation) the background is negligible, the afterglow is only of the order 10^{-4} of the peak rate and the beam-gas only about 5×10^{-4}. Consequently the corrected and uncorrected signal rates are similar in this region. However, the situation is different in the tails of the scans. Here the beam-gas contribution is of the same order as the signal rate (and sometimes even higher) and a clear difference between corrected and uncorrected μ is visible.

Figure 7.6 shows a comparison of uncorrected and corrected $\mu_{\text{vis,sp}}$ for an example BCID. The effect of background correction is clearly visible in the tails of the scans. It

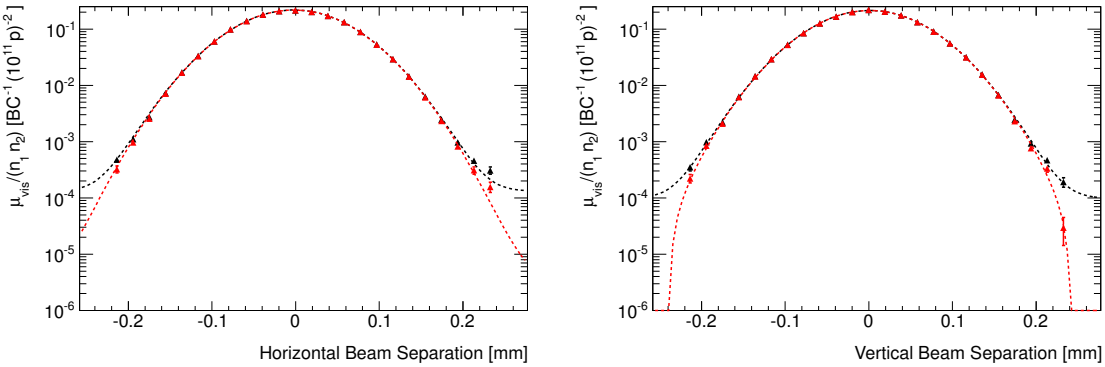

Figure 7.6 Example fits to the BCM-H Event-OR scan data of BCID 131 VII_x (left) and VII_y (right) without background correction (black) and with correction (red).

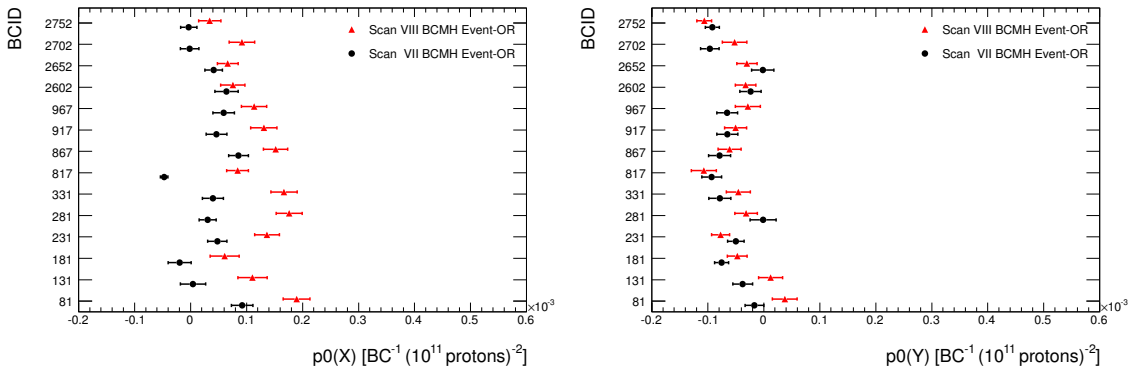

Figure 7.7 p0 term from the fits to BCM-H Event-OR after subtracting the background.

affects the scan-shape slightly, in particular the constant $p0$ term. Of course the missing point at -0.36 mm would have improved the fit-description in this regime significantly. Comparing horizontal and vertical profiles one finds that both scan-profiles are slightly different, in particular the tails in the y-scans have generally lower counts.

Figure 7.7 shows the constant fit parameter $p0$ for BCM-H, after the background correction for different BCIDs. In the fits to the vertical beam profiles $p0$ is negative for almost all BCIDs, whereas it is positive in the horizontal scan-direction (the same is observed for BCM-V). Since a background correction in Event-OR has been performed, one can assume that all fitted $\mu_{\mathrm{vis,sp}}$ is signal, including the $p0$. The justification to allow this term to become negative is that it is added to the fit-function to provide a better description of the scan-shape and not for a background correction as in the October scans. To verify that the remaining $p0$ is signal, the fraction of $p0$ to $\mu^{\mathrm{MAX}}_{\mathrm{vis,sp}}$ between the background corrected data of BCM to LUCID Event-OR has been compared.

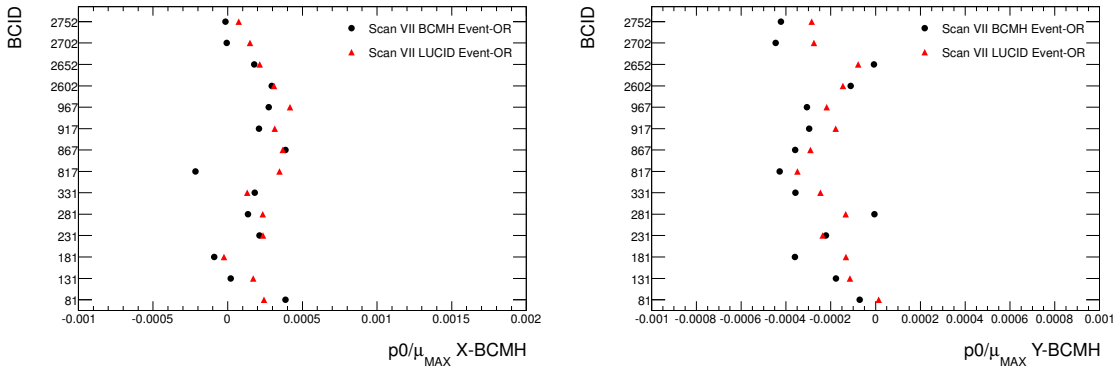

Figure 7.8 The ratio of $\mu_{\text{vis,sp}}^{\text{MAX}}$ over the constant $p0$ term for BCM-H Event-OR and LUCID Event-OR versus BCID for scan VII_x (left) and VII_y (right). Clearly visible is that the ratios for both detectors are of the same order.

This comparison is shown in Figure 7.8 for scan VII. It is visible that both detectors give consistent ratios for all colliding bunches in both planes. Because the signal-to-background ratio of both detectors is significantly different, one would expect these ratios to differ between both detectors if there was still a large background component in the $p0$. The full fit function, including the $p0$ term, must be considered and the fit-model that is used for Event-OR is therefore single-Gauss+$p0(\mathscr{L})$. The same procedure is done for the Event-ORA and Event-ORC data. The Event-AND algorithm has an intrinsic suppression of any background due to its coincidence requirement. With the given bunch pattern in this *vdM* scan it is therefore justified to assume the Event-AND rates to be background free.

7.3 Fit Results

The number of fitted scan-curves for this analysis increases to 56 (14 colliding bunches, two scan-sets) for each of the four algorithms. As also data from the BCM-V modules is available it further doubles the amount of data to be analyzed.

The single-sided algorithms are mainly used for monitoring and background studies and are not used for precision luminosity determination. Therefore the focus will be mainly on the Event-AND and Event-OR analysis. Figure 7.9 shows two example fits to Event-OR of BCM-H and Event-AND of BCM-V , respectively. As in the October scans, the fit quality for all BCIDs and scans is good. The χ^2/Ndf values of both modules are well between 1 and 2 (with only a few exceptions), as shown in Figure 7.10. However, looking at the pull distributions of the left-hand plot of Figure 7.9 one clearly sees a non-Gaussian modulation. Such a sinusoidal behavior of the pulls is observed for a few BCIDs, mainly in scans of the horizontal plane. The same is observed in the LUCID data [67]. This indicates that the single-Gaussian model may be not fully

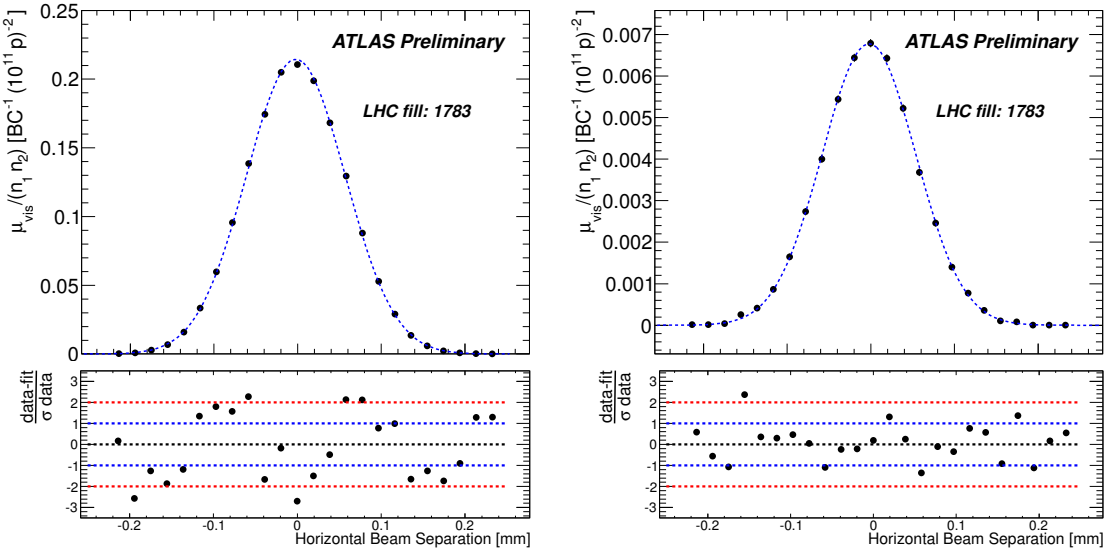

Figure 7.9 $\mu_{\mathrm{vis,sp}}$ versus nominal separation. Left is a fit to BCID 181 from BCM-H Event-OR data in scan VII$_x$. Right is shown a fit to BCM-V Event-AND data of BCID 281 VII$_x$. The errors are statistical only.

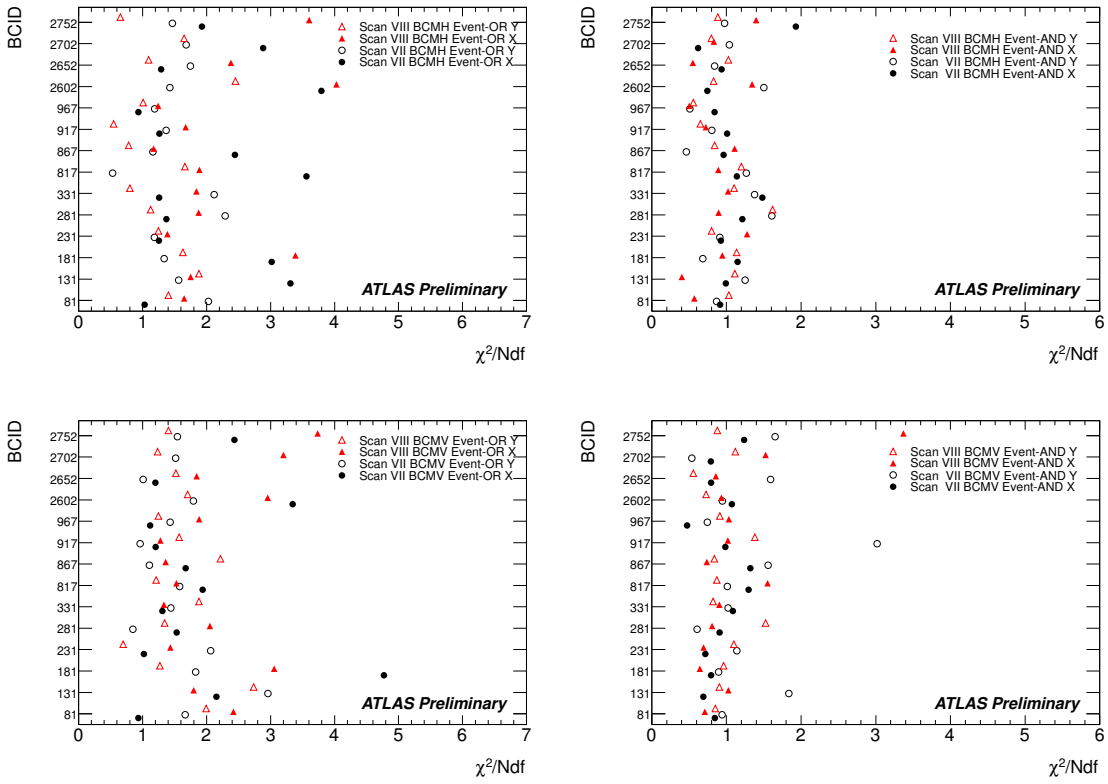

Figure 7.10 χ^2/Ndf values of the Gaussian fits to the Event-OR data(left) and single-Gaussian fits to the Event-AND data (right) for scans VII and VIII. The top plots are from BCM-H , the bottom ones from BCM-V . The vertical axis shows the colliding bunch number.

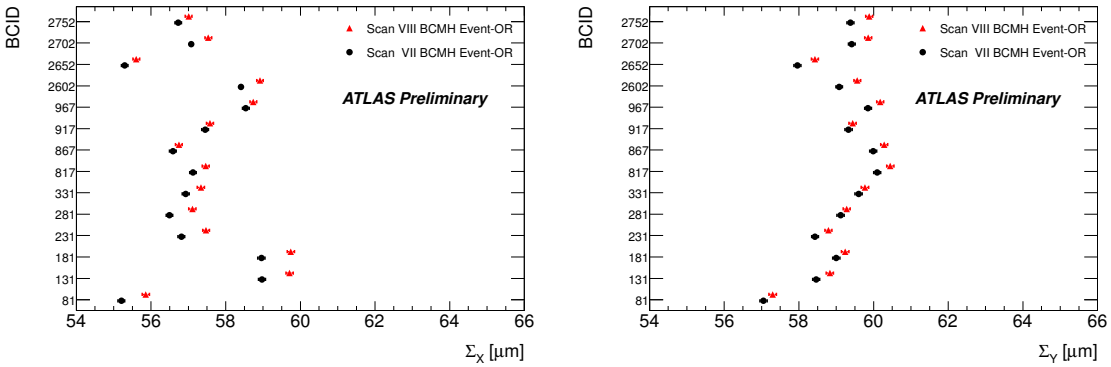

Figure 7.11 BCM-H horizontal (left) and vertical (right) convolved transverse beam sizes per BCID measured with Event-OR . In black scan VII, in red scan VIII. The errors are statistical only.

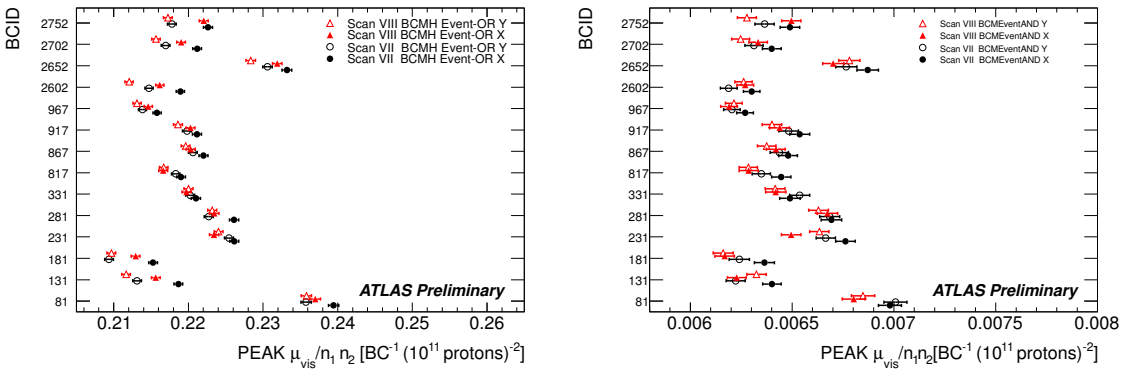

Figure 7.12 BCM-H peak $\mu_{\mathrm{vis,sp}}^{\mathrm{MAX}}$ values for Event-OR data (left) and Event-AND data (right) for scans VII and VIII. The vertical axis shows the colliding bunch number. The errors are statistical only.

appropriate to describe the scan-shape. The systematic error resulting on σ_{vis} will be covered by the fit model uncertainty.

The convolved beam sizes are plotted in Figure 7.11, for each of the 14 bunch pairs colliding in ATLAS. The effect of emittance growth between the two scans is clearly visible, with a growth of about 1μm in Σ_x and about 0.5μm in Σ_y. The maximum $\mu_{\mathrm{vis,sp}}$ is plotted in Figure 7.12, where the effect of emittance growth is also visible by a decrease in $\mu_{\mathrm{vis,sp}}^{\mathrm{MAX}}$ from scan VII to scan VIII. Since the emittance growth is in both planes, one would ideally expect the decreasing-order to be linked to the chronology of the scan, i.e. VII_x , VII_y , VIII_x , VIII_y , which is true for most cases, but however not for all.

Figure 7.13 shows the fitted position of the peak in the horizontal and vertical scans. These plots show an interesting feature of the scan. As already mentioned before, the colliding bunches in this scan can be assigned to three groups as listed in Table 7.2,

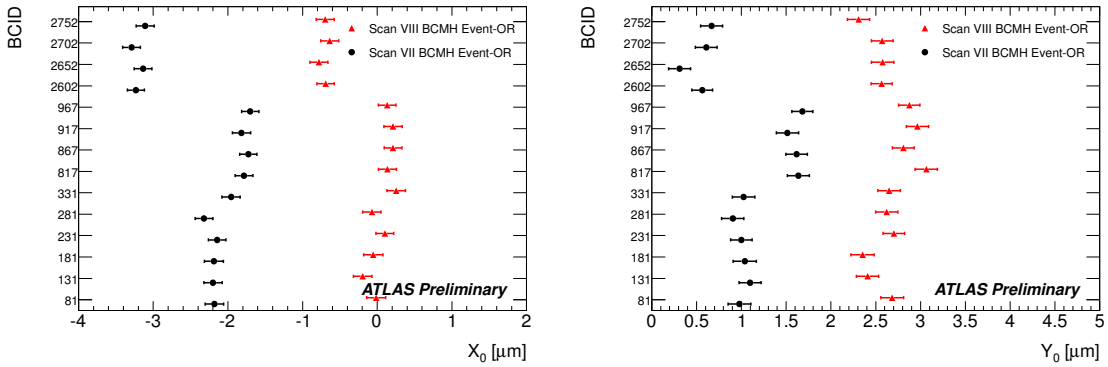

Figure 7.13 BCM-H horizontal (left) and vertical (right) peak position per BCID for BCM-H Event-OR . In black scan VII, in red scan VIII. The errors are statistical only.

depending on where else than at IP1 (and IP5) they collide. This pattern is clearly reflected in Figure 7.13, where one sees the corresponding groups of BCIDs with different peak positions. As explained in 5.5.2 collisions at other IPs have an impact on the beam-orbit: At each additional collision point, where the two beams were separated by $\approx 1.4\sigma_b$[1] in the scanning plane, the beam receives an additional defocussing force (a "kick") along the scanning plane. The pattern therefore reflects the cumulative effect of beam-beam deflections at the other IPs.

7.4 Visible Cross-Section and Specific Luminosity Measurement

Figure 7.14 shows the measured visible cross-sections for the colliding BCIDs. The weighted averages of σ_{vis} over the colliding BCIDs is indicated by the dashed lines. These values are in addition listed in Table 7.3 for Event-OR and in Table 7.4 for Event-AND . Comparing the average σ_{vis} values to the results of the October scans, an increase in the BCM-H efficiency of about 2% for Event-OR and about 5% for Event-AND is observed. This can be attributed to the BCM hardware changes mentioned at the beginning of this chapter. As in the October scan, the results of the first scan-set cannot be fully reproduced by the second scan-set. The σ_{vis} from scan VIII are systematically below those of scan VII. The non-reproducibility is of about the same order BCM-H and BCM-V . The absolute values of σ_{vis} , and thus the efficiencies, differ by about 0.7% for Event-OR and by about 0.6% for Event-AND .

[1] This separation was done in order to test if it is possible to perform *vdM* scans simultaneously at different IPs. A separation of 1.4 σ_b was chosen because there the luminosity is most sensitive to any orbit changes.

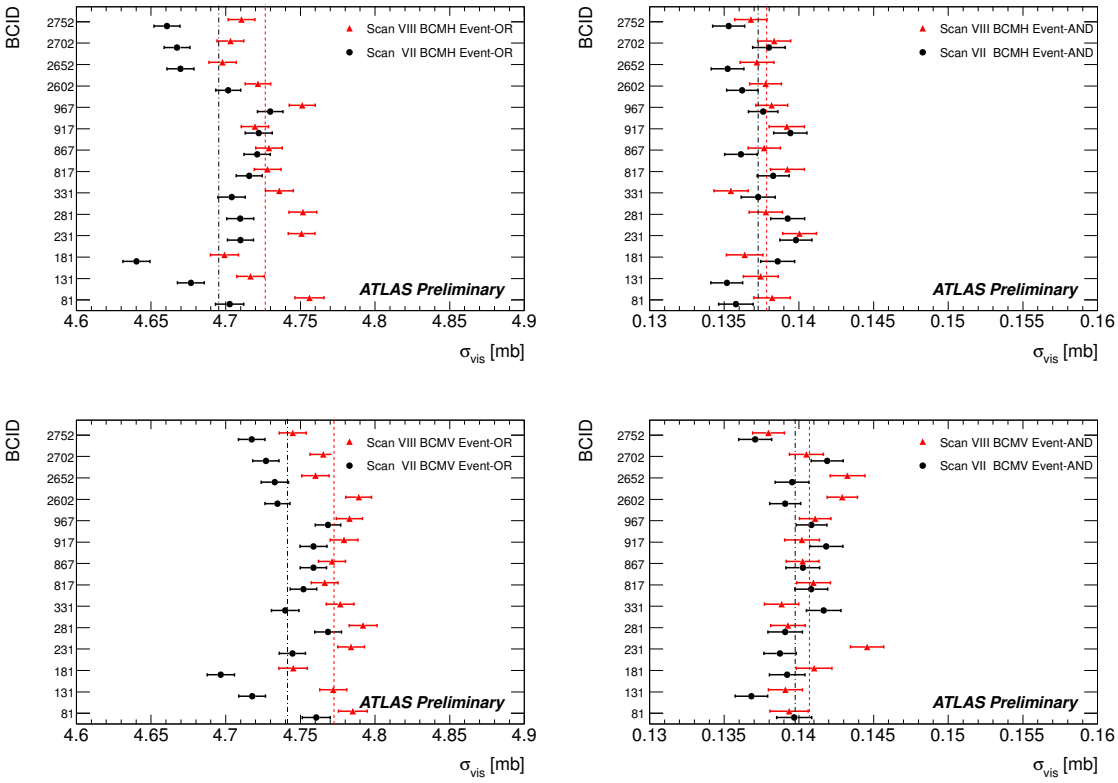

Figure 7.14 Results for the visible cross-section per BCID for Event-OR (left) and Event-AND (right). In black scan VII, in red scan VIII. The dashed lines show the corresponding ratios of the weighted averages over all BCIDs. The errors are statistical only.

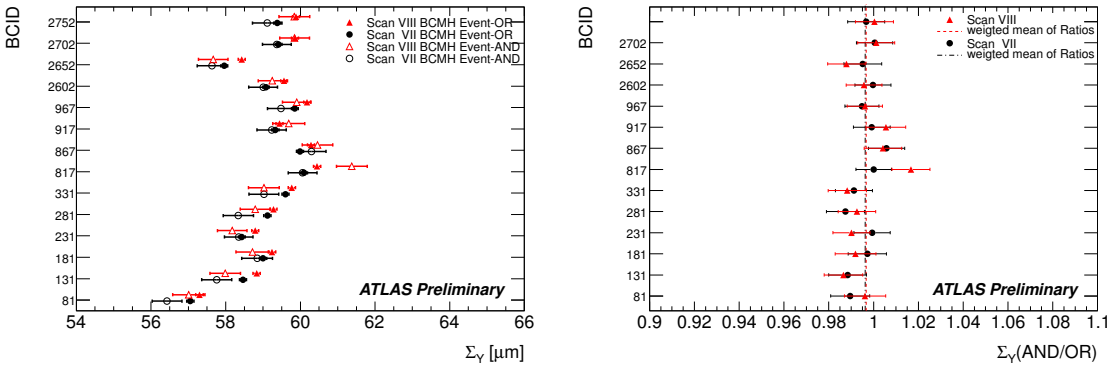

Figure 7.15 Comparison of Σ_y for Event-OR and Event-AND of BCM-H. The left plot shows a comparison of the fitted values, the right plot shows their ratio. The errors are statistical only.

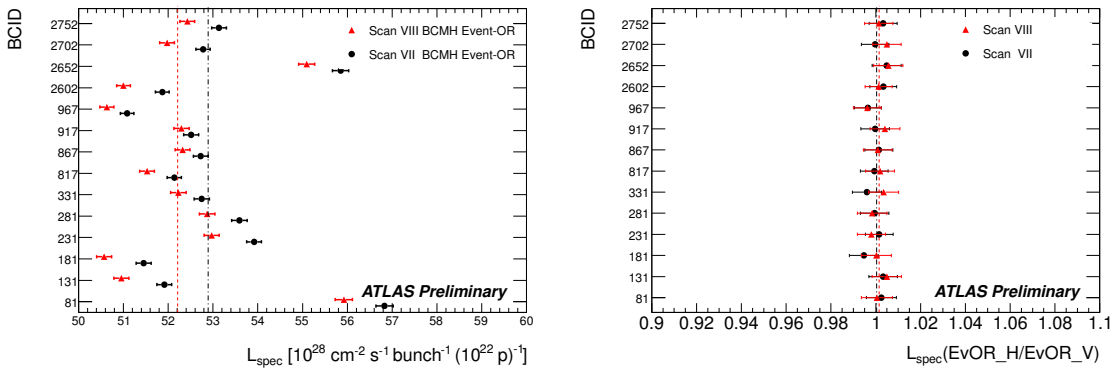

Figure 7.16 Specific luminosity measured at zero separation with Event-OR (left) of BCM-H . The right side shows the Event-OR $\mathscr{L}_{\text{sp}}$ ratio of BCM-H to BCM-V . The dashed lines show the weighted averages. The errors are statistical only.

	BCM-H Event-OR σ_{vis}		BCM-V Event-OR σ_{vis}	
BCID	Scan VII	Scan VIII	Scan VII	Scan VIII
81	4.703 ± 0.009	4.756 ± 0.010	4.761 ± 0.009	4.785 ± 0.010
131	4.677 ± 0.009	4.717 ± 0.009	4.718 ± 0.009	4.772 ± 0.009
181	4.640 ± 0.009	4.699 ± 0.009	4.697 ± 0.009	4.745 ± 0.009
231	4.710 ± 0.009	4.751 ± 0.009	4.745 ± 0.009	4.784 ± 0.009
281	4.710 ± 0.009	4.752 ± 0.009	4.769 ± 0.009	4.792 ± 0.009
331	4.704 ± 0.009	4.736 ± 0.009	4.740 ± 0.009	4.777 ± 0.009
817	4.716 ± 0.009	4.728 ± 0.009	4.752 ± 0.009	4.766 ± 0.009
867	4.721 ± 0.009	4.729 ± 0.009	4.759 ± 0.009	4.771 ± 0.009
917	4.722 ± 0.009	4.720 ± 0.009	4.759 ± 0.009	4.779 ± 0.009
967	4.730 ± 0.008	4.751 ± 0.009	4.768 ± 0.009	4.783 ± 0.009
2602	4.702 ± 0.008	4.722 ± 0.009	4.735 ± 0.008	4.789 ± 0.009
2652	4.670 ± 0.009	4.698 ± 0.009	4.733 ± 0.009	4.760 ± 0.009
2702	4.667 ± 0.009	4.703 ± 0.009	4.727 ± 0.009	4.765 ± 0.009
2752	4.661 ± 0.009	4.711 ± 0.009	4.717 ± 0.009	4.745 ± 0.009
Average	4.695 ± 0.002	4.726 ± 0.002	4.741 ± 0.002	4.773 ± 0.002
χ^2/Ndf	9.398	4.905	5.779	2.640

Table 7.3 Values of σ_{vis}[mb] as obtained from the fits per BCID. The average values are a weighted average of the individual bunches. The errors are statistical only.

	BCM-H Event-AND σ_{vis}		BCM-V Event-AND σ_{vis}	
BCID	Scan VII	Scan VIII	Scan VII	Scan VIII
81	0.1358 ± 0.0012	0.1382 ± 0.0012	0.1397 ± 0.0012	0.1393 ± 0.0013
131	0.1352 ± 0.0011	0.1374 ± 0.0012	0.1368 ± 0.0011	0.1391 ± 0.0011
181	0.1386 ± 0.0011	0.1364 ± 0.0012	0.1392 ± 0.0012	0.1410 ± 0.0012
231	0.1398 ± 0.0011	0.1400 ± 0.0011	0.1387 ± 0.0011	0.1446 ± 0.0011
281	0.1392 ± 0.0011	0.1378 ± 0.0011	0.1391 ± 0.0012	0.1393 ± 0.0012
331	0.1373 ± 0.0011	0.1354 ± 0.0011	0.1417 ± 0.0012	0.1388 ± 0.0011
817	0.1383 ± 0.0011	0.1392 ± 0.0011	0.1408 ± 0.0011	0.1410 ± 0.0011
867	0.1361 ± 0.0011	0.1377 ± 0.0011	0.1403 ± 0.0011	0.1402 ± 0.0011
917	0.1394 ± 0.0011	0.1392 ± 0.0012	0.1418 ± 0.0011	0.1402 ± 0.0012
967	0.1376 ± 0.0010	0.1382 ± 0.0011	0.1408 ± 0.0010	0.1411 ± 0.0011
2602	0.1362 ± 0.0010	0.1378 ± 0.0011	0.1391 ± 0.0010	0.1429 ± 0.0010
2652	0.1352 ± 0.0011	0.1372 ± 0.0011	0.1395 ± 0.0011	0.1433 ± 0.0012
2702	0.1380 ± 0.0011	0.1383 ± 0.0011	0.1419 ± 0.0011	0.1405 ± 0.0011
2752	0.1353 ± 0.0011	0.1368 ± 0.0011	0.1371 ± 0.0011	0.1380 ± 0.0011
Average	0.1373 ± 0.0003	0.1378 ± 0.0003	0.1398 ± 0.0003	0.1407 ± 0.0003
χ^2/Ndf	2.2812	1.0900	2.1197	2.7701

Table 7.4 Values of σ_{vis}[mb] as obtained from the fits per BCID. The average values are a weighted average of the individual bunches. The errors are statistical only.

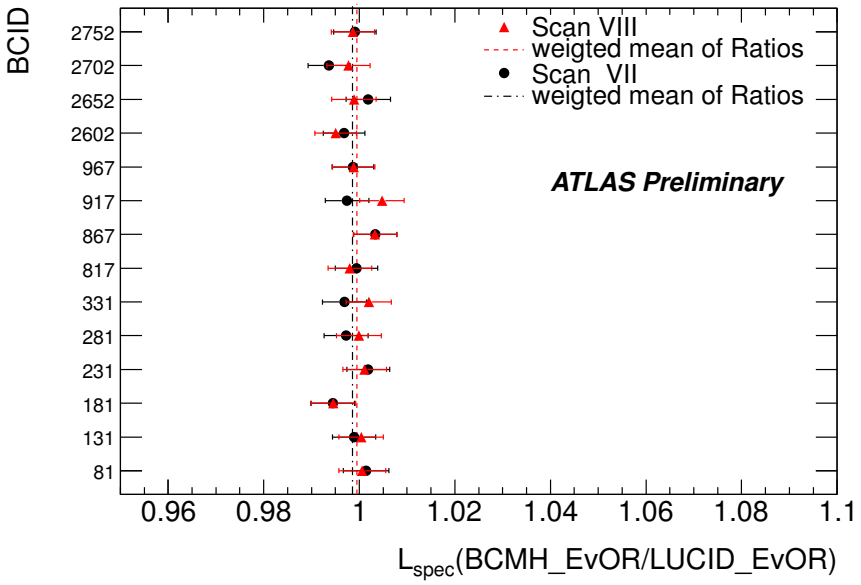

Figure 7.17 Ratio of $\mathscr{L}_{sp}$ measured with Event-OR of BCM-H to LUCID. The dashed lines show the weighted averages that are very close to one for both scans.

Even though this scan was performed with a higher μ than the October scan and thus more events could be accumulated per scan point, Event-AND still suffers from low statistics. In particular in the tails the number of events counted per PLB are generally below 3 and sometimes even zero. Comparing the convolved beam-sizes to those of Event-OR , one sees that they deviate for many BCIDs. Figure 7.15 shows the BCM-H results for the vertical scans. Clearly visible is that the Event-AND $\Sigma_{x,y}$ are systematically lower than those of Event-OR . The specific luminosities obtained with Event-OR of BCM-H are plotted in Figure 7.16 on the left. The 5-10% bunch-to-bunch variation can again be assigned to differences in the transverse emittances. Emittance growth is visible as a reduction of $\mathscr{L}_{\mathrm{sp}}$ form scan VII to scan VIII. The ratio of $\mathscr{L}_{\mathrm{sp}}$ between BCM-H and BCM-V for Event-OR is plotted on the right side. The weighted averages over the colliding BCIDs are close to one and reveal a good agreement between BCM-H and -V. A further comparison is given in Figure 7.17, which shows the $\mathscr{L}_{\mathrm{sp}}$ measured with BCM-H Event-OR to that of LUCID Event-OR . The dashed lines are showing the weighted average that are 0.9986 ± 0.00121 and 0.9995 ± 0.00122 for scans VII and VIII, respectively. This indicates that the agreement between the two independent detectors is very good.

The final σ_{vis} values for all algorithms and their efficiencies, averaged over all colliding BCIDs and both scans are given in Table 7.5. These values were entered into the OLC configuration, and thus calibrated online- and offline- luminosity of the BCM. The next section will discuss the uncertainties affection the final result of BCM-H Event-OR .

	BCM-H		BCM-V	
	σ_{vis} [mb]	ε	σ_{vis} [mb]	ε
Event-OR	4.694	6.6×10^{-2}	4.740	6.6×10^{-2}
Event-AND	0.138	1.9×10^{-3}	0.140	2.0×10^{-3}
Event-ORA	2.404	3.3×10^{-2}	2.439	3.4×10^{-2}
Event-ORC	2.427	3.4×10^{-2}	2.434	3.4×10^{-2}

Table 7.5 Final values of σ_{vis} [mb] averaged over all colliding BCIDs and scans VII and VIII. The resulting efficiencies of the algorithms are calculated assuming an inelastic *pp* cross-section of σ_{inel} =71.5 mb.

7.5 Calibration Uncertainties

The focus of the uncertainty discussion will be on the Event-OR algorithm measured with BCM-H data, as this algorithm provides the most stable results. The horizontal modules are believed to be best understood and were therefore chosen as the pre-

ferred BCM detector. Some uncertainties have been evaluated from the LUCID Event-OR data, which is the algorithm with best statistics. These are documented elsewhere [77, 48, 67] and are therefore only briefly mentioned in this thesis.

7.5.1 Bunch Charge Product

An overview over the beam intensity measurements was given in 3.4.4. The October scans showed that one of the dominant uncertainties was introduced through the bunch population normalization ($n_1 n_2$) used in Equation 5.37. In order to improve this uncertainty a detailed study of these measurements was carried out by the BCNWG group. The data from the FBCT, were compared to several different data sets from different devices which have sensitivity to the relative bunch charge population, including the BPTX. The results of this analysis indicated that the possible systematic effects of the measurements of the bunch population on the extracted cross-section are about 0.2%, which reduces the error by a large amount. Details on this analysis can be found in [80].

Scan Number	VII–VIII
Fill Number	1783
DCCT Baseline Offset	0.1%
DCCT Scale Variation	0.21%
Per-Bunch Fraction	0.20%
Ghost Charge & Satellites	0.44%
Total	0.54 %

Table 7.6 Systematic uncertainties on the determination of the bunch charge product $n_1 n_2$ for the May *vdM* scans VII and VIII [80].

Additional corrections to the per-bunch fraction are made to correct for ghost-charge, and satellite bunches which are described in detail in [81]. Table 7.6 lists all the systematic uncertainties affecting the bunch charge product.

7.5.2 Beam Centering

The maximum observed non-reproducibility in relative beam position can be estimated from Figure 7.13 to be about 3μm. Using Equation 2.16 this corresponds to an error of 0.1% on the luminosity. It is therefore slightly larger than in the October scan.

7.5.3 Transverse Emittance Growth and Other Non-Reproducibility

The simultaneous increase of beam sizes and decrease of the peak interaction rate between scans is clearly visible in Figures 7.11 and 7.12. The effect on σ_{vis} together with other non-reproducibilities can be estimated from the bunch averaged results in Figure 7.14. The deviation of σ_{vis} between scan VII and scan VIII for Event-OR is 0.7% at maximum for both modules. This is taken as the systematic uncertainty and is thus slightly higher than in the October scan.

7.5.4 Beam Position Jitter

The estimation of the beam position jitter has been performed using the LUCID data. The method was explained in 5.5.8. The re-centering of each scan step within the length-scale calibration scans yields shifts of 0.6μm RMS. The uncertainty on σ_{vis} was estimated to be 0.3% [67].

7.5.5 Bunch-to-Bunch σ_{vis} Consistency

If one compares the per-bunch σ_{vis} results within a scan in Figure 7.14 or in Table 7.3, some correlation between the values can be observed that is not entirely statistical in nature – no such effect was visible in the October scan. In particular BCIDs 81-181 reveal a trend that is seen in both BCM modules and is also observed in the LUCID data [67]. An additional systematic uncertainty of 0.6% has been applied from the RMS variation of $\sigma_{\text{vis}}^{\text{OR}}$.

7.5.6 Length Scale Calibration and Absolute ID Length Scale

The length-scale calibration has been performed using the LUCID data in [82]. The method was explained in 5.4.4 and 5.5.7. An uncertainty of 0.3% has been evaluated. An additional uncertainty due to the length scale of the ATLAS ID was estimated to be also 0.3%.

7.5.7 Fit Model and Background Subtraction

It was already discussed that some fits yield a small non-Gaussian component, and a modulation in their pulls is visible, e.g. in Figure 7.9. Figure 7.18 shows the Event-OR results of σ_{vis} per BCID using three different fit-functions. The BCID averages of each are given in Table 7.7. The largest variation of 0.5% is found to be between single-Gauss+p0(B) and the Spline fits for BCM-H in scan VIII which is taken as an additional systematic uncertainty. Which is significantly larger than the value in the October scan.

	BCM-H		BCM-V	
Fit Model	Scan VII	Scan VIII	Scan VII	Scan VIII
Gauss+p0(B)	4.697	4.743	4.719	4.769
Gauss+p0($\mathscr{L}$)	4.695	4.726	4.741	4.773
Spline	4.684	4.721	4.727	4.763

Table 7.7 BCID averages of $\sigma_{\text{vis}}^{\text{OR}}$ for Event-OR from three different fit-models.

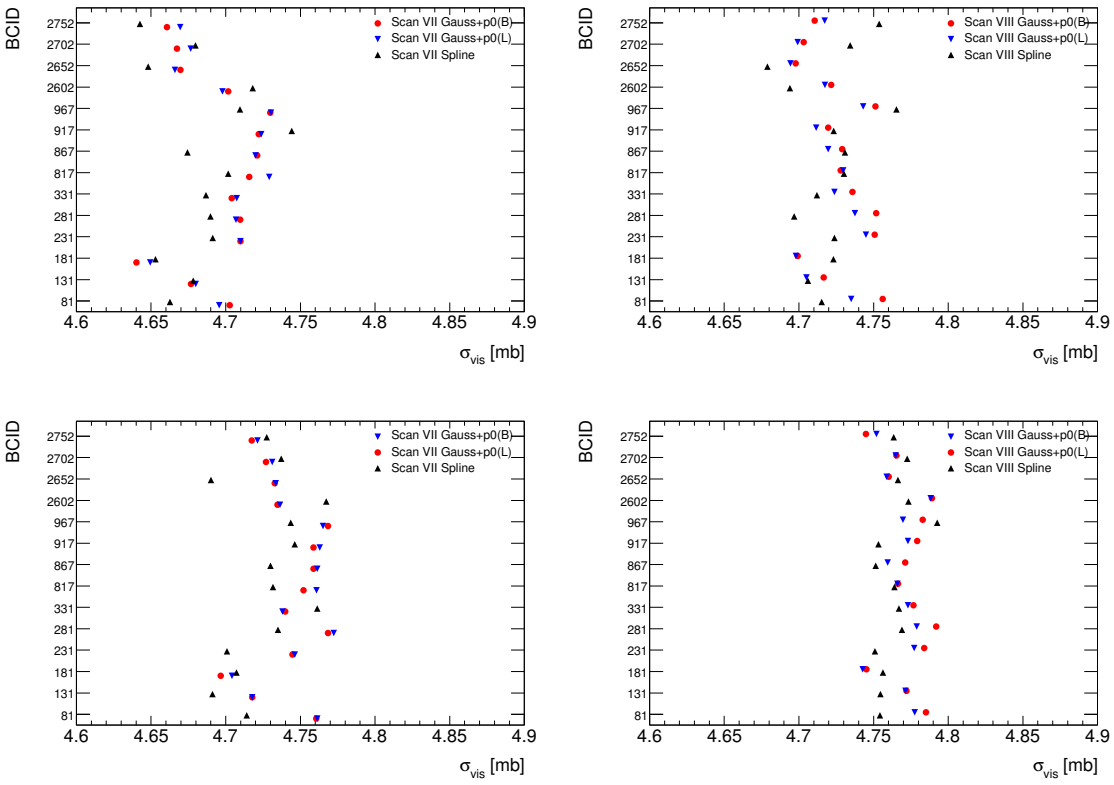

Figure 7.18 Results of $\sigma_{\text{vis}}^{\text{OR}}$ using three different fit models for scan VII (right) and scan VIII (left). The top plots shows results from the horizontal modules, the bottom ones from the vertical modules.

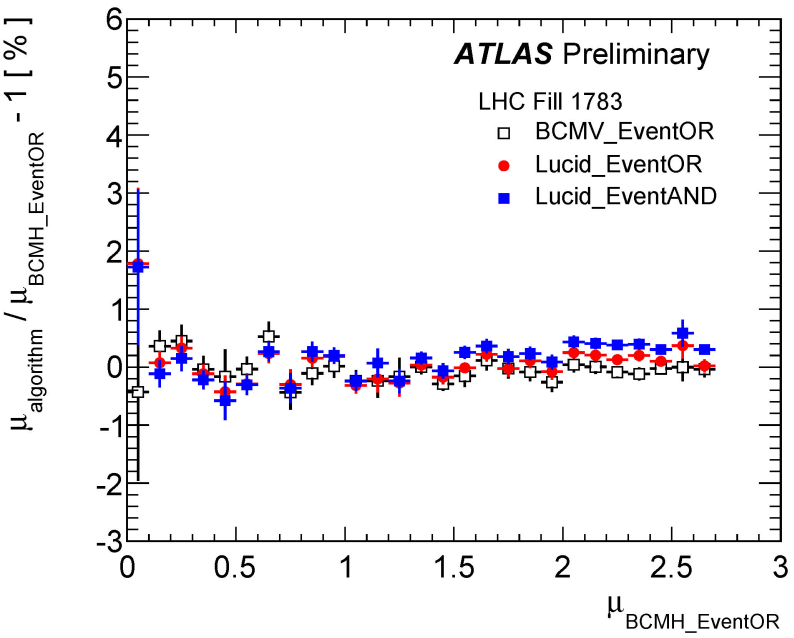

Figure 7.19 Relative deviation in the value of μ with respect to BCM-H Event-OR obtained with BCM-V Event-OR, LUCID Event-OR and LUCID Event-AND as a function of the μ value measured with BCM-H Event-OR during the May *vdM* scan [83].

The difference in $\sigma_{\text{vis}}^{\text{OR}}$ extracted from non-background subtracted data, fitted with single-Gauss+$p0$(B), i.e. $p0$ interpreted as background, versus results from background subtracted data fitted with single-Gauss+$p0(\mathscr{L})$, i.e. $p0$ interpreted as luminosity, is 0.3% at maximum and is taken as a relative uncertainty on the background subtraction.

7.5.8 Transverse Correlation

The analysis of measured transverse displacements of the luminous region during the scans from reconstructed event vertex data provides a 0.1% upper limit on the associated systematic uncertainty due to linear $x-y$ coupling.

Non-linear terms can appear due to a second-Gaussian component, which is now known to be barely present in the May scan-shapes. However, a generalized double-Gaussian fit on the LUCID Event-OR data, performed simultaneously to both planes results in a maximum deviation of 0.5%. This can be taken as a systematic uncertainty due to possible non-linear correlations [48].

7.5.9 μ Dependence within the *vdM* Scan

During scans VII and VIII the number of interactions per bunch crossing was in range of about $0 < \mu < 2.6$. Figure 7.19 shows the relative deviation of μ to BCM-H Event-

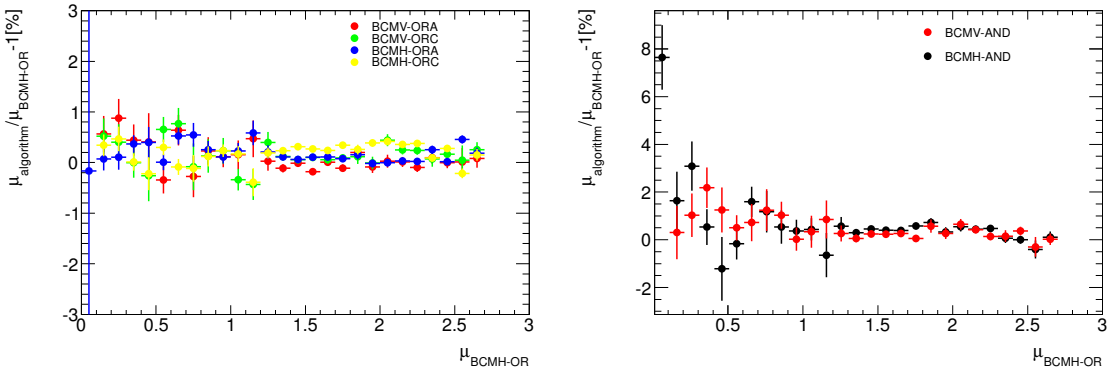

Figure 7.20 Relative deviation in the value of μ with respect to BCM-H Event-OR obtained with the single-sided Event-OR algorithms (left) and the Event-AND algorithms (right) as a function of the μ value measured with BCM-H Event-OR during the May *vdM* scan.

OR obtained with BCM-V Event-OR , LUCID Event-OR and LUCID Event-AND as a function of the μ value measured with BCM-H Event-OR during the May *vdM* scan. They agree to a level of 0.5% along the full scan-range. This value is taken as the statistical uncertainty on the μ dependence within the *vdM* scan. As a further comparison Figure 7.20 shows the same μ-dependence to BCM-H Event-OR , for all BCM algorithms that have been previously analyzed in this chapter. The left plot shows the relative deviation of the single sided OR-algorithms, namely Event-ORA Event-ORC . The right hand plot shows the agreement of the Event-AND algorithm, of BCM-H and BCM-V , respectively. They agree to about 0.5% for higher values of μ and for Event-AND about 2% for lower values, where low statistics become an issue. The large deviation of the first scan-point might, however, indicate that there is a background contribution in Event-AND in this fill, which was not corrected for (similar observations at large separation will be discussed later).

7.5.10 Beam-Beam effects

In [2] the uncertainty on σ_{vis} due to beam-beam effects was estimated to be about 0.5%, if one assumes head-on collisions in IP1 and IP5 only. Simulations have shown that effect gets slightly smaller if the $1.4\sigma_b$ offset collisions at all other IPs are included, because in this case the change on the β functions in x and y compensate. However, presently 0.5% is used as a conservative estimate.

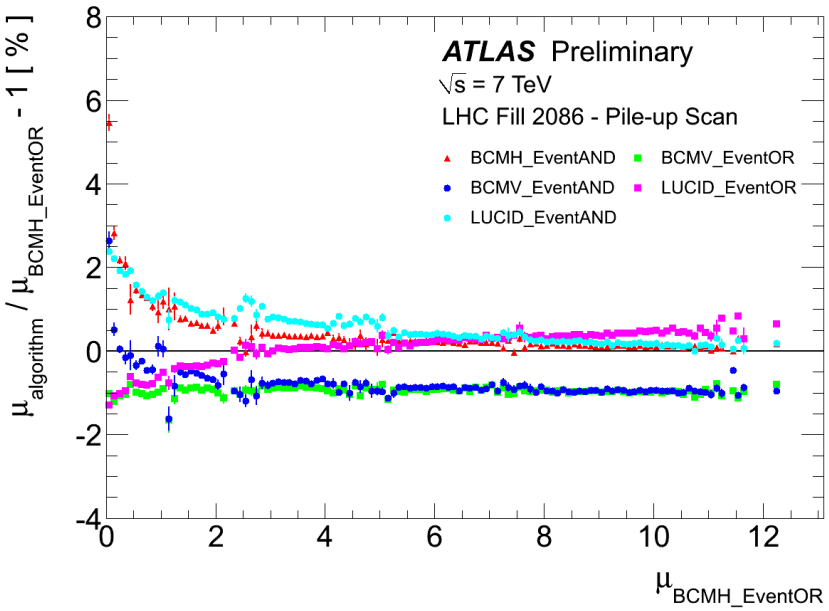

Figure 7.21 Relative deviation in the value of μ with respect to BCM-H Event-OR , obtained using different luminosity detectors plotted as a function of μ measured with BCM-H during the pile-up scan in September 2011. The high-μ values correspond to the beams colliding head-on, while the lowest mu values correspond to the beams being almost totally separated in the transverse plane [83].

7.6 Long Term Stability and μ Dependence

The 2011 running had a wide range of μ up to values of 35. It is therefore crucial to test the stability of the extracted calibrations for a large number of 2011 *pp* fills.
In order to decouple effects due to detector stability in time, from those explicitly related to the μ dependence itself, a dedicated analysis has been performed. Within a regular physics fill with 1024 colliding bunches and a peak μ of $\approx$12, both beams were *scanned* across each other in order to perform a so called μ or *pile-up* scan. In this way it was possible to take data within one fill for a range of $0.02 < \mu < 12$.
Due to the high number of bunches in the fill the afterglow contribution was also rising to about 0.1% in Event-OR . The fill had a large number of unpaired bunches, with rather high intensity. It was already discussed that beam-gas is independent of the beam separation. Therefore the strongest contribution within this scan, relative to the signal, is at low μ. It was found to be about 10% for Event-OR at $\mu < 0.5$. Compared to the *vdM* scan, this filling scheme also increases background forming a coincidence event, i.e. hits on both detector sides. Therefore also the Event-AND rates need to be background corrected. Figure 7.21 shows a comparison of the relative deviation of the per-bunch μ relative to BCM-H Event-OR for various detectors and algorithms in this scan. For $\mu > 2$, which is the range that is relevant for most 2011 physics analysis, all

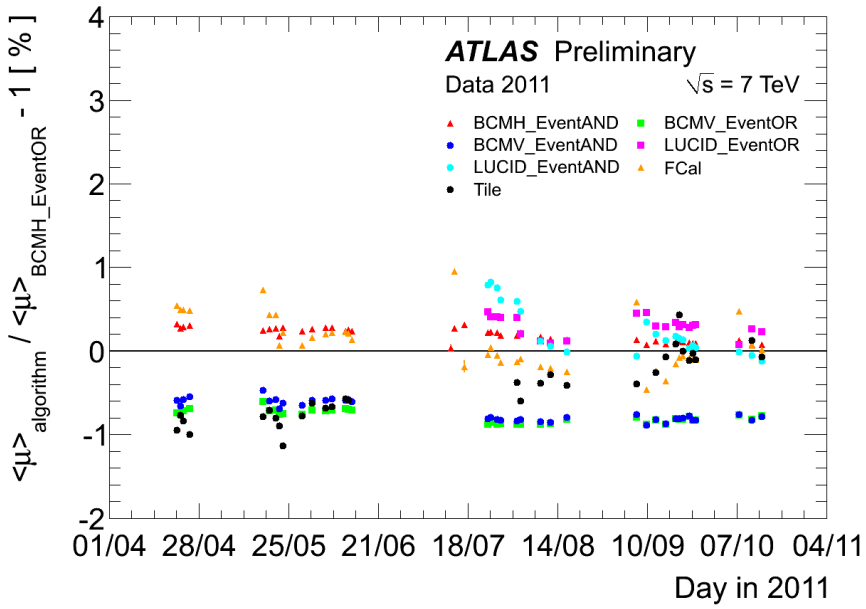

Figure 7.22 Long term stability: Relative deviation in the BCID-average μ with respect to BCM-H Event-OR obtained using different luminosity detectors, as a function of the day. Each point shows the deviation for a single ATLAS run, averaged over all colliding bunches and over the duration of that run [83].

algorithms agree within 1%. This value is taken as an additional uncertainty due a μ-dependence for the 2011 physics data. At lower μ the algorithms deviate significantly. Especially the Event-AND algorithms deviate by up to 2%. This is presumably due to a wrong background estimation for Event-AND , which is presently under study. Namely the combinatorics for the Event-AND background subtraction turned out to be very delicate and some intrinsic AND background component is observed, that is presently not understood.

As a test of long term stability Figure 7.22 shows the fractional deviation in μ with respect to BCM-H Event-OR obtained using different luminosity detectors averaged over many physics runs in 2011. All algorithms are consistent within $\pm 1\%$ during the time span of about six months. The 0.7% deviation between BCM-H and BCM-V is stable over this time. Even though the deviations are not independent of the μ-dependence, explained previously, the 1% deviation is conservatively taken as an additional systematic uncertainty.

7.6.1 BCM H/V Discrepancy

While BCM-H and BCM-V yield an excellent agreement during the *vdM* scans themselves (see Figure 7.20), this is not the case for fills after the scan. As mentioned in the previous section a constant deviation of 0.7% is visible over the runs in 2011. The

source of the discrepancy is not fully understood. It is assumed to be instrumental, caused by an effect called *diamond pumping*. This phenomenon is commonly observed in diamond-detectors and is believed to be caused by a gradual filling of charge traps, after the material is exposed to radiation. This can lead to a change in efficiency (where the change saturates at certain level, and can be reversed by UV light). More details on this can be found e.g. in [84]. As the strength of this effect depends on the level of impurities in the diamond sensors, BCM-H and BCM-V might be affected differently. However, so far this is just an assumption. It can therefore not be excluded that the source is some unknown uncertainty in the *vdM* calibration itself. Therefore the deviation of 0.7% must be taken as an additional systematic uncertainty on the calibration.

7.6.2 Total Uncertainty of the Results

Scan Number	VII–VIII
Fill Number	1783
Source	Relative Uncertainty
Bunch Charge Product	0.54%
Beam Centering	0.1%
Emittance Growth	
and other non-Reproducibility	0.7%
Beam-Position Jitter	0.3%
Bunch-to-Bunch σ_{vis} Consistency	0.6%
Fit Model	0.5%
Length Scale Calibration	0.3%
Absolute ID Length Scale	0.3%
Background Subtraction	0.3%
Transverse Correlations	0.5%
μ Dependence within Scan	0.5%
BCM-H to BCM-V Consistency	0.7%
Beam-Beam Effects	0.5%
Total Calibration Uncertainty	1.67%

Table 7.8 Individual relative systematic uncertainties on the determination of the visible cross-section $\sigma_{\text{vis}}^{\text{OR}}$. For the total uncertainty the individual values are added in quadrature.

Before the May 2011 scan, LUCID was the preferred luminosity detector of ATLAS. However, several operational issues appeared, in particular with increasing μ

Scan Number	VII–VIII
Fill Number	1783
Source	Relative Uncertainty
Long Term Stability	1.0%
μ-Dependence	1.0%
Afterglow	0.2%
Total, Luminosity Monitoring	1.43%
Total, Luminosity Calibration Uncertainty	1.67%
Total, Luminosity Uncertainty	2.2%

Table 7.9 Relative systematic uncertainties on the luminosity.

migration effects became an issue, and the LUCID Event-OR measurements started to saturate. Due to its very stable performance, as demonstrated in this thesis, the BCM detector therefore was chosen by the ATLAS luminosity community to be the preferred ATLAS luminosity detector, replacing LUCID.

Since May 2011, the ALTAS preferred online algorithm, whose results are sent to the LHC, is BCM-H Event-AND . Its online luminosity measurement is already almost background free, without any offline background-subtraction needed. The official luminosity, that is used for physics analysis, was chosen to be that of BCM-H Event-OR , because of its high statistics and because it its calibration is believed to be best understood.

In Table 7.9 a summary of all systematic uncertainties is given. The final uncertainty on its calibration constant $\sigma_{\text{vis}}^{\text{OR}}$ is taken as the quadratic sum over all individual components and is estimated to be 2.2%. In comparison with the October scans (IV and V), the total uncertainty has been reduced significantly mainly, due to the large improvement on the bunch charge uncertainty. However, as a consequence other uncertainties affecting the *vdM* calibration became more relevant. Additionally it was found that new uncertainties had to be added, such as ones due to beam-background and beam-beam effects. The total uncertainty affecting the ATLAS luminosity on data taken in 2011 can be estimated by the quadratic sum of the total uncertainty on $\sigma_{\text{vis}}^{\text{OR}}$ and the total uncertainty observed in luminosity monitoring. Where the latter is comprised of the μ-dependence and the uncertainty on afterglow correction observed in the 2011 data. The latter needs to be added, because the current standard method in ATLAS to correct luminosity data for afterglow is to correct for the μ value in the empty BCID preceding a collision. However, the afterglow rate drops with an exponential behavior. For this reason the preceding bunch overestimates the afterglow by up to a factor 2% and an additional uncertainty of 0.2% has been estimated [48]. The values are summarized in

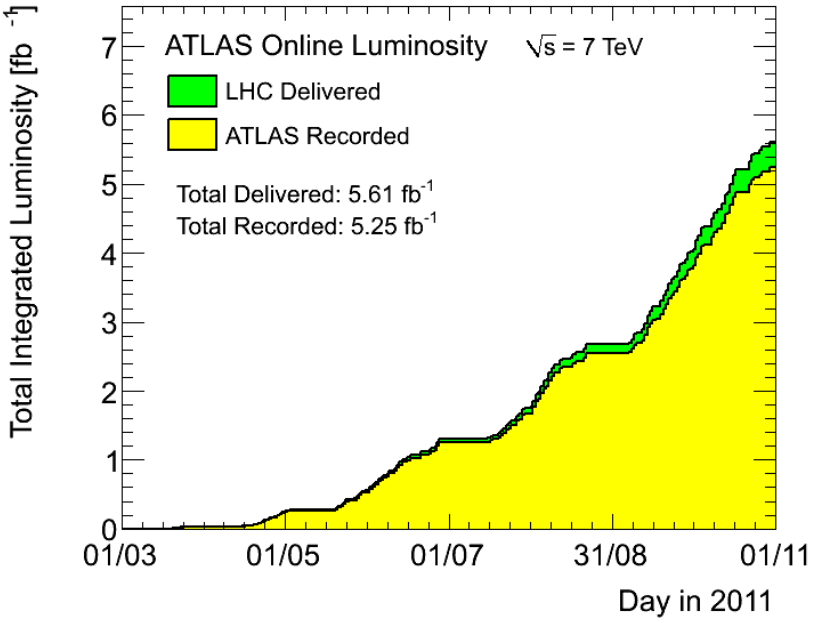

Figure 7.23 Cumulative luminosity versus day delivered to (green), and recorded by ATLAS (yellow) during stable beams for *pp* collisions at 7 TeV center-of-mass energy in 2011. The delivered luminosity accounts for the luminosity delivered from the start of stable beams until the LHC requests ATLAS to turn the sensitive detector off to allow a beam dump or beam studies. Given is the luminosity as determined with BCM-H Event-OR [62].

Table 7.9 and result in a final error on the luminosity of 2.2%.

The cumulative luminosity versus day within the 2011 running, as determined by BCM-H Event-OR , is shown on Figure 7.23 and the total peak luminosity per day in Figure 7.24. In 2011 and a maximum peak luminosity of $3.65\times10^{33}\,\mathrm{cm^2s^{-1}}$ was reached, and a total integrated luminosity of $5.61\,\mathrm{fb}^{-1}$ was delivered by the LHC to ATLAS, of which $5.25\,\mathrm{fb}^{-1}$ could be recorded by the ATLAS experiment.

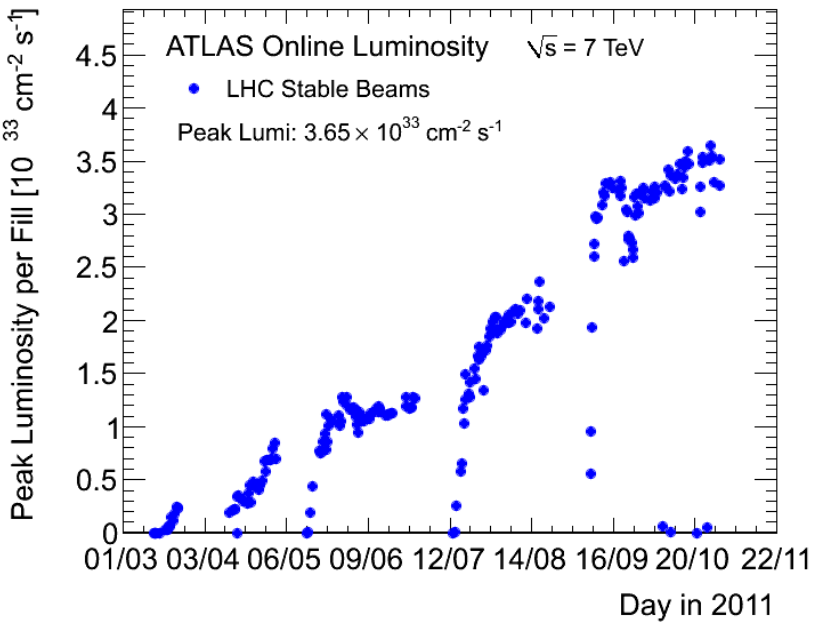

Figure 7.24 The maximum instantaneous luminosity versus day delivered to ATLAS, measured with BCM-H Event-OR . Only the peak luminosity during stable beam periods is shown [62].

Chapter 8

Summary and Conclusion

At the ATLAS experiment so called *relative luminosity* monitors measure the inelastic *pp* rate primarily via different *event counting* algorithms. In order to control and understand the systematics that affect the luminosity, ATLAS uses a variety of different sub-detectors, which all differ in their acceptance and response to *pile-up*, i.e. multiple interactions within the same bunch crossing. Their relative measurements are calibrated by *absolute measurements* which is presently done using so-called van-der Meer (*vdM*) scans.

The strategy of *vdM* scans is to simultaneous measure the interaction rate and separate the beams at the IP in a number of steps in both horizontal, and vertical planes. By fitting the resulting scan curve, the convolved transverse beam sizes $\Sigma_{x,y}$ at the IP can be measured. Together with other beam parameters, such as the bunch current product, the absolute luminosity can be determined and a calibration constant σ_{vis} for each algorithm can be extracted. Once σ_{vis} is known for a certain algorithm, it is possible to translate the event counting rate into a luminosity value for physics use.

In this thesis, the calibration of the ATLAS Beam Condition Monitors (BCM) as a luminosity sub-detector using *vdM* scans has been presented. Two *vdM* scan sessions have been analyzed, the first one was performed in October 2010, the second one in May 2011. Each scan session consisted of two *vdM* scans in order to test the reproducibility of the results. The most important algorithms analyzed were Event-OR , which uses inclusive counting and benefits from large statistics, and Event-AND , which uses coincidence counting, has less statistics but a better suppression of beam background. In addition, the May scans were analyzed for data from two independent BCM readouts, BCM-H and BCM-V , respectively.

Each *vdM* scan had multiple colliding bunches which allowed a number of cross-checks to be made. As there are in general large variations in beam sizes and intensities within the bunches, σ_{vis} and the luminosity were determined for each colliding bunch separately. For the final results of the calibration constants, the error-weighted aver-

ages over all colliding bunches and both scans were taken.

In order to estimate the uncertainty affecting the calibration constant, a detailed study of all possible error sources has been carried out. Many uncertainties that were introduced by the experimental set-up, e.g. from the bunch-charge product or the length-scale calibration, were investigated in dedicated studies elsewhere. Others could be directly evaluated from the BCM data, in particular by comparing the results between the two subsequent scans and results from the individual colliding bunches. To give a final uncertainty on the luminosity measured by the BCM in 2010 and 2011, the results from several algorithms and different sub-detectors were in addition compared over the corresponding period of data taking.

The analysis of these scans revealed many surprises. Before the LHC start, the precision on the luminosity using *vdM* scans was not expected to be better than 5-10% [51, 12, 85]. Generally this method was quoted only as a preliminary solution for the early LHC running period, before the absolute luminosity measurements with the dedicated detectors TOTEM and ALFA are fully commissioned.

However, the result from the October 2010 scans were exceeding the expectations with a final uncertainty of 3.4% on the 48 pb^{-1} data recorded in 2010. At this time, LUCID was the preferred detector for relative luminosity measurements and BCM was one detector amongst others to provide cross-checks.

Because of several hardware changes done on the luminosity sub-detectors in early 2011, it was decided to perform a new set of *vdM* scans. The general opinion was that it will be difficult to maintain the 3.4% for the running conditions of 2011, because of larger pile-up and a reduced bunch-spacing from 150 ns to 50 ns.

The *vdM* -scans performed in May 2011, however, managed to outrage this result again, and presently an uncertainty of 2.2% is estimated on the 5.6 fb^{-1} recorded in 2011. This is mainly thanks to a reduction of the bunch current product uncertainty from 3.1% to 0.54% [80].

The more challenging running conditions in 2011 also revealed the excellent performance of the BCM as a luminosity sub-detector. The Beam Condition Monitor, that was mainly designed to detect early signs of beam instabilities and provide only complementary luminosity measurements as a by-product, became the ATLAS preferred luminosity sub-detector in May 2011, and is providing up to now the official online- and offline- luminosity for ATLAS.

Bibliography

[1] ATLAS Collaboration, *Luminosity Determination in pp Collisions at $\sqrt{(s)}$=7 TeV Using the ATLAS Detector at the LHC*, Eur. Phys. J. **C71** (2011) 1630, arXiv:1101.2185 [hep-ex].

[2] ATLAS Collaboration, *Improved Luminosity Determination in pp Collisions at $\sqrt{(s)}$=7 TeV using the ATLAS Detector*, ATLAS-COM-CONF-2012-086, 2012.

[3] M. Mangano, *LHC Lumi Days 2011: Motivations and Precision Targets for an Accurate Luminosity Determination at the LHC*, CERN-Proceedings-2011-001, 2011.

[4] E. Wilson, *An Introduction to Particle Accelerators*. Oxford University Press, 2001.

[5] B. de Raad, A. Minten, and E. Keil, *Lectures on beam optics*. CERN, 1966.

[6] S. M. White, *Determination of the Absolute Luminosity at the LHC*. PhD thesis, Orsay, Universite Paris-Sud 11, Orsay, 2010. oai:cds.cern.ch:1308187.

[7] W. Herr and B. Muratori, *Concept of Luminosity*, CERN 2006-002, 2006.

[8] C. Moller and K. Danske, *Vidensk. Selsk. Mat.-Fys.Medd.*, **23,1** (1945) .

[9] D. E. Groom et al., *Review of Particle Physics*. The European Physical Journal, 2010. http://pdg.lbl.gov.

[10] W. Herr, *Beam-Beam Interactions*, CERN 2006-002, 2006.

[11] W. Herr, *LHC Lumi Days 2012: Beam-beam and dynamic beta*, 2012.

[12] H. Burkhardt and P. Grafstrom, *Absolute Luminosity from Machine Parameters*, LHC-PROJECT-Report-1019, 2007.

[13] R. Baartman, *Beam-Beam Effect and LHC Luminosity Limit*, July, 2011.

[14] S. Jadach, *Theoretical error of luminosity cross-section at LEP*, arXiv:hep-ph/0306083 [hep-ph].

[15] V. Papadimitriou, *Luminosity measurements at hadron colliders*, FERMILAB-CONF-08-106-E, 2008.

[16] A. Martin and others., *Parton distributions for the LHC*, Eur.Phys.J. **C63** (2009) 189–285, arXiv:0901.0002 [hep-ph].

[17] S. Alekhin et al., *The PDF4LHC Working Group Interim Report*, arXiv:1101.0536 [hep-ph].

[18] V. Khoze, *LHC Lumi Days 2011: Indirect luminosity measurements: theoretical assessment. Selected topics on the precision of luminometry at the LHC*, CERN-Proceedings-2011-001, 2011.

[19] G. Latino, *The TOTEM Experiment at the LHC*, arXiv:0905.2936, May, 2009.

[20] S. Jakobsen, *Calibration, testing, commissioning and first data of ALFA at LHC*, ATL-LUM-PROC-2011-002, Sep, 2011.

[21] M. V. Lokajicek and V. Kundrat, *Optical theorem and elastic nucleon scattering*, arXiv:0906.3961 [hep-ph].

[22] V. Papadimitriou, *LHC Lumi Days 2011: Luminosity determination at the Tevatron*, CERN-Proceedings-2011-001, Jun, 2011.

[23] R. Schmidt and W. Herr, *LHC Lumi Days 2011: Experience at CERN with Luminosity Monitoring and Calibration*, CERN-Proceedings-2011-001, 2011.

[24] LHCb Collaboration, *LHCb : Technical Proposal*. No. CERN-LHCC-98-004 in LHC Tech. Proposal. CERN, Geneva, 1998.

[25] P. Hopchev, *The beam-gas method for luminosity measurement at LHCb*, arXiv:1005.4398 [physics.ins-det].

[26] L. R. Evans and P. Bryant, *LHC Machine*, vol. 3. CERN, 2008.

[27] M. Lamont, *Status of the Large Hadron Collider*, Journal of Physics: Conference Series **347** (2012) no. 1, 012001. http://stacks.iop.org/1742-6596/347/i=1/a=012001.

[28] C. Carli, *Proceedings of the LHC Performance Workshop 2011 (Chamonix 2011)*, 2011.

[29] C. Carli, *Proceedings of the LHC Performance Workshop 2012 (Chamonix 2012)*, .

[30] ATLAS Collaboration, *ATLAS: technical proposal*. No. CERN-LHCC-94-43 in LHC Tech. Proposal. CERN, Geneva, 1994.

[31] CMS Collaboration, *CMS: Technical proposal*. No. CERN-LHCC-94-38 in LHC Tech. Proposal. CERN, Geneva, 1994.

[32] W. Kienzle et al., *TOTEM, Total Cross Section, Elastic Scattering and Diffraction Dissociation at the LHC: Technical Proposal*, CERN-LHCC-99-007. LHCC-P-5, Mar, 1999.

[33] ALICE Collaboration, *ALICE: Technical proposal for a Large Ion collider Experiment at the CERN LHC*. No. CERN-LHCC-95-71. CERN, Geneva, 1995.

[34] http://press.web.cern.ch/press/pressreleases/releases2011/PR01.11E.html.

[35] C. Lefevre, *The CERN accelerator complex*, Dec, 2008.

[36] R. Bailey and P. Collier, *Standard Filling Schemes for Various LHC Operation Modes*, LHC-PROJECT-NOTE-323, Sep, 2003.

[37] *Non-collision backgrounds as measured by the ATLAS detector during the 2010 proton-proton run*, ATLAS-CONF-2011-137, 2011.

[38] G. Papotti, *Chamonix 2011 Workshop on LHC Performance: Luminosity analysis*, CERN-ATS-2011-005, 2011.

[39] R. Jones, *First Results from the LHC Beam Instrumentation Systems*, LHC-Performance-Note-006, Jan, 2009.

[40] E. Bravin, G. Burtin, A. Fisher, A. Guerrero, A. Jeff, T. Lefevre, A. Goldblatt, and F. Roncarolo, *First Beam Measurements with the LHC Synchrotron Light Monitors*, CERN-BE-2010-019, May, 2010.

[41] S. Burger et al., *First Results of the LHC Collision Rate Monitors*, CERN-BE-2011-017, May, 2011.

[42] http://lpc.web.cern.ch/lpc/bcnwg.htm.

[43] P. Odier, M. Ludwig, and S. Thoulet, *The DCCT for the LHC Beam Intensity Measurement*, CERN-BE-2009-019, May, 2009.

[44] D. Belohrad et al., *Implementation of the Electronics Chain for the Bunch by Bunch Intensity Measurement Devices for the LHC*, CERN-BE-2009-018, May, 2009.

[45] G. Anders et al., *LHC Bunch Current Normalisation for the April-May 2010 Luminosity Calibration Measurements*, CERN-ATS-Note-2011-004 PERF, Feb, 2011.

[46] A. Jeff, *LHC Lumi Days 2012: Ghost and satellites measured with the LHC LDM*, 2012.

[47] T. Pauly, *LHC Lumi Days 2011: Bunch Current Normalisation Analysis Results. BCTs and BPTX analysis results*, CERN-Proceedings-2011-001, 2011.

[48] ATLAS Collaboration, *Luminosity Determination in pp Collisions at* $\sqrt{(}s)$*=7 TeV using the ATLAS Detector in 2011*, ATLAS-CONF-2011-116, Aug, 2011.

[49] R. Spiwoks et al., *The ATLAS Level-1 Central Trigger Processor (CTP)*, ATL-DAQ-CONF-2005-030, 2005.

[50] T. Pauly, *The ATLAS Level-1 Central Trigger System in Operation*, ATL-DAQ-PROC-2009-012, May, 2009.

[51] S. Ask, D. Malon, T. Pauly, and M. Shapiro, *Report from the Luminosity Task Force*, ATL-GEN-PUB-2006-002, Jul, 2006.

[52] C. Ohm and T. Pauly, *The ATLAS beam pick-up based timing system*, arXiv:0905.3648, May, 2009.

[53] H. Pernegger, *First test results of a high-speed beam conditions monitor for the ATLAS experiment*, .

[54] I. Dolenc et al., *ATLAS diamond BCM. ATLAS Diamond Beam Conditions Monitor*, PoS **VERTEX 2008** (2008) .

[55] A. Gorisek, *The ATLAS Beam Condition Monitor Commissioning*, oai:cds.cern.ch:1108885, 2008.

[56] B. Macek, *Performance of the ATLAS Beam Diagnostic Systems*, ATL-INDET-PROC-2010-045, Dec, 2010.

[57] A. Sbrizzi, *A Cherenkov Detector for Monitoring ATLAS Luminosity*, ATL-LUM-PROC-2010-004, Sep, 2010.

[58] P. Jenni, M. Nessi, and M. Nordberg, *Zero Degree Calorimeters for ATLAS*, LHCC-I-016. CERN-LHCC-2007-001, Jan, 2007.

[59] S. Arfaoui, M. Monnier, and L. Hervas, *Cross-calibration of the 2011 LUCID and BCM luminosity with the ATLAS forward calorimeter*, ATL-COM-LARG-2011-012, Jul, 2011.

[60] S. Maettig, *The Online Luminosity Calculator of ATLAS*, ATL-DAQ-PROC-2011-009, Jan, 2011.

[61] S. Kolos, E. Alexandrov, E. Feng, R. Hauser, A. Yakovlev, and A. Zaytsev, *Online remote monitoring facilities for the ATLAS experiment*, ATL-DAQ-PROC-2011-002, Jan, 2011.

[62] https://atlas.web.cern.ch/Atlas/GROUPS/DATAPREPARATION/DataSummary/2012/.

[63] http://op-webtools.web.cern.ch/op-webtools/vistar/vistars.php?usr=LHC3.

[64] S. van der Meer, *Calibration of the effective beam height in the ISR*, CERN-ISR-PO-68-31, 1968.

[65] Kjell and Johnsen, *The CERN intersecting storage rings*, Nuclear Instruments and Methods **108** (1973) no. 2, 205 – 223. http://www.sciencedirect.com/science/article/pii/0029554X73905922.

[66] H. V. and A. Sbrizzi, *Derivation of the Luminosity Algorithms*, Oct, 2010.

[67] ATLAS Collaboration, *Updated Luminosity Determination in pp Collisions at $\sqrt{(s)}$=7 TeV using the ATLAS Detector*, ATLAS-CONF-2011-011, Mar, 2011.

[68] J. LHC Lumi Days 2011: Panman, *Direct Luminosity Measurements at the LHC - Summary. Status summary and wishes from the experiments*, CERN-Proceedings-2011-001, 2011.

[69] W. Kozanecki, *LHC Lumi Days 2012: Beam-beam and dynamic beta*, 2012.

[70] D. Berge, A. Hoecker, A. Messina, and G. piacquadio, *Determination of the absolute luminosity and the visible cross section from LHC van der Meer scans using events with MBTS triggers and with primary vertices*, ATL-COM-LUM-2010-023, Jun, 2010.

[71] ATLAS Collaboration, *Characterization of Interaction-Point Beam Parameters Using the pp Event-Vertex Distribution Reconstructed in the ATLAS Detector at the LHC*, ATLAS-CONF-2010-027, May, 2010.

[72] D. Berge et al., *Generalization of the van der Meer luminosity calibration method to two dimensions*, ATL-COM-LUM-2011-001, Jan, 2011.

[73] J. Heinrich, *Coverage of Error Bars for Poisson Data*, CDF/MEMO/Statistics/Public/6438, 2003.

[74] M. Huhtinen, *Private Communication*.

[75] K. Schindl, *The injector chain for the LHC*, CERN-PS-99-18-DI, 1999.

[76] http://atlas-runquery.cern.ch.

[77] M. Tibbetts, *Visible Cross-Section Measurements and Evaluation of Systematic Uncertainties from Beam Profile Modelling using LUCID Data taken during the 7TeV ATLAS Beam Separation Scans in May 2011*, ATL-COM-LUM-2011-015, Jul, 2011.

[78] M. Huhtinen, *ATLAS LMTF meeting*. Nov., 2011. https://indico.cern.ch/conferenceDisplay.py?confId=157844.

[79] V. Hedberg, *ATLAS LMTF meeting*. Feb., 2012. https://indico.cern.ch/conferenceDisplay.py?confId=171273.

[80] G. Anders et al., *Study of the Relative LHC Bunch Populations for Luminosity Calibration*, CERN-ATS-Note-2012-028 PERF, Feb, 2012.

[81] A. Alici, *Study of the LHC Ghost Charge and Satellite Bunches for Luminosity Calibration*, CERN-ATS-Note-2012-029 PERF, Feb, 2012.

[82] K. Shaw, *Length Scale Calibration during the May 2011 scans using the ATLAS Detector*, ATL-COM-LUM-2011-016, Jul, 2011.

[83] https://twiki.cern.ch/twiki/bin/view/AtlasPublic/LuminosityPublicResults.

[84] R. J. Tapper, *Diamond detectors in particle physics*, 2000.

[85] F. Gianotti and M. Pepe-Altarelli, *Precision physics at the LHC*, Nucl.Phys.Proc.Suppl. **89** (2000) 177–189, arXiv:hep-ex/0006016 [hep-ex].

Appendix A

Abbreviations and Definitions

LHC/ATLAS INSTRUMENTATION

- *OLC:* Online Luminosity Calculator, software that handles all data relevant to the ATLAS online luminosity.
- *LB:* Luminosity Block, time unit of ATLAS.
- *PLB:* Pseudo-Luminosity Block, time unit that is synchronized to the beam-movements in a *vdM* scan.
- `COOL` : Conditions Database, permanent storage of the ATLAS relevant data.
- *BCM-H(V):* Horizontal- (Vertical-) Beam Condition Monitor Modules.
- *LUCID:* Cerenkov relative- luminosity detector of ATLAS.
- *BPTX:* Beam Pick-ups, used in ATLAS for general monitoring of the bunches and for relative intensity measurements per BCID.
- *FBCT:* Fast Beam Current Transformers, used for intensity measurements per BCID.
- *DCCT:* DC Current Transformers, they give an accurate absolute measurement of the total circulating intensity in each ring.

EXPRESSIONS USED IN LUMINOSITY DETERMINATION

- *pile-up*: Multiple interaction per bunch crossing.
- $\mathscr{L}$: Instantaneous luminosity.
- L: Integrated luminosity.
- θ_C: Full Crossing Angle at IP1.

- β: Optical β-function describing the particle trajectory. Determined by the accelerator magnet configuration and powering.
- β^*: Value of the optical β-function at the IP. At the IP the beam is "squeezed" in order th reach higher luminosity.
- ε: Transverse emittance given by 2.5. A low emittance particle beam is a beam where the particles are confined to a small distance and have nearly the same momentum.
- f_r: LHC revolution frequency 11.245 kHz.
- $n_{1(2)}$: Number of particles per bunch in beam 1(2).
- n_b: Number of colliding bunches in the ring.
- $\Sigma_{x,y}$: Transverse convolved beam size in horizontal (x) or vertical (y) direction.
- $\mu_{\text{vis,sp}}^{\text{MAX}}$: Maximum $\mu_{\text{vis,sp}}$, as determined by a fit to the scan-curves.
- σ_{vis}: Visible cross section of a given detector-algorithm, can be interpreted as its calibration constant.
- μ: Average number of *pp*-collisions per bunch-crossing.
- Indices:
  - vis: *visible value*, one that is multiplied with the detector efficiency, e.g. $\mu_{\text{vis}} = \varepsilon \cdot \mu$.
  - spec: *specific value*, one that is corrected for bunch-current product, e.g. $\mu_{\text{sp}} = \mu/(\text{n}_1\text{n}_2)$.

Appendix B

vdM Scans I–III

	vdM Scan I (April 26, 2010)	vdM Scan II, III (May 9, 2010)
LHC Fill Number	1059	1089
Scan Directions	1 horizontal scan followed by 1 vertical scan	2 horizontal scans followed by 2 vertical scans
Total Scan Steps per Plane	27 ($\pm 6\sigma_b$)	27 ($\pm 6\sigma_b$)
Scan Duration per Step	30 s	30 s
Number of Bunches Colliding in ATLAS & CMS	1	1
Total Number of Bunches per Beam	2	2
Number of Protons per Bunch	$\sim 0.1 \cdot 10^{11}$	$\sim 0.2 \cdot 10^{11}$
β-function at IP [$\beta^\star$] (m)	~ 2	~ 2
Transverse Single Beam Size σ_b (μm)	~ 45	~ 45
Crossing Angle (μrad)	0	0
Typical Luminosity/Bunch ($\mu \mathrm{b}^{-1}/s$)	$4.5 \cdot 10^{-3}$	$1.8 \cdot 10^{-2}$
μ	0.03	0.11

Table B.1 Summary of the main characteristics of the first three *vdM* scans performed at the ATLAS IP.

Appendix C

October 2010 *vdM* scan

C.1 Fit Parameters

BCID	Scan	$\Sigma_x[\mu m]$	$\mu_{\text{vis,sp}}^{\text{MAX}}[(10^{22}p)^{-2}]$	$Cov_{\Sigma_x-\mu_{\text{vis,sp}}^{\text{MAX}}}$	$X_0[\mu m]$	p0$[10^{-4}(10^{22}p)^{-2}]$	χ^2/Ndf
1	IV	81 ± 0.31	0.11 ± 0.00057	-0.73	-5.2 ± 0.28	0.11 ± 0.19	1.4
	V	81 ± 0.31	0.11 ± 0.00051	-0.76	-2.7 ± 0.25	0.18 ± 0.16	1
501	IV	80 ± 0.33	0.11 ± 0.00061	-0.75	-4.3 ± 0.28	0.12 ± 0.17	1
	V	80 ± 0.3	0.11 ± 0.00054	-0.76	-2.3 ± 0.24	0.26 ± 0.14	1.3
862	IV	81 ± 0.31	0.11 ± 0.00053	-0.72	-4.2 ± 0.26	0.25 ± 0.28	1.1
	V	80 ± 0.29	0.11 ± 0.00051	-0.79	-2.5 ± 0.22	0.17 ± 0.088	1
1451	IV	79 ± 0.32	0.12 ± 0.00062	-0.78	-4.8 ± 0.26	0.12 ± 0.15	0.99
	V	79 ± 0.33	0.12 ± 0.00058	-0.82	-2.5 ± 0.23	0.2 ± 0.093	0.89
1651	IV	81 ± 0.34	0.11 ± 0.00062	-0.79	-4.8 ± 0.27	$2.9e-11\pm0.081$	1.4
	V	81 ± 0.46	0.11 ± 0.00072	-0.89	-2.5 ± 0.24	0.22 ± 0.098	0.81
2301	IV	79 ± 0.34	0.12 ± 0.00064	-0.79	-4.9 ± 0.26	0.15 ± 0.13	0.43
	V	80 ± 0.3	0.11 ± 0.00054	-0.79	-2.4 ± 0.23	0.17 ± 0.095	1.4

Table C.1 Fit parameters obtained from BCM-H in the horizontal scans IV and V to Event-OR .

BCID	Scan	$\Sigma_y[\mu m]$	$\mu_{\text{vis,sp}}^{\text{MAX}}[(10^{22}p)^{-2}]$	$Cov_{\Sigma_y-\mu_{\text{vis,sp}}^{\text{MAX}}}$	$Y_0[\mu m]$	p0$[10^{-4}(10^{22}p)^{-2}]$	χ^2/Ndf
1	IV	83 ± 0.37	0.11 ± 0.00061	-0.78	0.62 ± 0.29	0.14 ± 0.19	0.74
	V	84 ± 0.36	0.11 ± 0.00055	-0.8	0.34 ± 0.25	0.48 ± 0.22	0.85
501	IV	81 ± 0.37	0.11 ± 0.00064	-0.79	1.3 ± 0.28	0.12 ± 0.18	1.1
	V	82 ± 0.34	0.11 ± 0.00056	-0.78	0.53 ± 0.25	0.43 ± 0.22	0.87
862	IV	83 ± 0.35	0.11 ± 0.00056	-0.77	0.81 ± 0.26	0.079 ± 0.22	0.67
	V	84 ± 0.32	0.11 ± 0.0005	-0.79	0.88 ± 0.23	0.36 ± 0.18	0.47
1451	IV	79 ± 0.33	0.12 ± 0.00062	-0.78	0.79 ± 0.26	0.38 ± 0.18	0.79
	V	79 ± 0.33	0.12 ± 0.00058	-0.82	0.55 ± 0.23	0.46 ± 0.16	1.4
1651	IV	80 ± 0.34	0.11 ± 0.00062	-0.79	0.82 ± 0.27	0.29 ± 0.16	1.2
	V	81 ± 0.3	0.11 ± 0.00052	-0.76	0.36 ± 0.24	0.52 ± 0.21	0.9
2301	IV	79 ± 0.31	0.12 ± 0.00059	-0.75	0.6 ± 0.26	0.085 ± 0.2	0.65
	V	80 ± 0.34	0.11 ± 0.00059	-0.82	0.33 ± 0.23	0.5 ± 0.16	0.65

Table C.2 Fit parameters obtained from BCM-H in the vertical scans IV and V to Event-OR .

BCID	Scan	$\Sigma_x[\mu m]$	$\mu_{\mathrm{vis,sp}}^{\mathrm{MAX}}[(10^{22}p)^{-2}]$	$Cov_{\Sigma_x-\mu_{\mathrm{vis,sp}}^{\mathrm{MAX}}}$	$X_0[\mu m]$	p0$[10^{-4}(10^{22}p)^{-2}]$	χ^2/Ndf
1	IV	81 ± 0.94	$0.0031\pm4.7e-05$	-0.54	-5.3 ± 1.2	$6.6e-14\pm0.012$	0.95
	V	81 ± 0.87	$0.003\pm4.1e-05$	-0.55	-1.2 ± 1.1	$6.1e-12\pm0.017$	0.89
501	IV	80 ± 0.99	$0.0032\pm5e-05$	-0.56	-5.2 ± 1.2	$2.2e-14\pm0.034$	0.98
	V	80 ± 0.85	$0.0032\pm4.2e-05$	-0.55	-2 ± 1.1	$7.7e-15\pm0.011$	1
862	IV	81 ± 0.86	$0.0031\pm4.2e-05$	-0.55	-3 ± 1.1	$1.8e-12\pm0.011$	0.56
	V	82 ± 0.74	$0.0031\pm3.6e-05$	-0.54	-1.8 ± 0.97	$9.8e-13\pm0.0051$	0.55
1451	IV	79 ± 0.93	$0.0033\pm4.6e-05$	-0.56	-4.1 ± 1.1	0.015 ± 0.024	0.66
	V	80 ± 0.78	$0.0033\pm3.9e-05$	-0.56	-2.9 ± 0.96	$6.6e-13\pm0.013$	0.76
1651	IV	81 ± 0.97	$0.0032\pm4.6e-05$	-0.55	-5.5 ± 1.2	0.012 ± 0.025	0.48
	V	80 ± 0.7	$0.0032\pm3.8e-05$	-0.51	-2.2 ± 1	$6.5e-16\pm0.0033$	1.7
2301	IV	80 ± 0.92	$0.0033\pm4.6e-05$	-0.56	-5.9 ± 1.1	0.005 ± 0.022	0.38
	V	80 ± 0.77	$0.0032\pm3.9e-05$	-0.55	-3.3 ± 0.98	$9.1e-13\pm0.017$	0.63

Table C.3 Fit parameters obtained from BCM-H in the horizontal scans IV and V to Event-AND .

BCID	Scan	$\Sigma_y[\mu m]$	$\mu_{\mathrm{vis,sp}}^{\mathrm{MAX}}[(10^{22}p)^{-2}]$	$Cov_{\Sigma_y-\mu_{\mathrm{vis,sp}}^{\mathrm{MAX}}}$	$Y_0[\mu m]$	p0$[10^{-4}(10^{22}p)^{-2}]$	χ^2/Ndf
1	IV	85 ± 1	$0.003\pm4.6e-05$	-0.55	1.2 ± 1.3	$7.2e-13\pm0.0099$	0.77
	V	84 ± 0.97	$0.0031\pm4.1e-05$	-0.62	0.34 ± 1.1	0.02 ± 0.025	0.83
501	IV	82 ± 1	$0.0032\pm4.9e-05$	-0.56	2.8 ± 1.2	$1.8e-13\pm0.25$	1.3
	V	82 ± 0.8	$0.0031\pm4.1e-05$	-0.48	-0.88 ± 1.1	$5.6e-13\pm0.0054$	2.6
862	IV	83 ± 0.89	$0.0031\pm4.1e-05$	-0.55	0.68 ± 1.1	$1.8e-13\pm0.015$	1.5
	V	85 ± 0.86	$0.003\pm3.5e-05$	-0.63	0.58 ± 1	0.0019 ± 0.066	0.95
1451	IV	79 ± 0.91	$0.0033\pm4.5e-05$	-0.56	1.8 ± 1.1	0.0052 ± 0.02	0.74
	V	80 ± 0.79	$0.0032\pm3.9e-05$	-0.55	1.6 ± 0.97	$1.8e-11\pm0.025$	0.88
1651	IV	81 ± 0.97	$0.0032\pm4.6e-05$	-0.57	0.93 ± 1.2	$4.5e-13\pm0.074$	0.91
	V	81 ± 0.84	$0.0031\pm3.9e-05$	-0.67	0.24 ± 1	$4.1e-14\pm0.0089$	1.2
2301	IV	80 ± 0.91	$0.0033\pm4.5e-05$	-0.56	1.2 ± 1.1	$1.7e-14\pm0.046$	0.64
	V	83 ± 0.83	$0.0032\pm3.8e-05$	-0.6	2.1 ± 1	$8.4e-13\pm0.021$	0.58

Table C.4 Fit parameters obtained from BCM-H in the vertical scans IV and V to Event-AND .

Appendix D

May 2011 *vdM* scan

D.1 Fit parameters

BCID	Scan	$\Sigma_x[\mu m]$	$\mu_{\mathrm{vis,sp}}^{\mathrm{MAX}}[(10^{22}p)^{-2}]$	$Cov_{\Sigma_x-\mu_{\mathrm{vis,sp}}^{\mathrm{MAX}}}$	$X_0[\mu m]$	p0$[10^{-4}(10^{22}p)^{-2}]$	χ^2/Ndf
81	VII	55.204 ± 0.093	0.239 ± 0.001	-0.594	-2.181 ± 0.124	0.922 ± 0.193	1.034
	VIII	55.859 ± 0.097	0.236 ± 0.001	-0.595	-0.014 ± 0.126	1.894 ± 0.239	1.648
131	VII	58.973 ± 0.093	0.218 ± 0.001	-0.581	-2.199 ± 0.122	0.042 ± 0.226	3.310
	VIII	59.710 ± 0.098	0.215 ± 0.001	-0.589	-0.194 ± 0.124	1.106 ± 0.260	1.752
181	VII	58.956 ± 0.095	0.214 ± 0.001	-0.580	-2.189 ± 0.127	-0.195 ± 0.207	3.019
	VIII	59.744 ± 0.100	0.212 ± 0.001	-0.581	-0.053 ± 0.129	0.608 ± 0.258	3.389
231	VII	56.812 ± 0.088	0.225 ± 0.001	-0.595	-2.143 ± 0.117	0.479 ± 0.172	1.254
	VIII	57.473 ± 0.093	0.223 ± 0.001	-0.597	0.102 ± 0.120	1.365 ± 0.221	1.387
281	VII	56.493 ± 0.090	0.225 ± 0.001	-0.596	-2.320 ± 0.120	0.306 ± 0.153	1.372
	VIII	57.106 ± 0.095	0.223 ± 0.001	-0.598	-0.071 ± 0.122	1.760 ± 0.231	1.877
331	VII	56.930 ± 0.093	0.220 ± 0.001	-0.595	-1.957 ± 0.122	0.400 ± 0.186	1.260
	VIII	57.336 ± 0.097	0.219 ± 0.001	-0.598	0.254 ± 0.124	1.668 ± 0.234	1.843
817	VII	57.123 ± 0.087	0.218 ± 0.001	-0.602	-1.784 ± 0.119	-0.472 ± 0.065	3.560
	VIII	57.462 ± 0.093	0.216 ± 0.001	-0.599	0.138 ± 0.120	0.839 ± 0.195	1.888
867	VII	56.585 ± 0.089	0.221 ± 0.001	-0.601	-1.727 ± 0.117	0.855 ± 0.176	2.444
	VIII	56.746 ± 0.091	0.220 ± 0.001	-0.595	0.212 ± 0.118	1.518 ± 0.218	1.175
917	VII	57.448 ± 0.091	0.220 ± 0.001	-0.590	-1.818 ± 0.122	0.462 ± 0.185	1.262
	VIII	57.576 ± 0.095	0.219 ± 0.001	-0.589	0.212 ± 0.123	1.308 ± 0.235	1.671
967	VII	58.539 ± 0.088	0.215 ± 0.001	-0.595	-1.700 ± 0.115	0.590 ± 0.191	0.934
	VIII	58.740 ± 0.091	0.214 ± 0.001	-0.593	0.134 ± 0.116	1.134 ± 0.225	1.244
2602	VII	58.406 ± 0.086	0.218 ± 0.001	-0.583	-3.232 ± 0.114	0.642 ± 0.206	3.794
	VIII	58.916 ± 0.089	0.215 ± 0.001	-0.587	-0.691 ± 0.116	0.755 ± 0.217	4.027
2652	VII	55.293 ± 0.089	0.232 ± 0.001	-0.593	-3.136 ± 0.120	0.413 ± 0.158	1.289
	VIII	55.603 ± 0.090	0.231 ± 0.001	-0.588	-0.781 ± 0.121	0.663 ± 0.186	2.381
2702	VII	57.074 ± 0.086	0.220 ± 0.001	-0.583	-3.291 ± 0.118	-0.016 ± 0.165	2.883
	VIII	57.533 ± 0.090	0.218 ± 0.001	-0.580	-0.637 ± 0.119	0.917 ± 0.227	3.905
2752	VII	56.727 ± 0.088	0.222 ± 0.001	-0.587	-3.108 ± 0.120	-0.032 ± 0.146	1.927
	VIII	57.007 ± 0.090	0.221 ± 0.001	-0.581	-0.697 ± 0.121	0.342 ± 0.199	3.603

Table D.1 Fit parameters obtained from BCM-H in the horizontal scans VII and VIII to Event-OR after background correction.

BCID	Scan	$\Sigma_y[\mu m]$	$\mu_{\mathrm{vis,sp}}^{\mathrm{MAX}}[(10^{22}p)^{-2}]$	$Cov_{\Sigma_y-\mu_{\mathrm{vis,sp}}^{\mathrm{MAX}}}$	$Y_0[\mu m]$	p0$[10^{-4}(10^{22}p)^{-2}]$	χ^2/Ndf
81	VII	57.050 ± 0.096	0.235 ± 0.001	-0.598	0.979 ± 0.127	-0.167 ± 0.169	2.030
	VIII	57.297 ± 0.099	0.235 ± 0.001	-0.595	2.684 ± 0.128	0.375 ± 0.221	1.402
131	VII	58.462 ± 0.095	0.212 ± 0.001	-0.595	1.098 ± 0.123	-0.377 ± 0.177	1.564
	VIII	58.828 ± 0.097	0.211 ± 0.001	-0.595	2.409 ± 0.124	0.120 ± 0.214	1.880
181	VII	59.001 ± 0.096	0.209 ± 0.001	-0.594	1.037 ± 0.129	-0.752 ± 0.124	1.339
	VIII	59.240 ± 0.099	0.209 ± 0.001	-0.594	2.353 ± 0.129	-0.474 ± 0.175	1.630
231	VII	58.430 ± 0.090	0.225 ± 0.001	-0.595	1.000 ± 0.119	-0.498 ± 0.148	1.185
	VIII	58.791 ± 0.092	0.223 ± 0.001	-0.595	2.702 ± 0.121	-0.773 ± 0.160	1.246
281	VII	59.118 ± 0.097	0.222 ± 0.001	-0.591	0.904 ± 0.124	-0.011 ± 0.233	2.291
	VIII	59.280 ± 0.096	0.222 ± 0.001	-0.594	2.622 ± 0.125	-0.315 ± 0.200	1.125
331	VII	59.599 ± 0.095	0.219 ± 0.001	-0.586	1.024 ± 0.125	-0.785 ± 0.196	2.117
	VIII	59.769 ± 0.098	0.219 ± 0.001	-0.592	2.649 ± 0.126	-0.455 ± 0.214	0.803
817	VII	60.097 ± 0.094	0.218 ± 0.001	-0.593	1.636 ± 0.122	-0.931 ± 0.177	0.532
	VIII	60.446 ± 0.097	0.216 ± 0.001	-0.589	3.064 ± 0.123	-1.069 ± 0.224	1.661
867	VII	59.990 ± 0.093	0.220 ± 0.001	-0.593	1.616 ± 0.121	-0.790 ± 0.197	1.160
	VIII	60.282 ± 0.095	0.219 ± 0.001	-0.593	2.807 ± 0.122	-0.609 ± 0.206	0.783
917	VII	59.329 ± 0.095	0.219 ± 0.001	-0.593	1.514 ± 0.124	-0.650 ± 0.189	1.368
	VIII	59.440 ± 0.097	0.218 ± 0.001	-0.594	2.966 ± 0.125	-0.505 ± 0.196	0.549
967	VII	59.851 ± 0.090	0.213 ± 0.001	-0.593	1.680 ± 0.117	-0.654 ± 0.186	1.188
	VIII	60.179 ± 0.093	0.212 ± 0.001	-0.591	2.874 ± 0.118	-0.286 ± 0.223	1.008
2602	VII	59.078 ± 0.090	0.214 ± 0.001	-0.595	0.564 ± 0.116	-0.238 ± 0.190	1.428
	VIII	59.563 ± 0.092	0.211 ± 0.001	-0.601	2.565 ± 0.117	-0.327 ± 0.183	2.449
2652	VII	57.957 ± 0.095	0.230 ± 0.001	-0.595	0.310 ± 0.123	-0.018 ± 0.198	1.745
	VIII	58.430 ± 0.096	0.228 ± 0.001	-0.596	2.577 ± 0.125	-0.302 ± 0.180	1.094
2702	VII	59.416 ± 0.092	0.216 ± 0.001	-0.591	0.608 ± 0.121	-0.964 ± 0.166	1.682
	VIII	59.854 ± 0.095	0.215 ± 0.001	-0.590	2.572 ± 0.122	-0.521 ± 0.217	1.649
2752	VII	59.380 ± 0.092	0.217 ± 0.001	-0.593	0.668 ± 0.123	-0.918 ± 0.125	1.467
	VIII	59.885 ± 0.094	0.216 ± 0.001	-0.595	2.307 ± 0.125	-1.063 ± 0.133	0.653

Table D.2 Fit parameters obtained from BCM-H in the vertical scans VII and VIII to Event-OR after background correction.

BCID	Scan	$\Sigma_x[\mu m]$	$\mu_{\mathrm{vis,sp}}^{\mathrm{MAX}}[(10^{22}p)^{-2}]$	$Cov_{\Sigma_x-\mu_{\mathrm{vis,sp}}^{\mathrm{MAX}}}$	$X_0[\mu m]$	p0$[10^{-4}(10^{22}p)^{-2}]$	χ^2/Ndf
81	VII	55.405 ± 0.093	0.240 ± 0.001	-0.595	-2.184 ± 0.123	0.499 ± 0.182	0.934
	VIII	55.946 ± 0.096	0.237 ± 0.001	-0.600	0.090 ± 0.126	0.872 ± 0.189	2.418
131	VII	59.159 ± 0.094	0.219 ± 0.001	-0.583	-2.076 ± 0.122	0.519 ± 0.241	2.152
	VIII	59.841 ± 0.098	0.216 ± 0.001	-0.586	-0.242 ± 0.124	1.378 ± 0.274	1.798
181	VII	58.933 ± 0.092	0.218 ± 0.001	-0.578	-2.414 ± 0.126	-0.509 ± 0.163	4.773
	VIII	59.728 ± 0.099	0.215 ± 0.001	-0.580	-0.303 ± 0.129	0.646 ± 0.269	3.055
231	VII	56.793 ± 0.089	0.226 ± 0.001	-0.592	-2.253 ± 0.117	0.601 ± 0.191	1.021
	VIII	57.347 ± 0.093	0.224 ± 0.001	-0.598	-0.133 ± 0.119	1.493 ± 0.225	1.434
281	VII	56.533 ± 0.089	0.228 ± 0.001	-0.597	-2.347 ± 0.119	0.111 ± 0.134	1.532
	VIII	57.066 ± 0.095	0.225 ± 0.001	-0.596	0.037 ± 0.122	1.688 ± 0.238	2.050
331	VII	56.789 ± 0.092	0.224 ± 0.001	-0.594	-2.352 ± 0.121	0.561 ± 0.186	1.308
	VIII	57.380 ± 0.096	0.220 ± 0.001	-0.596	0.034 ± 0.124	1.362 ± 0.222	1.332
817	VII	57.161 ± 0.089	0.219 ± 0.001	-0.599	-1.790 ± 0.118	0.147 ± 0.144	1.940
	VIII	57.488 ± 0.093	0.217 ± 0.001	-0.596	-0.222 ± 0.120	1.102 ± 0.209	1.528
867	VII	56.622 ± 0.089	0.222 ± 0.001	-0.602	-1.639 ± 0.117	0.657 ± 0.171	1.674
	VIII	56.714 ± 0.092	0.221 ± 0.001	-0.595	0.041 ± 0.118	2.099 ± 0.234	1.362
917	VII	57.442 ± 0.091	0.222 ± 0.001	-0.592	-1.795 ± 0.121	0.473 ± 0.181	1.203
	VIII	57.654 ± 0.095	0.221 ± 0.001	-0.591	0.070 ± 0.122	1.321 ± 0.243	1.278
967	VII	58.408 ± 0.088	0.217 ± 0.001	-0.594	-1.756 ± 0.114	0.974 ± 0.206	1.120
	VIII	58.560 ± 0.091	0.216 ± 0.001	-0.591	0.178 ± 0.116	1.740 ± 0.247	1.885
2602	VII	58.488 ± 0.085	0.219 ± 0.001	-0.586	-3.142 ± 0.114	0.379 ± 0.188	3.345
	VIII	58.877 ± 0.088	0.218 ± 0.001	-0.586	-0.905 ± 0.115	0.782 ± 0.222	2.953
2652	VII	55.435 ± 0.089	0.235 ± 0.001	-0.592	-3.277 ± 0.119	0.344 ± 0.168	1.199
	VIII	55.849 ± 0.090	0.233 ± 0.001	-0.592	-0.795 ± 0.121	0.564 ± 0.169	1.845
2702	VII	57.021 ± 0.087	0.224 ± 0.001	-0.580	-3.262 ± 0.117	0.218 ± 0.192	3.936
	VIII	57.773 ± 0.090	0.220 ± 0.001	-0.583	-0.523 ± 0.119	0.905 ± 0.225	3.202
2752	VII	56.764 ± 0.088	0.223 ± 0.001	-0.584	-3.179 ± 0.119	0.353 ± 0.183	2.435
	VIII	57.093 ± 0.090	0.222 ± 0.001	-0.582	-0.734 ± 0.120	0.223 ± 0.195	3.736

Table D.3 Fit parameters obtained from BCM-V in the horizontal scans VII and VIII to Event-OR after background correction.

BCID	Scan	$\Sigma_y[\mu m]$	$\mu_{\mathrm{vis,sp}}^{\mathrm{MAX}}[(10^{22}p)^{-2}]$	$Cov_{\Sigma_y-\mu_{\mathrm{vis,sp}}^{\mathrm{MAX}}}$	$Y_0[\mu m]$	p0$[10^{-4}(10^{22}p)^{-2}]$	χ^2/Ndf
81	VII	56.988 ± 0.093	0.238 ± 0.001	-0.597	1.055 ± 0.126	-0.591 ± 0.080	1.667
	VIII	57.236 ± 0.097	0.237 ± 0.001	-0.599	2.355 ± 0.127	-0.059 ± 0.177	1.993
131	VII	58.468 ± 0.092	0.214 ± 0.001	-0.594	1.095 ± 0.122	-0.513 ± 0.140	2.960
	VIII	58.989 ± 0.093	0.212 ± 0.001	-0.601	2.682 ± 0.124	-1.270 ± 0.072	2.737
181	VII	58.708 ± 0.098	0.212 ± 0.001	-0.596	1.126 ± 0.127	-0.269 ± 0.176	1.831
	VIII	59.272 ± 0.100	0.210 ± 0.001	-0.597	2.322 ± 0.129	-0.388 ± 0.180	1.272
231	VII	58.538 ± 0.089	0.226 ± 0.001	-0.591	1.164 ± 0.119	-0.783 ± 0.147	2.063
	VIII	58.808 ± 0.090	0.226 ± 0.001	-0.596	2.545 ± 0.120	-0.813 ± 0.134	0.695
281	VII	59.047 ± 0.094	0.225 ± 0.001	-0.595	1.128 ± 0.123	-0.523 ± 0.170	0.848
	VIII	59.224 ± 0.097	0.224 ± 0.001	-0.596	2.449 ± 0.124	-0.346 ± 0.207	1.344
331	VII	59.510 ± 0.097	0.221 ± 0.001	-0.589	1.011 ± 0.125	-0.390 ± 0.228	1.442
	VIII	59.932 ± 0.097	0.220 ± 0.001	-0.590	2.671 ± 0.126	-1.031 ± 0.196	1.881
817	VII	60.017 ± 0.093	0.220 ± 0.001	-0.592	1.825 ± 0.121	-1.100 ± 0.183	1.578
	VIII	60.533 ± 0.094	0.218 ± 0.001	-0.589	2.747 ± 0.123	-1.153 ± 0.189	1.211
867	VII	60.031 ± 0.092	0.222 ± 0.001	-0.595	1.634 ± 0.120	-0.976 ± 0.173	1.108
	VIII	60.371 ± 0.096	0.221 ± 0.001	-0.594	2.750 ± 0.121	-0.976 ± 0.226	2.216
917	VII	59.316 ± 0.093	0.221 ± 0.001	-0.595	1.737 ± 0.123	-0.944 ± 0.143	0.961
	VIII	59.605 ± 0.097	0.220 ± 0.001	-0.595	2.968 ± 0.125	-0.696 ± 0.202	1.573
967	VII	59.774 ± 0.090	0.216 ± 0.001	-0.596	1.714 ± 0.116	-0.648 ± 0.180	1.431
	VIII	60.134 ± 0.093	0.214 ± 0.001	-0.594	2.707 ± 0.117	-0.399 ± 0.217	1.247
2602	VII	59.193 ± 0.088	0.214 ± 0.001	-0.600	0.552 ± 0.116	-0.546 ± 0.143	1.796
	VIII	59.678 ± 0.090	0.214 ± 0.001	-0.598	2.620 ± 0.117	-0.701 ± 0.160	1.705
2652	VII	58.088 ± 0.093	0.231 ± 0.001	-0.594	0.422 ± 0.123	-0.418 ± 0.165	1.009
	VIII	58.500 ± 0.095	0.229 ± 0.001	-0.598	2.349 ± 0.124	-0.457 ± 0.158	1.521
2702	VII	59.452 ± 0.093	0.219 ± 0.001	-0.591	0.664 ± 0.120	-0.679 ± 0.200	1.518
	VIII	59.901 ± 0.094	0.216 ± 0.001	-0.592	2.436 ± 0.122	-0.869 ± 0.195	1.236
2752	VII	59.538 ± 0.094	0.219 ± 0.001	-0.594	0.582 ± 0.123	-0.786 ± 0.167	1.545
	VIII	59.877 ± 0.095	0.218 ± 0.001	-0.590	2.494 ± 0.124	-1.000 ± 0.182	1.405

Table D.4 Fit parameters obtained from BCM-V in the vertical scans VII and VIII to Event-OR after background correction.

BCID	Scan	$\Sigma_x[\mu m]$	$\mu_{\mathrm{vis,sp}}^{\mathrm{MAX}}[(10^{22}p)^{-2}]$	$Cov_{\Sigma_x-\mu_{\mathrm{vis,sp}}^{\mathrm{MAX}}}$	$X_0[\mu m]$	p0$[10^{-4}(10^{22}p)^{-2}]$	χ^2/Ndf
81	VII	55.469 ± 0.395	0.007 ± 0.000	-0.541	-1.647 ± 0.464	0.007 ± 0.033	0.846
	VIII	55.239 ± 0.433	0.007 ± 0.000	-0.527	1.092 ± 0.472	0.135 ± 0.065	0.710
131	VII	59.384 ± 0.399	0.006 ± 0.000	-0.513	-2.972 ± 0.446	0.026 ± 0.052	0.689
	VIII	59.464 ± 0.406	0.006 ± 0.000	-0.519	-0.532 ± 0.453	0.012 ± 0.050	1.024
181	VII	59.632 ± 0.422	0.006 ± 0.000	-0.512	-2.939 ± 0.480	-0.046 ± 0.049	0.790
	VIII	59.997 ± 0.422	0.006 ± 0.000	-0.539	0.528 ± 0.488	-0.017 ± 0.034	0.645
231	VII	56.128 ± 0.360	0.007 ± 0.000	-0.546	-2.357 ± 0.415	-0.000 ± 0.028	0.717
	VIII	57.556 ± 0.377	0.007 ± 0.000	-0.538	-0.648 ± 0.434	-0.040 ± 0.030	0.693
281	VII	56.047 ± 0.389	0.007 ± 0.000	-0.538	-2.218 ± 0.433	0.013 ± 0.042	0.907
	VIII	56.757 ± 0.410	0.007 ± 0.000	-0.541	0.461 ± 0.449	0.051 ± 0.047	0.807
331	VII	57.699 ± 0.405	0.007 ± 0.000	-0.548	-2.437 ± 0.453	-0.038 ± 0.030	1.087
	VIII	56.657 ± 0.403	0.007 ± 0.000	-0.534	-0.225 ± 0.453	0.043 ± 0.045	0.905
817	VII	57.201 ± 0.371	0.006 ± 0.000	-0.543	-1.651 ± 0.429	0.006 ± 0.029	1.297
	VIII	57.750 ± 0.385	0.006 ± 0.000	-0.543	-0.026 ± 0.437	-0.033 ± 0.029	1.552
867	VII	56.307 ± 0.388	0.007 ± 0.000	-0.541	-1.630 ± 0.420	0.078 ± 0.047	1.321
	VIII	57.110 ± 0.382	0.006 ± 0.000	-0.545	0.652 ± 0.430	-0.021 ± 0.030	0.737
917	VII	57.911 ± 0.383	0.007 ± 0.000	-0.540	-2.089 ± 0.445	0.002 ± 0.031	0.985
	VIII	57.719 ± 0.388	0.007 ± 0.000	-0.534	-0.221 ± 0.449	-0.038 ± 0.031	1.019
967	VII	58.887 ± 0.367	0.006 ± 0.000	-0.518	-1.537 ± 0.405	-0.001 ± 0.046	0.474
	VIII	58.479 ± 0.363	0.006 ± 0.000	-0.545	0.804 ± 0.407	-0.040 ± 0.027	1.032
2602	VII	58.378 ± 0.362	0.006 ± 0.000	-0.505	-2.926 ± 0.398	0.057 ± 0.054	1.071
	VIII	59.301 ± 0.349	0.006 ± 0.000	-0.539	-0.490 ± 0.404	-0.033 ± 0.025	0.931
2652	VII	55.231 ± 0.376	0.007 ± 0.000	-0.543	-2.941 ± 0.441	0.016 ± 0.031	0.794
	VIII	55.797 ± 0.376	0.007 ± 0.000	-0.534	-0.858 ± 0.443	-0.031 ± 0.031	0.857
2702	VII	57.251 ± 0.357	0.007 ± 0.000	-0.537	-3.067 ± 0.420	-0.004 ± 0.029	0.791
	VIII	57.898 ± 0.389	0.006 ± 0.000	-0.528	0.175 ± 0.428	-0.152 ± 0.034	1.525
2752	VII	56.736 ± 0.375	0.007 ± 0.000	-0.513	-3.635 ± 0.436	-0.019 ± 0.044	1.240
	VIII	56.538 ± 0.343	0.007 ± 0.000	-0.510	0.062 ± 0.432	-0.091 ± 0.020	3.374

Table D.5 Fit parameters obtained from BCM-V in the horizontal scans VII and VIII to Event-AND .

BCID	Scan	$\Sigma_y[\mu m]$	$\mu_{\mathrm{vis,sp}}^{\mathrm{MAX}}[(10^{22}p)^{-2}]$	$Cov_{\Sigma_y-\mu_{\mathrm{vis,sp}}^{\mathrm{MAX}}}$	$Y_0[\mu m]$	p0$[10^{-4}(10^{22}p)^{-2}]$	χ^2/Ndf
81	VII	56.634 ± 0.396	0.007 ± 0.000	-0.538	0.643 ± 0.470	-0.036 ± 0.027	0.942
	VIII	57.446 ± 0.430	0.007 ± 0.000	-0.525	2.065 ± 0.490	-0.024 ± 0.049	0.851
131	VII	57.966 ± 0.375	0.006 ± 0.000	-0.528	0.877 ± 0.448	-0.021 ± 0.029	1.837
	VIII	58.551 ± 0.402	0.006 ± 0.000	-0.545	3.118 ± 0.458	-0.012 ± 0.031	0.906
181	VII	58.497 ± 0.418	0.006 ± 0.000	-0.544	0.632 ± 0.481	-0.013 ± 0.031	0.894
	VIII	59.704 ± 0.426	0.006 ± 0.000	-0.542	2.383 ± 0.491	-0.077 ± 0.023	0.961
231	VII	57.930 ± 0.385	0.007 ± 0.000	-0.533	1.510 ± 0.425	-0.009 ± 0.043	1.140
	VIII	59.228 ± 0.383	0.007 ± 0.000	-0.544	2.887 ± 0.438	-0.072 ± 0.024	1.098
281	VII	58.516 ± 0.403	0.007 ± 0.000	-0.521	0.872 ± 0.447	0.049 ± 0.054	0.605
	VIII	58.460 ± 0.390	0.007 ± 0.000	-0.536	2.856 ± 0.455	-0.024 ± 0.031	1.523
331	VII	59.998 ± 0.401	0.006 ± 0.000	-0.531	1.408 ± 0.465	-0.066 ± 0.031	1.022
	VIII	59.730 ± 0.401	0.007 ± 0.000	-0.539	2.970 ± 0.464	-0.064 ± 0.025	0.822
817	VII	60.309 ± 0.397	0.007 ± 0.000	-0.541	2.361 ± 0.444	-0.073 ± 0.031	1.012
	VIII	60.594 ± 0.407	0.006 ± 0.000	-0.507	2.668 ± 0.448	-0.029 ± 0.055	0.873
867	VII	59.688 ± 0.395	0.007 ± 0.000	-0.535	1.955 ± 0.433	0.004 ± 0.044	1.557
	VIII	60.402 ± 0.393	0.007 ± 0.000	-0.548	2.894 ± 0.439	-0.040 ± 0.029	0.838
917	VII	58.972 ± 0.384	0.007 ± 0.000	-0.528	1.996 ± 0.451	-0.113 ± 0.022	3.016
	VIII	59.582 ± 0.418	0.006 ± 0.000	-0.523	2.953 ± 0.463	0.018 ± 0.051	1.379
967	VII	59.747 ± 0.356	0.006 ± 0.000	-0.539	1.381 ± 0.408	-0.030 ± 0.027	0.743
	VIII	59.803 ± 0.380	0.006 ± 0.000	-0.532	3.198 ± 0.413	0.014 ± 0.044	0.910
2602	VII	59.218 ± 0.366	0.006 ± 0.000	-0.546	1.352 ± 0.406	-0.055 ± 0.027	0.946
	VIII	59.253 ± 0.361	0.006 ± 0.000	-0.543	3.000 ± 0.411	-0.022 ± 0.027	0.728
2652	VII	57.879 ± 0.392	0.007 ± 0.000	-0.540	0.818 ± 0.454	-0.041 ± 0.030	1.590
	VIII	58.203 ± 0.401	0.007 ± 0.000	-0.546	2.717 ± 0.461	-0.009 ± 0.033	0.556
2702	VII	59.982 ± 0.386	0.006 ± 0.000	-0.542	0.976 ± 0.440	-0.031 ± 0.030	0.537
	VIII	60.251 ± 0.407	0.006 ± 0.000	-0.516	2.915 ± 0.444	0.012 ± 0.053	1.121
2752	VII	58.995 ± 0.402	0.006 ± 0.000	-0.545	1.277 ± 0.456	-0.019 ± 0.031	1.651
	VIII	59.838 ± 0.402	0.006 ± 0.000	-0.541	2.350 ± 0.459	-0.031 ± 0.031	0.878

Table D.6 Fit parameters obtained from BCM-V in the vertical scans VII and VIII to Event-AND .

BCID	Scan	$\Sigma_x[\mu m]$	$\mu_{\mathrm{vis,sp}}^{\mathrm{MAX}}[(10^{22}p)^{-2}]$	$Cov_{\Sigma_x-\mu_{\mathrm{vis,sp}}^{\mathrm{MAX}}}$	$X_0[\mu m]$	p0$[10^{-4}(10^{22}p)^{-2}]$	χ^2/Ndf
81	VII	54.732 ± 0.401	0.007 ± 0.000	-0.545	-2.213 ± 0.463	-0.000 ± 0.032	0.915
	VIII	56.463 ± 0.416	0.007 ± 0.000	-0.546	0.371 ± 0.485	-0.026 ± 0.027	0.571
131	VII	58.990 ± 0.372	0.006 ± 0.000	-0.532	-2.250 ± 0.439	-0.072 ± 0.020	0.990
	VIII	60.056 ± 0.422	0.006 ± 0.000	-0.520	-0.040 ± 0.462	0.026 ± 0.053	0.404
181	VII	59.480 ± 0.401	0.006 ± 0.000	-0.524	-2.212 ± 0.482	-0.030 ± 0.033	1.146
	VIII	59.907 ± 0.439	0.006 ± 0.000	-0.510	0.033 ± 0.491	0.014 ± 0.057	0.946
231	VII	56.761 ± 0.362	0.007 ± 0.000	-0.544	-2.223 ± 0.422	-0.031 ± 0.023	0.926
	VIII	58.329 ± 0.390	0.006 ± 0.000	-0.539	1.055 ± 0.444	-0.038 ± 0.032	1.277
281	VII	56.757 ± 0.382	0.007 ± 0.000	-0.548	-3.200 ± 0.443	-0.026 ± 0.023	1.212
	VIII	56.035 ± 0.383	0.007 ± 0.000	-0.547	0.311 ± 0.445	-0.026 ± 0.023	0.896
331	VII	56.781 ± 0.406	0.006 ± 0.000	-0.555	-2.299 ± 0.457	-0.002 ± 0.030	1.479
	VIII	56.868 ± 0.409	0.006 ± 0.000	-0.526	0.697 ± 0.460	0.058 ± 0.049	1.023
817	VII	57.234 ± 0.379	0.006 ± 0.000	-0.548	-2.494 ± 0.434	0.014 ± 0.029	1.140
	VIII	57.363 ± 0.402	0.006 ± 0.000	-0.540	0.118 ± 0.443	0.053 ± 0.043	0.889
867	VII	55.594 ± 0.377	0.006 ± 0.000	-0.530	-1.271 ± 0.418	0.082 ± 0.047	0.961
	VIII	56.581 ± 0.365	0.006 ± 0.000	-0.542	-0.981 ± 0.427	-0.027 ± 0.022	1.109
917	VII	57.501 ± 0.393	0.007 ± 0.000	-0.545	-1.627 ± 0.445	-0.031 ± 0.029	1.008
	VIII	57.736 ± 0.396	0.006 ± 0.000	-0.537	-0.059 ± 0.454	-0.050 ± 0.030	0.723
967	VII	58.981 ± 0.355	0.006 ± 0.000	-0.542	-2.341 ± 0.407	-0.013 ± 0.026	0.842
	VIII	59.153 ± 0.380	0.006 ± 0.000	-0.522	0.101 ± 0.415	0.022 ± 0.047	0.503
2602	VII	58.775 ± 0.367	0.006 ± 0.000	-0.525	-2.848 ± 0.401	0.031 ± 0.045	0.744
	VIII	59.002 ± 0.376	0.006 ± 0.000	-0.509	-0.186 ± 0.409	0.091 ± 0.056	1.345
2652	VII	54.725 ± 0.369	0.007 ± 0.000	-0.536	-3.143 ± 0.439	-0.042 ± 0.024	0.934
	VIII	56.113 ± 0.392	0.007 ± 0.000	-0.538	-1.049 ± 0.458	-0.023 ± 0.031	0.549
2702	VII	58.128 ± 0.390	0.006 ± 0.000	-0.524	-3.811 ± 0.434	-0.035 ± 0.043	0.621
	VIII	58.417 ± 0.390	0.006 ± 0.000	-0.527	-1.407 ± 0.437	-0.010 ± 0.041	0.831
2752	VII	56.613 ± 0.368	0.006 ± 0.000	-0.531	-3.899 ± 0.437	-0.062 ± 0.023	1.932
	VIII	56.892 ± 0.362	0.006 ± 0.000	-0.522	-0.158 ± 0.435	-0.095 ± 0.021	1.402

Table D.7 Fit parameters obtained from BCM-H in the horizontal scans VII and VIII to Event-AND .

BCID	Scan	$\Sigma_y[\mu m]$	$\mu_{\mathrm{vis,sp}}^{\mathrm{MAX}}[(10^{22}p)^{-2}]$	$Cov_{\Sigma_y-\mu_{\mathrm{vis,sp}}^{\mathrm{MAX}}}$	$Y_0[\mu m]$	p0$[10^{-4}(10^{22}p)^{-2}]$	χ^2/Ndf
81	VII	56.453 ± 0.400	0.007 ± 0.000	-0.541	0.690 ± 0.471	-0.028 ± 0.027	0.868
	VIII	57.078 ± 0.430	0.007 ± 0.000	-0.556	3.329 ± 0.489	-0.022 ± 0.028	1.032
131	VII	57.783 ± 0.400	0.006 ± 0.000	-0.544	1.391 ± 0.450	-0.045 ± 0.029	1.250
	VIII	58.034 ± 0.410	0.006 ± 0.000	-0.526	2.163 ± 0.451	0.022 ± 0.050	1.112
181	VII	58.836 ± 0.410	0.006 ± 0.000	-0.535	1.534 ± 0.486	-0.070 ± 0.022	0.682
	VIII	58.763 ± 0.440	0.006 ± 0.000	-0.517	2.780 ± 0.489	0.049 ± 0.056	1.134
231	VII	58.391 ± 0.383	0.007 ± 0.000	-0.548	1.683 ± 0.435	-0.003 ± 0.030	0.912
	VIII	58.208 ± 0.395	0.007 ± 0.000	-0.518	2.909 ± 0.439	0.028 ± 0.052	0.800
281	VII	58.377 ± 0.406	0.007 ± 0.000	-0.527	1.083 ± 0.453	0.011 ± 0.048	1.608
	VIII	58.837 ± 0.401	0.007 ± 0.000	-0.540	2.040 ± 0.454	-0.062 ± 0.031	1.618
331	VII	59.077 ± 0.400	0.007 ± 0.000	-0.539	1.937 ± 0.464	-0.020 ± 0.031	1.377
	VIII	59.067 ± 0.412	0.006 ± 0.000	-0.543	2.650 ± 0.470	-0.018 ± 0.032	1.104
817	VII	60.099 ± 0.385	0.006 ± 0.000	-0.532	2.193 ± 0.446	-0.059 ± 0.028	1.267
	VIII	61.454 ± 0.414	0.006 ± 0.000	-0.539	2.487 ± 0.458	-0.093 ± 0.032	1.200
867	VII	60.336 ± 0.393	0.006 ± 0.000	-0.521	1.728 ± 0.438	-0.057 ± 0.043	0.462
	VIII	60.536 ± 0.409	0.006 ± 0.000	-0.528	2.971 ± 0.447	-0.037 ± 0.044	0.841
917	VII	59.281 ± 0.392	0.006 ± 0.000	-0.538	0.848 ± 0.456	-0.062 ± 0.024	0.806
	VIII	59.765 ± 0.429	0.006 ± 0.000	-0.519	3.128 ± 0.467	0.024 ± 0.056	0.649
967	VII	59.539 ± 0.366	0.006 ± 0.000	-0.550	1.586 ± 0.410	-0.053 ± 0.021	0.509
	VIII	59.944 ± 0.380	0.006 ± 0.000	-0.529	2.939 ± 0.418	-0.021 ± 0.040	0.555
2602	VII	59.059 ± 0.387	0.006 ± 0.000	-0.522	0.433 ± 0.411	0.047 ± 0.051	1.501
	VIII	59.310 ± 0.382	0.006 ± 0.000	-0.532	2.872 ± 0.416	0.004 ± 0.042	0.829
2652	VII	57.678 ± 0.397	0.007 ± 0.000	-0.546	0.669 ± 0.460	-0.036 ± 0.025	0.843
	VIII	57.722 ± 0.395	0.007 ± 0.000	-0.541	1.989 ± 0.461	-0.049 ± 0.025	1.026
2702	VII	59.442 ± 0.386	0.006 ± 0.000	-0.540	0.894 ± 0.442	-0.046 ± 0.027	1.039
	VIII	59.923 ± 0.398	0.006 ± 0.000	-0.534	2.747 ± 0.448	-0.095 ± 0.030	0.797
2752	VII	59.184 ± 0.397	0.006 ± 0.000	-0.540	1.235 ± 0.456	-0.019 ± 0.031	0.975
	VIII	59.907 ± 0.414	0.006 ± 0.000	-0.548	2.817 ± 0.462	-0.033 ± 0.030	0.885

Table D.8 Fit parameters obtained from BCM-H in the vertical scans VII and VIII to Event-AND .

D.2 $\mathscr{L}_{sp}$ and σ_{vis} Results

	BCMH_EventOR $\mathscr{L}_{sp}$		BCMV_EventOR $\mathscr{L}_{sp}$	
BCID	Scan VII	Scan VIII	Scan VII	Scan VIII
81	56.905 ± 0.192	56.144 ± 0.194	56.685 ± 0.187	55.894 ± 0.191
131	51.881 ± 0.165	51.064 ± 0.168	51.745 ± 0.163	50.702 ± 0.162
181	51.364 ± 0.167	50.581 ± 0.169	51.730 ± 0.166	50.556 ± 0.169
231	53.917 ± 0.167	53.027 ± 0.169	53.835 ± 0.166	53.071 ± 0.168
281	53.619 ± 0.173	53.010 ± 0.175	53.617 ± 0.169	52.957 ± 0.175
331	52.716 ± 0.171	52.346 ± 0.175	52.959 ± 0.172	52.045 ± 0.171
817	52.007 ± 0.160	51.514 ± 0.166	52.170 ± 0.162	51.432 ± 0.163
867	52.737 ± 0.165	52.414 ± 0.167	52.655 ± 0.164	52.273 ± 0.168
917	52.496 ± 0.168	52.375 ± 0.171	52.528 ± 0.166	52.083 ± 0.171
967	51.079 ± 0.154	50.710 ± 0.157	51.264 ± 0.154	50.824 ± 0.157
2602	51.908 ± 0.155	51.041 ± 0.156	51.696 ± 0.152	50.937 ± 0.153
2652	55.889 ± 0.181	55.126 ± 0.179	55.581 ± 0.178	54.781 ± 0.177
2702	52.688 ± 0.161	52.014 ± 0.164	52.796 ± 0.163	51.718 ± 0.162
2752	53.044 ± 0.164	52.362 ± 0.165	52.958 ± 0.166	52.355 ± 0.165

Table D.9 Values of $\mathscr{L}_{sp}[10^{28}\text{cm}^{-2}\text{s}^{-1}\text{bunch}^{-1}(10^{22}\text{p})^{-1}]$ as obtained from the fits per BCID.

	BCMH_EventAND $\sigma_{vis}[mb]$		BCMV_EventAND $\sigma_{vis}[mb]$	
BCID	Scan VII	Scan VIII	Scan VII	Scan VIII
81	57.925 ± 0.834	55.535 ± 0.828	56.974 ± 0.804	56.402 ± 0.865
131	52.507 ± 0.695	51.353 ± 0.724	51.995 ± 0.685	51.406 ± 0.704
181	51.143 ± 0.701	50.842 ± 0.754	51.308 ± 0.730	49.965 ± 0.709
231	54.001 ± 0.699	52.715 ± 0.710	55.044 ± 0.719	52.503 ± 0.683
281	54.018 ± 0.739	54.287 ± 0.741	54.572 ± 0.755	53.941 ± 0.750
331	53.356 ± 0.742	53.283 ± 0.755	51.701 ± 0.708	52.888 ± 0.731
817	52.033 ± 0.678	50.771 ± 0.698	51.882 ± 0.678	51.147 ± 0.685
867	53.357 ± 0.709	52.254 ± 0.690	53.253 ± 0.720	51.885 ± 0.685
917	52.505 ± 0.706	51.868 ± 0.728	52.407 ± 0.687	52.043 ± 0.715
967	50.967 ± 0.620	50.475 ± 0.644	50.870 ± 0.620	51.177 ± 0.643
2602	51.561 ± 0.659	51.145 ± 0.656	51.772 ± 0.641	50.936 ± 0.610
2652	56.703 ± 0.772	55.258 ± 0.765	55.989 ± 0.760	55.112 ± 0.752
2702	51.799 ± 0.684	51.130 ± 0.681	52.119 ± 0.660	51.306 ± 0.692
2752	53.417 ± 0.706	52.514 ± 0.697	53.472 ± 0.718	52.903 ± 0.676

Table D.10 Values of $\mathscr{L}_{sp}[10^{28}\text{cm}^{-2}\text{s}^{-1}\text{bunch}^{-1}(10^{22}\text{p})^{-1}]$ as obtained from the fits per BCID.

	BCMH_EventORA $\mathscr{L}_{sp}$		BCMV_EventORA $\mathscr{L}_{sp}$	
BCID	Scan VII	Scan VIII	Scan VII	Scan VIII
81	56.974 ± 0.267	55.828 ± 0.268	56.734 ± 0.259	55.847 ± 0.261
131	51.894 ± 0.230	50.880 ± 0.230	51.755 ± 0.227	50.722 ± 0.225
181	51.341 ± 0.229	50.558 ± 0.233	51.807 ± 0.227	50.426 ± 0.229
231	53.727 ± 0.226	52.949 ± 0.231	53.807 ± 0.226	53.118 ± 0.229
281	53.572 ± 0.238	53.027 ± 0.239	53.793 ± 0.232	52.904 ± 0.240
331	52.914 ± 0.237	52.021 ± 0.240	52.798 ± 0.234	51.885 ± 0.234
817	52.139 ± 0.220	51.432 ± 0.226	52.127 ± 0.222	51.457 ± 0.224
867	53.060 ± 0.230	52.192 ± 0.228	52.483 ± 0.226	52.144 ± 0.230
917	52.546 ± 0.232	52.164 ± 0.232	52.704 ± 0.230	52.050 ± 0.235
967	51.082 ± 0.213	50.404 ± 0.215	51.112 ± 0.210	50.879 ± 0.217
2602	51.925 ± 0.212	50.966 ± 0.212	51.784 ± 0.207	50.976 ± 0.208
2652	55.587 ± 0.249	55.169 ± 0.247	55.464 ± 0.242	54.847 ± 0.245
2702	52.503 ± 0.223	51.988 ± 0.226	52.874 ± 0.224	51.789 ± 0.224
2752	53.123 ± 0.225	52.382 ± 0.230	52.830 ± 0.228	52.278 ± 0.227

Table D.11 Values of $\mathscr{L}_{sp}[10^{28}\text{cm}^{-2}\text{s}^{-1}\text{bunch}^{-1}(10^{22}\text{p})^{-1}]$ as obtained from the fits per BCID.

	BCMH_EventORC $\mathscr{L}_{sp}$		BCMV_EventORC $\mathscr{L}_{sp}$	
BCID	Scan VII	Scan VIII	Scan VII	Scan VIII
81	56.846 ± 0.262	55.969 ± 0.265	56.719 ± 0.259	55.959 ± 0.264
131	52.022 ± 0.224	51.089 ± 0.231	51.762 ± 0.221	50.761 ± 0.223
181	51.565 ± 0.229	50.627 ± 0.231	51.619 ± 0.230	50.650 ± 0.234
231	54.136 ± 0.231	52.959 ± 0.233	53.983 ± 0.231	52.989 ± 0.233
281	53.674 ± 0.238	52.877 ± 0.242	53.540 ± 0.235	53.059 ± 0.241
331	52.614 ± 0.233	52.504 ± 0.241	53.028 ± 0.236	52.330 ± 0.237
817	52.119 ± 0.222	51.561 ± 0.229	52.181 ± 0.223	51.430 ± 0.225
867	52.456 ± 0.224	52.454 ± 0.230	52.864 ± 0.223	52.390 ± 0.232
917	52.501 ± 0.230	52.415 ± 0.238	52.322 ± 0.226	52.126 ± 0.235
967	51.078 ± 0.207	50.855 ± 0.214	51.378 ± 0.212	50.789 ± 0.213
2602	51.763 ± 0.212	51.050 ± 0.213	51.615 ± 0.210	50.892 ± 0.209
2652	56.168 ± 0.249	55.014 ± 0.246	55.711 ± 0.248	54.764 ± 0.242
2702	52.976 ± 0.219	51.912 ± 0.224	52.668 ± 0.222	51.633 ± 0.222
2752	53.186 ± 0.229	52.498 ± 0.224	53.103 ± 0.227	52.465 ± 0.225

Table D.12 Values of $\mathscr{L}_{sp}[10^{28}\text{cm}^{-2}\text{s}^{-1}\text{bunch}^{-1}(10^{22}\text{p})^{-1}]$ as obtained from the fits per BCID.

	BCMH_EventORA $\sigma_{\text{vis}}[mb]$		BCMV_EventORA $\sigma_{\text{vis}}[mb]$	
BCID	Scan VII	Scan VIII	Scan VII	Scan VIII
81	2.395 ± 0.007	2.421 ± 0.007	2.438 ± 0.007	2.455 ± 0.007
131	2.386 ± 0.006	2.408 ± 0.006	2.415 ± 0.006	2.442 ± 0.006
181	2.361 ± 0.006	2.398 ± 0.007	2.408 ± 0.006	2.432 ± 0.007
231	2.406 ± 0.006	2.420 ± 0.006	2.439 ± 0.006	2.449 ± 0.006
281	2.408 ± 0.006	2.426 ± 0.006	2.445 ± 0.006	2.457 ± 0.007
331	2.394 ± 0.006	2.416 ± 0.007	2.437 ± 0.006	2.444 ± 0.007
817	2.403 ± 0.006	2.411 ± 0.006	2.437 ± 0.006	2.445 ± 0.006
867	2.395 ± 0.006	2.416 ± 0.006	2.445 ± 0.006	2.447 ± 0.006
917	2.405 ± 0.006	2.407 ± 0.006	2.438 ± 0.006	2.451 ± 0.007
967	2.414 ± 0.006	2.431 ± 0.006	2.443 ± 0.006	2.457 ± 0.006
2602	2.398 ± 0.006	2.413 ± 0.006	2.429 ± 0.006	2.452 ± 0.006
2652	2.391 ± 0.006	2.392 ± 0.006	2.428 ± 0.006	2.442 ± 0.007
2702	2.395 ± 0.006	2.399 ± 0.006	2.425 ± 0.006	2.437 ± 0.006
2752	2.371 ± 0.006	2.402 ± 0.006	2.420 ± 0.006	2.440 ± 0.006
Average	2.395 ± 0.002	2.412 ± 0.002	2.432 ± 0.002	2.446 ± 0.002
χ^2/DOF	5.302	3.111	3.300	1.328

Table D.13 Values of σ_{vis}[mb] as obtained from the fits per BCID. The average values are a weighted average of the individual bunches.

	BCMH_EventORC $\sigma_{\text{vis}}[mb]$		BCMV_EventORC $\sigma_{\text{vis}}[mb]$	
BCID	Scan VII	Scan VIII	Scan VII	Scan VIII
81	2.426 ± 0.007	2.454 ± 0.007	2.445 ± 0.007	2.452 ± 0.007
131	2.407 ± 0.006	2.429 ± 0.007	2.421 ± 0.006	2.450 ± 0.006
181	2.397 ± 0.006	2.420 ± 0.007	2.408 ± 0.006	2.434 ± 0.007
231	2.425 ± 0.006	2.451 ± 0.006	2.427 ± 0.006	2.460 ± 0.006
281	2.422 ± 0.006	2.445 ± 0.007	2.446 ± 0.006	2.456 ± 0.007
331	2.428 ± 0.006	2.438 ± 0.007	2.426 ± 0.006	2.454 ± 0.007
817	2.433 ± 0.006	2.438 ± 0.006	2.438 ± 0.006	2.446 ± 0.006
867	2.443 ± 0.006	2.432 ± 0.006	2.435 ± 0.006	2.446 ± 0.006
917	2.438 ± 0.006	2.434 ± 0.007	2.445 ± 0.006	2.452 ± 0.007
967	2.434 ± 0.006	2.440 ± 0.006	2.446 ± 0.006	2.448 ± 0.006
2602	2.423 ± 0.006	2.428 ± 0.006	2.426 ± 0.006	2.460 ± 0.006
2652	2.394 ± 0.006	2.423 ± 0.006	2.425 ± 0.006	2.443 ± 0.006
2702	2.391 ± 0.006	2.424 ± 0.006	2.426 ± 0.006	2.452 ± 0.006
2752	2.406 ± 0.006	2.428 ± 0.006	2.414 ± 0.006	2.426 ± 0.006
Average	2.419 ± 0.002	2.434 ± 0.002	2.431 ± 0.002	2.448 ± 0.002
χ^2/DOF	7.428	2.507	3.718	2.215

Table D.14 Values of σ_{vis}[mb] as obtained from the fits per BCID. The average values are a weighted average of the individual bunches.

D.3 Background Correction for Event-OR

Side-A	Side-C	Probability
		Model for Signal
		$P_{00} = e^{-\varepsilon_{OR}\mu}$
X		$P_{XORA} = e^{-\varepsilon_{XORC}\mu} - e^{-\varepsilon_{OR}\mu}$
	X	$P_{XORC} = e^{-\varepsilon_{XORA}\mu} - e^{-\varepsilon_{OR}\mu}$
X	X	$P_{AND} = 1 - e^{-\varepsilon_{XORA}\mu} - e^{-\varepsilon_{XORC}\mu} + e^{\varepsilon_{OR}\mu}$
		Model for Background
		$(1 - P_{bXORA})(1 - P_{bXORC})$
0		$P_{bXORA}(1 - P_{bXORC})$
	0	$(1 - P_{bXORA})P_{bXORC}$
0	0	$P_{bXORA}P_{bXORC}$

Table D.15

To simplify things the algorithm name will be used as index instead of the convention used in 5.3.2. In order to derive the background correction for Event-OR , Table D.15 shows the probabilities for having a background events or signal events, respectively. Combining the probability for signal and background for zero counting one gets [79]:

$$P_{00}^{meas} = P_{00}(1 - P_{bXORA} - P_{bXORC} + P_{bXORA}P_{bXORC}) \tag{D.1}$$

Where P_{algo}^{meas} denotes the measured probability including background. As explained in Section 5.3.2 the probability for an inclusive OR event is just one minus the probability of having zero counts:

$$P_{OR}^{meas} = 1 - P_{00}(1 - P_{bXORA} - P_{bXORC} + P_{bXORA}P_{bXORC}) \tag{D.2}$$

$$= 1 - (1 - P_{OR})(1 - P_{bXORA} - P_{bXORC} + P_{bXORA}P_{bXORC}) \tag{D.3}$$

$$= P_{OR}(1 - P_{bXORA} - P_{bXORC} + P_{bXORA}P_{bXORC}) + (P_{bXORA} + P_{bXORC} - P_{bXORA}P_{bXORC}) \tag{D.4}$$

The result for the background corrected Event-OR is therefore:

$$P_{OR} = \frac{P_{OR}^{meas} - (P_{bXORA} + P_{bXORC} - P_{bXORA}P_{bXORC})}{1 - P_{bXORA} - P_{bXORC} + P_{bXORA}P_{bXORC}} \tag{D.5}$$

Danksagungen

Zu allererst möchte ich Prof. Dr. Johannes Haller dafür danken, daß er mir die Möglichkeit gegeben hat, meine Doktorarbeit bei ihm schreiben zu dürfen. Bereits seit 2007, als ich meine Diplomarbeit in seiner ATLAS Gruppe in Hamburg schrieb, konnte ich stets auf seine Unterstützung zählen.
Nicht weniger dankbar bin ich meinem Betreuer Dr. Thilo Pauly am CERN. Er hat sich von Anfang an sehr um mich gekümmert und ich habe viel von ihm gelernt. Ich hatte immer das Gefühl an interessanten und sinnvollen Aufgaben arbeiten zu dürfen und wurde dabei stets sehr gut betreut.
Ich bedanke mich insbesondere für die Möglichkeit, daß ich die gesamte Zeit meiner Doktorarbeit am CERN verbringen konnte und somit auf eine extrem spannende und ereignisreiche Zeit zurückblicken kann.
In diesem Sinne möchte ich auch Dr. Michael Hauschild und der Unterstützung durch das BMBF im Rahmen des Wolfgang-Gentner Stipendiums danken.
Des weiteren möchte ich meinen Kollegen aus ATLAS Luminosity Task Force und der L1CT Gruppe danken, für die freundliche Atmosphäre und die gute Zusammenarbeit. Ganz besonders möchte ich Mika Huhtinen danken, der mir bei vielen Fragen stets geholfen hat und mit dem die Gespräche auch gerne mal über das Bergsteigen abschweifen konnten.
Ich danke außerdem den vielen netten und interessanten Menschen, die ich in den letzten Jahren in Genf kennengelernt und mit denen ich Zeit verbracht habe. Ich hoffe, daß wir noch lange in Kontakt bleiben werden.
Danke an Flaminia für die wundervolle Zeit zusammen und danke dafür, daß sie mich immer dann wenn es nötig war von der Arbeit abgelenkt hat.
Natürlich danke ich von ganzem Herzen meiner Familie, insbesondere meinen Eltern und meinem Bruder Thomas, die mich immer unterstützen und an mich glauben.